Universidad de Sevilla
Escuela Técnica Superior de Ingeniería
Departamento Ingeniería Aeroespacial y Mecánica de Fluidos

Study of the production of drops and their impact on surfaces. Application to the development of an additive manufacturing technique for metals

A dissertation submitted in partial fulfilment of the requirements for the degree of Doctor of Philosophy by:

Beatriz Natividad Muñoz Sánchez

PhD programme:

Ingeniería Mecánica y Organización Industrial

Supervisors:

Prof. Alfonso Miguel Gañán Calvo (Universidad de Sevilla)

Prof. José María Montanero Fernández (Universidad de Extremadura)

Sevilla, 2021

Financial support from “la Caixa”Foundation (ID 100010434) under grant LCF/BQ/ES14/10320005 is gratefully acknowledged.

A quienes me apoyaron en los últimos
100 metros de esta maratón.

AMDG

Agradecimientos

«Si he visto más lejos es porque estoy sentado sobre los hombros de gigantes»

BERNARDO DE CHARTRES

Esta cita, habitualmente atribuida a Isaac Newton, podría parecer algo típica, incluso manida, para comenzar los agradecimientos de un documento académico. Pero es sólo desde el reconocimiento de nuestra pequeñez, o más bien, de nuestra verdadera estatura, desde donde podemos agradecer a quienes generosamente nos tendieron su mano y prestaron sus hombros.

No se trata sólo del aspecto científico, cuyo cuerpo crece cada día más, cimentado sobre el conocimiento anterior. Esta tesis, como cualquier trabajo de investigación, no hubiese sido factible sin el esfuerzo y resultados de quienes nos precedieron.

Para mí los gigantes van más allá. Son personas que me han apoyado en este camino, que tantas veces, y sobre todo en la etapa final, resultó cuesta arriba. Son personas que, incluso sin saberlo, me cargaban sobre sus hombros cuando yo no tenía fuerzas para continuar. Son personas cuya cercanía los hizo más grandes aún ante mis ojos. Son aquellos que me valoraron y así me hicieron ver más lejos, haciéndome sentir que yo era más que simplemente mi trabajo. A estos mis gigantes, que han dejado tanta huella en mí, va dirigido mi más profundo agradecimiento.

En primer lugar, a mis directores de tesis, que me ofrecieron su saber, visión y directrices sobre esta investigación. José Mª, eres un increíble MENTOR en todo el esplendor de la palabra. Hace años confiaste en mí, aun sin conocerme, y me abriste las puertas de este apasionante mundo de la investigación. Aún más, me incluiste en este grupo-familia que has sabido construir, mantener y alentar. Tu mirada crítica, serena y ordenada -que no sólo afecta al ámbito académico, sino a la vida- ha calado en mí. Probablemente nunca dejaré de admirarte, serás siempre “el jefe”. Alfonso, no puedo dejar de darte gracias por haberme abierto tantas puertas en estos años. Sin tu apoyo no hubiese podido disfrutar de muchas oportunidades que se me han brindado. Es un privilegio haber compartido este camino con un gigante de la investigación y la transferencia del conocimiento como tú.

Al grupo de investigación de Mecánica de Fluidos de la Universidad de Extremadura, cuyos miembros me han acogido con cariño, siempre ofreciéndome su ayuda para que pudiera avanzar. Me siento agradecida por haber encontrado un lugar donde verdaderamente quiero estar, tarea a veces difícil en este mundo. Compartir trabajo es, al fin y al cabo, compartir vida, y es una gran suerte hacerlo con personas a las que admiras en lo profesional y en lo personal.

A Lupe -madre, científica y docente ejemplar-, de la que tantísimo he aprendido estos años, y cuya actitud práctica e ingenieril no deja de sorprenderme. A pesar de “habernos quemado como toberas” en muchas ocasiones, lo hemos hecho juntas, como “las Zipi y Zape del perfeccionismo”, y hemos disfrutado y celebrado los resultados que sí salieron adelante.

A Emilio, trabajador incansable cuyo tesón y positividad me encantaría absorber, que me acogió como un hermano mayor en mis primeros pasos en la investigación. Gracias por tu disponibilidad casi infinita, por cada consejo de "*cacharreo*" en el laboratorio, por tu ayuda y cercanía más allá de lo laboral, a veces tan escasa en este mundo deshumanizado. Gracias por pensar en mí y abrirme, generosamente -como no puede ser de otra forma en ti-, una puerta al futuro.

A quienes ya estaban y abrieron sus brazos a mi llegada. A Conrado, grande en todos los sentidos, gracias por tu cercanía y sincero interés, por contar conmigo como una más. A Noelia y Antonio, las primeras personas en las que pude ver, en directo, el esfuerzo e ilusión que requería una tesis doctoral. Fui afortunada de celebrar con vosotros el feliz desenlace, y ahora no puedo sino agradeceros que me hiciérais testigo de esos vuestros pasos. Gracias por vuestros consejos de laboratorio y especialmente por los consejos profesionales, valiosísimos, para intentar hacernos un hueco laboral en este competitivo mundo de la investigación.

A los que llegaron más o menos a la vez que yo, que han sido algo así como mis "hermanos de tesis" bajo un mismo director: Alberto y Rafa, mi compañero de despacho y paciente espectador de tantos momentos "¡me jubilo!". Afortunadamente creo que los buenos momentos ganan en el balance de nuestras horas juntos. Gracias por estar presente en el momento en el que, literalmente, me fallaron las fuerzas.

A quienes llegaron después, y con los que espero seguir compartiendo momentos de grupo y retos laborales: Manu y Alejandro. Os deseo lo mejor en vuestra tesis doctoral y espero poder ayudaros en lo que necesitéis. A quienes completan este grupo de "*fluidines*" y con los que he compartido celebraciones y alegrías: Javi y Tere, desde otra posición, más distendida, habéis sido testigos de la construcción de esta tesis.

Al grupo de Física de Fluidos y Microfluídica de la Universidad de Sevilla. A Pepe y Miguel Ángel, siempre acogedores y con una buena dosis de sentido del humor. A Paco e Irene, compañeros y hermanos de este camino. A Bea, de tanta ayuda en la parte administrativa.

A nuestros colegas portugueses, Rui y Diana, que me han iniciado en el apasionante mundo de la bioingeniería. Gracias por contestar, con tanta paciencia, a mis infinitas dudas y curiosidades acerca de este tema.

Muchos saben que esta tesis ha sido "*movidita*", y no sólo en el sentido laboral o emocional, sino en el geográfico. En estos años dedicados a la investigación he pasado por La Laguna, Cambridge, Redu, Londres, Bremen y Enschede. Más que haber pasado yo por ellos, y como bien decía Fr. Mark Langham (q. e. p. d.), los lugares pasan por nosotros, dejan su profundo rastro en nuestra forma de ser, de mirar. Los recuerdos asociados a estos lugares, y las personas con las que los construí, son imborrables, los llevaré siempre en mi mochila. Gracias a quienes fuisteis un apoyo en tierras lejanas.

A Rafa Castrejón, que me recibió con calidez en un lugar del que me enamoré, en un momento en el que necesitaba encontrar mi camino. Gracias por tu voto inicial de confianza aun sin conocerme, por contagiarme esa pasión tuya por la ciencia que espero que las circunstancias nunca apaguen. Gracias por haber vuelto a contar conmigo en otras ocasiones. Es una fortuna que de nuestro trabajo haya nacido esta amistad.

Al Prof. Detlef Lohse y la Dra. Kirsten Harth, que me abrieron las puertas del grupo PoF (Physics of Fluids) en la Universidad de Twente, tan grande en número como en talento, donde aprendí lecciones muy valiosas.

A mis amigos: los de siempre, los recientes, los de cerca y los de lejos (o muy lejos). A pesar de las dificultades por tiempo, obligaciones o distancia, siempre son un placer esos ratitos que alegran el alma, los de ponernos al día y compartir VIDA. A mi familia política, que me considera una más del clan. A Yolanda, que ha sido como un faro iluminando este último año y medio, de tanta transformación. A mis hermanos en la fe -PJP, Pastoral UEx, Fisher House, Ariëns, Emaús, ENS...-, gracias por haberme sostenido con vuestra oración y ejemplo de vida. A todos aquellos que me asegurábais, con una confianza casi ciega, que conseguiría este reto. Puede que esta sección sea la única inteligible para muchos de vosotros. Mi agradecimiento es dedicaros lo que aquí sigue y el trabajo que hubo detrás.

Para el final han quedado los gigantes más importantes, los más grandes. A mis padres, que sobre sus hombros me mostraron cómo es la vida, quienes me enseñaron el valor del esfuerzo y la renuncia, uno de cuyos frutos es esta tesis. Espero ser siempre digna alumna de tan ejemplares MAESTROS. A mi hermana, que me precedió en muchos puntos del camino y me va dejando "miguitas de pan" en forma de consejos; a la que suelo tener a muchos kilómetros, pero siempre siento cerca. A Yon, que llegó a nuestra familia para aportar un buen *fact-checking* y siempre deja, con paciencia, que le "invadamos" en tierras del Norte. La familia, el lugar donde se aprende y sucede todo lo importante. Gracias por tanto.

A mi marido, Juanlu, mi mayor pilar, testigo de mis días oscuros y compañero de los momentos de luz. Has sido quien me alentaba cada mañana a continuar. Una gran parte de esta tesis es obra de esos abrazos que reconstruyen, protegen y alejan lo malo. Gracias por ser parte de mí, indisoluble, eterna. Nuestro "para siempre" tuvo un comienzo, pero no tiene final.

Sé que las palabras se quedan cortas en tantas cosas que cabe agradecer. Sé que muchos nombres no han sido explicitados. Sé que mi memoria puede haber olvidado a personas en el momento de escribir estas líneas. No así mi corazón, en los que está, indeleble, vuestra huella. GRACIAS.

«El agradecimiento es la memoria del corazón»

JEAN BAPTISTE MASSIEU

Abstract

Drops are constantly and spontaneously produced in nature, but varied industrial fields (such as biotechnology, chemical engineering, pharmacy, food industry or microbiology) require drops to be produced in a controlled manner. Furthermore, many applications in these fields benefit when droplets are very small in size, on the micrometer and even nanometer scale.

Consequently, physics of fluids on the submillimeter scale has been intensively developed in the last decades. Within this area, droplet-based microfluidics has demonstrated to be a leading platform to generate and manipulate a wide range of fluid microentities.

On the other hand, the impact of droplets happens to be critically important in many of the scenarios where they are produced, so this phenomenon should be explored together with droplet delivery.

This application-driven thesis, by compiling a series of 8 published articles, addresses the controlled production of droplets by several droplet-based methods, and their impact on surfaces.

Paper I produces droplets by both *Drop on Demand* and direct *dripping* (gravitational) in order to study their impact over moving liquid surfaces.

Since a particularly interesting application is the development of additive manufacturing for metals, Paper II produces droplets in direct *jetting* mode with that potential use.

The next contributions (Paper III, Paper IV and Paper V) aim to generate and characterize PDMS microparticles mainly to develop blood analogue fluids. In this case, *needle focusing* was used to produce intermediate-state PDMS precursor droplets that will be later cured into solid particles.

A common factor among the aforementioned droplet production techniques is the presence of an orifice or nozzle, which becomes a key element to achieve the fragmentation of a continuous liquid phase into droplets. Therefore, nozzle manufacturing was studied in this thesis through Paper VI and Paper VII.

Finally, the major role played by surface tension at microfluidic scales and its dominance on capillary breakup of jets into droplets requires its value to be accurately known. Paper VIII measures the interfacial tension between two immiscible liquids of similar density, with the consequent application to droplet production methods relying on such value.

Content

LIST OF TABLES

LIST OF FIGURES

1 INTRODUCTION

Drops are constantly produced in nature: from rain drops of large sizes to the small airborne droplets naturally generated from a steaming liquid or the breakage of waves in the ocean. In contrast to these spontaneous examples, drop production in a controlled manner has been intensively explored in the last decades to be applied in many industrial fields: biotechnology, chemical engineering, pharmacy, food industry or microbiology are only some examples.

Special interest have awakened droplets of a very small size, on the micrometer and even nanometer scale. The physics of fluids on the submillimeter scale is characterized by the importance of viscous forces, diffusion, and surface effects; whereas liquid inertia and gravity are generally neglected.

Droplet size is of the uttermost importance for some applications. For example, it determines where in the lungs the aerosol medicines are delivered (Bennett et al., 2002) or defines inkjet printing resolution, where droplets are precisely deposited for graphical purposes or as functional materials (Basaran, 2002; Basaran et al., 2013; Wijshoff, 2010).

Droplets applications expand when they are regarded as an intermediate state in the obtention of other products. Commonly in pharmaceutical applications, a bulk material is fragmented into droplets that will be later solidified by freezing, desolvation or drying (Vehring, 2008), therefore obtaining particles of different shapes and functionalities for solid dispersions or suspensions (Wang et al., 2011).

Droplet-based microfluidics has demonstrated to be a leading platform to generate and manipulate a wide range of fluid microentities (Gañán-Calvo et al., 2013): not only droplets, but other morphologies such as bubbles, simple and compound jets, liquid ligaments, emulsions and capsules. As mentioned for the case of droplets, further operations over these microentities would give rise to complex materials: fibers of different type (solid, hollow, coaxial) from jets (Sattler et al., 2008) or hollow spheres and shells from liquid capsules (Berkland et al., 2004). As one can imagine, possibilities and applications become endless.

The scope of this thesis will be restricted to droplets manufactured by any of the droplet-based production methods schematized in Figure 1.1. Each technique will yield a different degree of monodispersity, which is an important characteristic for the collections of microentities, together with size and morphology.

The first distinction appears between methods acting on demand or methods that continuously generate droplets. In *Drop on Demand* (DoD), an external actuator is required to produce a single pressure pulse on the liquid, so the latter will get ejected through a small orifice. Typical actuators are piezoelectric (Xu and Attinger, 2008) or thermal systems, through the creation of a vapor bubble (Vaught et al., 1984). The great advantage of DoD is its 'digital' nature, so material is only deposited where and when needed. It is a well-established method in industries as graphical inkjet, Organic Light Emitting Diodes (OLEDs) or printed electronics.

On the contrary, other techniques generate *continuous droplet streams* (Christopher and Anna, 2007) that benefit from large production rates and a high degree of monodispersity. They are driven by surface tension and other forces (gravitational, electric, thermal, chemical, hydrodynamic, etc). Continuous production methods used in this thesis are based only on gravitational and hydrodynamic forces.

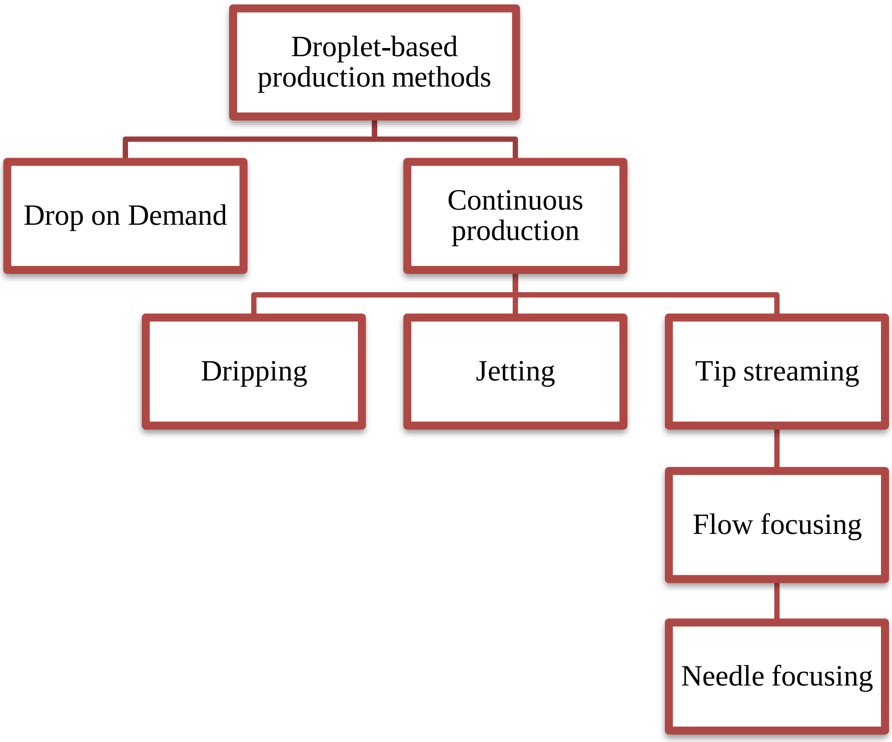

Figure 1.1 Droplet-based production methods used in this thesis, classified by working mode. Built from Gañán-Calvo et al. (2013).

Particularly, gravity is the simplest way to produce droplets. It acts on the *dripping* mode (Basaran, 2002), where the interface pinches at distances in the order of the emitting orifice diameter, and resulting droplets are larger than the latter. Despite its simplicity, dripping is limited to relatively large sizes, since small orifices get clogged easily. This regime can also appear in other configurations not driven by gravity, for example in cross-flow geometries (Baroud et al., 2010; Nisisako et al., 2002).

In the *jetting* regime, an additional input of energy (e. g., pressure) leads to the formation of a liquid ligament that moves downstream. This jet is inherently unstable, since it will end up breaking into droplets (Rayleigh, 1878). In contrast to dripping, the interface pinches off at a distance from the orifice much longer than its diameter.

Direct *dripping* or *jetting* shown in Figure 1.1 will produce droplets in the order of the orifice diameter. To reduce droplet size, *tip streaming* has been largely explored. This flow requires a delicate balance of forces to be established and can be found in varied configurations: electrospray, shear flows in the presence of surfactants, co-flows for sufficiently large viscosities or extensional co-flows (Gañán-Calvo et al., 2013). In all cases, tip streaming is characterized by a hanging meniscus, with droplets/jets being expelled from its very tip, in the so-called *'dripping/jetting via tip streaming'* regimes and with a much smaller size than the device orifice. This thesis only deals with tip streaming happening in extensional co-flows (*Flow Focusing*), where a geometric element causes the streams to accelerate, narrowing the inner fluid thread (Anna, 2016).

Flow Focusing (Gañán-Calvo, 1998) has been largely proved to produce a wide variety of microentities within an immiscible carrier fluid (both liquids and gases) at a continuous high rate (Utada et al., 2005). It benefits from working by purely hydrodynamic means and overcomes the clogging problems of other droplet sources (Kupitz et al., 2014; Weierstall et al., 2014), being applicable to any liquids, even delicate substances used for instance in biological studies (Wiedorn et al., 2018).

Flow Focusing principle has been applied to varied configurations, not only in its 3D axisymmetric geometry, but also in planar devices (Anna et al., 2003). Another popular configuration is the *Gas Dynamic Virtual Nozzle* (GDVN) (DePonte et al., 2008), where the classical plate-orifice is replaced by a converging nozzle, which reduces the sharpness of the orifice, the resulting droplets diameter and the gas (energy) consumption, among other advantages. These configurations and the governing parameters are sketched in Figure 1.2.

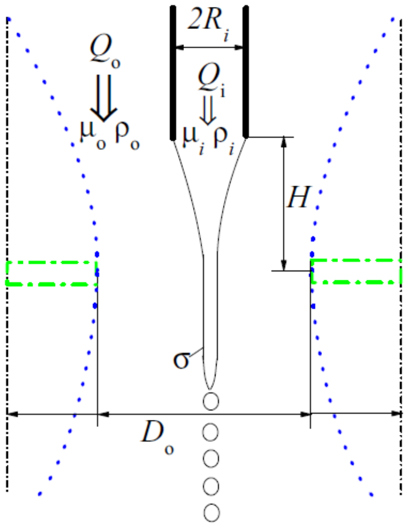

Figure 1.2 Sketch of jetting via tip streaming for different geometries: a channel in co-flow (black line), a classical plate-orifice in *Flow Focusing* (green line) and a nozzle in GDVN (blue line).

Lastly, another *Flow Focusing* configuration has been used in this thesis: the so-called *Needle Focusing* (Acero et al., 2013). The cylindrical capillary used in the classical flow focusing setup to inject the inner liquid is here replaced with a common hypodermic needle of a similar dimension (Figure 1.3). In this way, the tapering meniscus of the standard flow focusing configuration is substituted by a couette-type flow directed towards the needle tip. The completely different dynamics drastically reduces the minimum flow rate to form steady jets, which are ejected from the very tip of the needle with sizes down to the submicrometer scale.

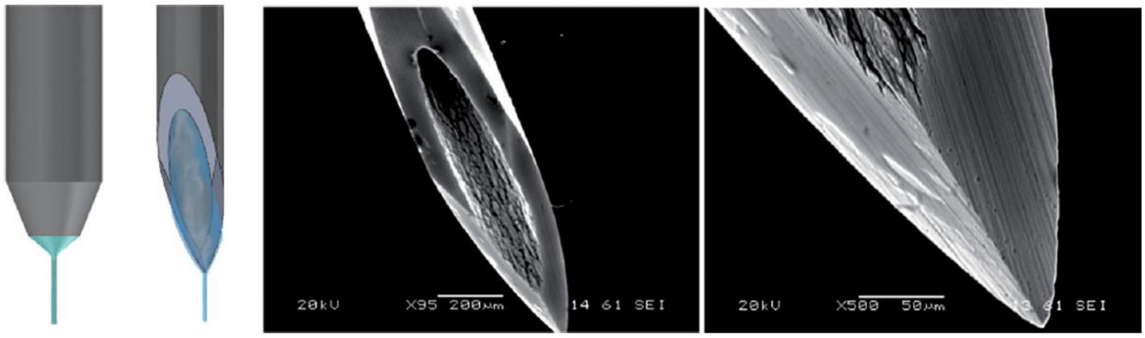

Figure 1.3 Sketch of standard capillary in *Flow Focusing* (left) and hypodermic needle (right) that replaces it, with SEM images of the needle tip.

Needless to say, the impact of droplets is critically important in many of the scenarios where they are produced. For example in nature, the impact of rain affects the erosion of soil (Ahn et al., 2013), buildings (Erkal et al., 2012), and wind turbine blades (Field et al., 2012); but also has an influence in industrial applications such as printing technologies (Ru et al., 2014; Wijshoff, 2010), cleaning of semiconductor wafers (Okorn-Schmidt et al., 2014), metal spray deposition (Djuric and Grant, 2001; McDonald et al., 2006), fuel fragmentation in engines (Moreira et al., 2010), crop spraying and novel applications as deposition of cell-containing drops for the fabrication of living tissue (Binder et al., 2011; Derby, 2008; Tasoglu and Demirci, 2013).

For the continuous development of such applications, and in order to overcome current limitations, a better understanding of droplet formation, droplet–substrate interaction, pinning phenomena, drop coalescence and material compatibility is needed (Derby, 2010; Eggers and Villermaux, 2008). Hence, this thesis also explores the impact of droplets.

1.1 Structure of the document

This thesis compiles a series of comprehensive studies within the field of droplet generation and their impact. It constitutes a collection of 8 articles already published in high-impact peer-reviewed scientific journals, namely:

- Paper I: Castrejón-Pita, J. R.; Muñoz-Sánchez, B. N.; Hutchings, I. M.; Castrejón-Pita, A. A. Droplet Impact onto Moving Liquids. *J. Fluid Mech.* **2016**, *809*, 716–725. https://doi.org/10.1017/jfm.2016.672
- Paper II: Vega, E. J.; Cabezas, M. G.; Muñoz-Sánchez, B. N.; Montanero, J. M.; Gañán-Calvo, A. M. A Novel Technique to Produce Metallic Microdrops for Additive Manufacturing. *Int. J. Adv. Manuf. Technol.* **2014**, *70* (5–8), 1395–1402. https://doi.org/10.1007/s00170-013-5357-3
- Paper III: Muñoz-Sánchez, B. N.; Silva, S. F.; Pinho, D.; Vega, E. J.; Lima, R. Generation of Micro-Sized PDMS Particles by a Flow Focusing Technique for Biomicrofluidics Applications. *Biomicrofluidics* **2016**, *10* (1), 14122. https://doi.org/10.1063/1.4943007
- Paper IV: Anes, C. F.; Pinho, D.; Muñoz-Sánchez, B. N.; Vega, E. J.; Lima, R. Shrinkage and Colour in the Production of Micro-Sized PDMS Particles for Microfluidic Applications. *J. Micromechanics Microengineering* **2018**, *28* (7), 075002. https://doi.org/10.1088/1361-6439/aab7b9
- Paper V: Pinho, D.; Muñoz-Sánchez, B. N.; Anes, C. F.; Vega, E. J.; Lima, R. Flexible PDMS Microparticles to Mimic RBCs in Blood Particulate Analogue Fluids. *Mech. Res. Commun.* **2019**, *100*, 103399. https://doi.org/10.1016/j.mechrescom.2019.103399
- Paper VI: Muñoz-Sánchez, B. N.; Cabezas, M. G. Borosilicate Nozzles Manufactured by Reproducible Fire Shaping. *J. Mater. Process. Technol.* **2018**, *261* (November), 173–183. https://doi.org/10.1016/j.jmatprotec.2018.06.011
- Paper VII: Muñoz-Sánchez, B. N.; Gañán-Calvo, A. M.; Cabezas, M. G. A New Fire Shaping Approach to Produce Highly Axisymmetric and Reproducible Nozzles. *J. Mater. Process. Technol.* **2019**, *270* (August), 241–253. https://doi.org/10.1016/j.jmatprotec.2019.02.027
- Paper VIII: Muñoz-Sánchez, B. N.; Cabezas, M. G.; Ferrera, C.; Herrada, M. A.; Montanero, J. M. A Method for Measuring the Interfacial Tension for Density-Matched Liquids. *J. Colloid Interface Sci.* **2020**, *566*, 90–97. https://doi.org/10.1016/j.jcis.2020.01.043

Each paper, by making use of the different droplet production techniques in Figure 1.1, focuses on a relevant application or aspect.

Paper I produces droplets by both *Drop on Demand* and direct *dripping* (gravitational) in order to study their impact over moving liquid surfaces.

Since a particularly interesting application is the development of additive manufacturing for metals, Paper II produces droplets in direct *jetting* mode with that potential use.

The next contributions (Paper III, Paper IV and Paper V) aim to generate and characterize PDMS microparticles for different applications, mainly to develop blood analogue fluids. In this case, *needle focusing* is used to produce intermediate-state PDMS precursor droplets that will be later cured into solid particles.

A common factor among the aforementioned droplet production techniques is the presence of an orifice or nozzle, either as an emitting source or in other parts of the device (GDVN). This is a key element to achieve the fragmentation of a continuous liquid phase into droplets. Therefore, nozzle manufacturing is addressed in this thesis through Paper VI and Paper VII. Interestingly, glass capillaries used here coincide with the inner one in Paper II device, so any advances in nozzle manufacturing would also benefit the proposed metal manufacturing technique.

Finally, the major role played by surface tension at microfluidic scales and its dominance on capillary breakup of jets into droplets requires its value to be accurately known. In particular, Paper VIII measures the interfacial tension between two immiscible liquids of similar density, with the consequent application to droplet production methods relying on such value.

The subsequent sections in this introductory chapter show an overview of the above fields: Impact of droplets, Additive manufacturing, Generation of PDMS microparticles, Nozzles as the core element and Interfacial tension measurement. Next chapters are subdivided according to the contribution of each individual paper. Chapter 2 identifies the gaps and establishes the specific objectives pursued in each paper. Chapter 3 summarizes the results and briefly discuss them. This memory closes in chapter 4, with the main conclusions and future research possibilities.

1.2 Impact of droplets

The impact of droplets onto moving liquid surfaces or films occurs frequently in nature (e. g. rain drops landing on the ocean), but it is also present and critically important in many industrial processes, such as spray painting, crop spraying or inkjet printing.

The current section explores previous studies on this matter.

1.2.1 Impact onto static pools

First studies about impacting droplets were performed back in the 19th century by Worthington, who focused on droplets impacting a stationary pool of the same liquid (Worthington, 1908). This continues to be an active area of research today (Castrejón-Pita et al., 2012), showing the complexity of the dynamics at the interface, with a wide range of phenomena arising, such as vortices shedding, air bubbles trapping or the generation of daughter microdroplets produced from splash (Deegan et al., 2008; Moore et al., 2014; Thoroddsen, 2002; Thoroddsen et al., 2008)

1.2.2 Impact onto static solids

Also the impact of droplets onto static solid surfaces shows a range of behaviours: from smooth spreading to violent splash dependent on the surrounding gas pressure (Xu et al., 2005) or surface roughness (Xu et al., 2007), or even bouncing on hydrophobic surfaces (Bird et al., 2013).

1.2.3 Other studies on impact

In addition, some studies have focused on other aspects of the problems, like the angled impact of solid bodies onto liquid surfaces or oblique water-entry events (Howison et al., 2004; Korobkin, 1988; Moore et al., 2012; Sun and Wu, 2013).

1.2.4 Moving substrates

Although most of the mentioned studies approach the problem of stationary substrates, droplets frequently impact moving substrates instead. This can be seen both in nature and industrial applications: rain droplets falling on moving bodies of water, high-speed inkjet printing or spraying/painting onto moving substrates which may be dry or already wet (Derby, 2010).

Some studies of liquid impact onto moving solid substrates have arisen, showing that the previously known behaviours of splashing or bouncing can be controlled by adjusting the new variable of the problem: the speed of the substrate (Bird et al., 2009; Lhuissier et al., 2013).

1.2.5 Governing parameters

Previous studies on impact of droplets have shown that the appearance of splashing depends on the dynamics of the lamella (the liquid sheet formed after impact) (Thoraval et al., 2012). The resulting dynamics can be categorised according to the splashing number K, defined as $K = We\sqrt{Re}$. It depends on two other dimensionless groups: the Reynolds (Re) and the Weber (We) numbers, defined as $Re = \rho r v_n / \mu$ and $We = \rho r v_n^2 / \sigma$ respectively, where ρ, μ and σ are the density, viscosity and surface tension of the liquid and v_n and r are the impact speed and radius of the droplet.

The Reynolds and Weber numbers quantify the ratios of inertial forces to viscous and surface tension forces respectively. For impacting droplets, they describe the relative importance of the impact inertia over the viscous forces, which tend to decelerate the liquid, or surface forces, which tend to break up the expanding liquid rim of the lamella.

These dimensionless numbers have been demonstrated to govern not only the impact onto static substrates, but also the impact onto moving solids. In this case, the critical value of K that leads to splash also depends on the ratio between the tangential and the impact velocity (Bird et al., 2009).

1.3 Additive manufacturing

Additive Manufacturing (AM) consists in building three-dimensional objects layer by layer by joining each layer to the previous one. It is also known as Layered Manufacturing (LM) or Solid Freeform Fabrication (SFF), and it has evolved from early rapid prototyping techniques (Chua et al., 1998).

There is a wide variety of AM techniques, which are becoming very popular because they are flexible, highly automated, do not require the use of complex tooling, and impose nearly no limitation to the object shape (Gibson et al., 2010). AM techniques can produce functional objects of different materials, polymers being the most common ones so far. AM is especially adequate for objects with complex shapes and small production volume.

1.3.1 Additive manufacturing for metals

The use of AM for metallic parts has received growing attention in the medical, aeronautical (Murr et al., 2010), and manufacturing industries (Choi and Chang, 2005).

AM techniques for producing metallic parts can be classified into two groups (Gibson et al., 2010; Gu et al., 2012):

I. Those that spread a layer of metallic powder and then consolidate it to build the manufactured object cross section. Some examples are Selective Laser Sintering (SLS), Selective Laser Melting (SLM), Electron Beam Melting (EBM) (Murr et al., 2010) and 3D printing (Williams et al., 2011).

II. Those that directly deposit the metal corresponding to the cross section and, if necessary, auxiliary support structures. Some commercial techniques within this group are Direct Metal Deposition (DMD), Laser-Engineered Net Shaping (LENS), and Direct Light Fabrication (DLF).

1.3.1.1 Drop production techniques

Drop production techniques, such as inkjet printing, can be regarded as a subcategory of Direct Metal Deposition (DMD) methods. The use of drop production systems in AM is well established for polymeric materials and it is receiving growing attention in the application to low/medium-melting-point alloys.

The drop generator consists of a crucible where the alloy is melted and overheated. The crucible is pressurized by an inert gas on the top, and the molten metal emerges through a nozzle at the bottom. To prevent metal oxidation, the drop generator is mounted onto a chamber with an inert or low-oxygen concentration atmosphere. Drops are generated following two strategies: discrete drop or Drop on Demand (DoD) production (Cao and Miyamoto, 2006; Cheng et al., 2005; Fang et al., 2008) and continuous drop formation (Chao et al., 2012; Jiang et al., 2010). In both cases, the drop diameter ranges from one to two times that of the nozzle.

1.3.1.1.1 Drop on demand

In DoD, the droplet is squeezed out through the nozzle orifice by a mechanical pulse only when it is demanded, and it is directly deposited onto a movable substrate. This mechanical pulse can be produced by valves (Cheng et al., 2005) and pneumatic actuators (Fang et al., 2008), among other devices. Drops of indium, tin, lead, and zinc with diameters between 0.17 and 0.6 mm have been produced on demand (Cheng et al., 2005). The droplets could be placed in arbitrary patterns by coordinating the droplet formation with the movement of an x-y stage placed under the droplet generator. The influence of both the droplet and substrate temperatures and the droplet diameter on the metallurgical bonding has been studied experimentally (Fang et al., 2008).

1.3.1.1.2 Continuous droplet stream

In the continuous droplet stream method, a jet of molten metal emerges from the nozzle and breaks up into droplets under the influence of a mechanical disturbance. This disturbance can be imposed by a pneumatic actuator (Chao et al., 2012) or by a rod submerged into the crucible and connected to a piezoelectric device (Jiang et al., 2010). The jet is usually electrically charged to avoid the coalescence of the resulting droplets and to control their deposition (Luo et al., 2008). Droplets of aluminum (Orme and Smith, 2000) and Sn63-Pb37 (Luo et al., 2008) alloys, among others, have been produced from metallic jets with nozzles typically between 100 μm (Jiang et al., 2010) and 150 μm (Luo et al., 2008) in diameter, although smaller orifices have also been used (Lee et al., 2008).

1.4 Generation of PDMS microparticles

1.4.1 PDMS uses

Polydimethylsiloxane (PDMS) is a silicon-based organic polymer that has become incredibly popular due to its unique properties: good optical transparency, flexibility, non-toxicity, chemical inertness, thermal stability, biocompatibility, and permeability to gases (Johnston et al., 2014; Mata et al., 2005; Seo et al., 2013; Wang et al., 2014). Its industrial applications range from contact lenses to shampoos, caulking, lubricating oils and heat-resistant tiles, but also micro-electro-mechanical systems (MEMS) have benefited of PDMS deformability to create flexible microstructures, such as micropumps, microvalves or flexible micropillar arrays for force measurements (Fujiwara et al., 2010; Ghanbari et al., 2012).

Nevertheless, PDMS is receiving the greatest attention for its use in biomedical applications (Cardoso et al., 2018; Pinho et al., 2016), through the fabrication of microfluidic devices to investigate several flow phenomena in microvessels (Abkarian et al., 2008; Leble et al., 2011; Lima et al., 2012, 2008), to perform cell separation (Hou et al., 2010; Pinho et al., 2013; Tanaka et al., 2012; Tripathi et al., 2015) and deformability analysis (Bento et al., 2018b; Faustino et al., 2014; Partola et al., 2017; Rodrigues et al., 2015; Yaginuma et al., 2013), or even to culture endothelial cells (Huh et al., 2012; Ohashi and Sato, 2012; Shin et al., 2004).

1.4.2 PDMS particles and applications

Not only PDMS microfluidic devices are widely applied, but the production of monodisperse particles of PDMS is also attracting an increasing interest among researchers. Flow-focusing-based techniques have enabled the production of PDMS particles of hundreds of microns in size with different functions: from discrete oxygen sensors (Jiang et al., 2012), to shell-like particles with tunable elasticity (do Nascimento et al., 2017) or with amphiphilic behaviour (Zhao et al., 2011). These particles have been also characterized (Carneiro et al., 2016) or studied while flowing through constrictions (do Nascimento et al., 2017).

The control over the size or other mechanical properties of such microparticles would make them suitable for different biomedical applications, including blood analogue fluids (Calejo et al., 2016; Pinho et al., 2017), magnetic hyperthermia (Kalambur et al., 2005; Rodrigues et al., 2016a; Saidur et al., 2011) or contrast agents for magnetic resonance imaging (Kalambur et al., 2005). The latter applications rely on the potential of PDMS microparticles to encapsulate and work as delivery vehicles of fluorescent and magnetic nanoparticles.

When using nanoparticles with high thermal performances, such encapsulation ability would widen the application of PDMS particles to many fields other than biomedicine: electronics or engine cooling (Saidur et al., 2011; Yi et al., 2014), solar thermal energy (Khullar et al., 2014; Verma and Tiwari, 2015) or cooling and heating in buildings (Saidur et al., 2011).

1.4.3 Blood analogues

Among the applications of PDMS microparticles, the production of blood analogues deserves special attention. The study of blood flow through microchannels is crucial to improve our understanding about different phenomena happening in the human microcirculatory system (i.e., vessels with diameters smaller than 300 μm). Nevertheless, the use of *in vitro* blood implies some difficulties, such as coagulation and sample storage. These obstacles have promoted the development of fluids with rheological properties similar to real blood: the blood analogues (Sousa et al., 2011).

Most typical blood analogues in experimental flow studies are either newtonian, using a mixture of glycerine and water, or non-newtonian aqueous solutions based on xanthan gum and polyacrylamide (Anastasiou et al., 2012; Campo-Deaño et al., 2013; Sousa et al., 2011). However, they only replicate the rheological behaviour of blood and not other phenomena.

In order to reproduce multiphase effects of blood, particulate solutions are needed. Particles contained should mimic key structural attributes (size, shape, and mechanical properties) of red blood cells (RBCs), which are the most abundant cells in blood with a contribution of around 45% by volume (Lima et al., 2012). Some characteristic features found *in vivo* for microcirculation of RBCs are their reversible deformability or their migration to the vessel centre, resulting in the formation of a cell-free layer (CFL) close to the walls (Bento et al., 2018a; Lima et al., 2012; Maeda, 1996; Secomb and Pries, 2013; Sun et al., 2015).

Particulate blood analogues are hence aimed to replicate such blood phenomena. The main challenge in their development lies in the production of RBC-like particles. Some researchers designed synthetic particles that mimic size and shape of RBCs (Doshi et al., 2009; Ju et al., 2017; She et al., 2013), but mechanical properties were still far away. In particular, deformability is a key property that should be reproduced and has been therefore evaluated with different means, mainly by making the particles pass through narrow channels (Chen et al., 2012; Cui et al., 2014; Doshi et al., 2009; Sun et al., 2015) or constricted environments (Anselmo et al., 2015; Sun et al., 2015; L. Zhang et al., 2012). Different materials have been succesfully used to fabricate tunable elasticity particles: from hydrogels (Cui et al., 2014; Merkel et al., 2011) to silicon (Vilanova et al., 2013).

This thesis, considering the inherent properties of PDMS, proposes this material as a suitable candidate to develop such flexible microparticles, and therefore blood analogue fluids. In contrast with previous studies of elastic microparticles, which only assess their deformability, other blood flow phenomena will be verified for the produced PDMS microparticles.

1.5 Nozzles as the core element

1.5.1 Use in microfluidics

Nozzles are extensively used in microfluidics in order to produce drops, jets, bubbles and other fluid shapes. Microfluidic devices usually include one or multiple nozzles that need to be correctly positioned and aligned to obtain the desired device performance. The geometry, material and manufacturing process for the nozzles is mostly determined by the requirements of the particular application.

The range of practical applications where nozzles are used is really wide: devices for nanofiber production by electrospinning (Varesano et al., 2009), machines for multi-material three-dimensional printing by drop on demand (Li et al., 2009), or any drop generation technique that is based on Flow Focusing (Gañán-Calvo, 1998), such as devices to produce double emulsions for the food and cosmetic industry (Utada et al., 2005) or the Gas Dynamic Virtual Nozzle (GDVN) (DePonte et al., 2008). Particular applications of GDVN are those related to produce straight jetting for X-ray laser sample delivery (Nelson et al., 2016).

1.5.2 Importance of nozzle characteristics

In most applications, the flow through the nozzle is affected by the size, shape and surface roughness of the nozzle. In some cases, controlling these parameters is of the uttermost importance for the correct performance of the device.

For example, one of the fundamental obstacles to reduce the jet diameter produced by the GDVN is the so-called absolute whipping (Acero et al., 2012). This instability makes the meniscus swing violently while emitting the jet, which completely alters the formation of droplets downstream. Essentially, absolute instability arises when the component parallel to the nozzle axis of the air stream momentum exceeds a certain threshold. This component can be reduced by properly adjusting the nozzle shape. Therefore, controlling the inner shape of the nozzles will widen the range of stability of the GDVN device and the spectrum of applications.

In general, each particular device will require different nozzle characteristics, thus defining the geometry, material and manufacturing process needed to produce the nozzle.

1.5.3 Election of nozzle material

Polymer materials, due to their low cost and easy manipulation, have been chosen to produce micronozzles by different processes. For example, by stereolithography (Morimoto et al., 2009) or soft-lithographical techniques to produce a master for molding the final GDVN devices (Trebbin et al., 2014). Three-dimensional printing, whose resolution has increased in the last years, has been also used to produce photoresist GDVN devices (Nelson et al., 2016). Different techniques and apparatus have been reported to produce direct emulsification devices (Vladisavljević et al., 2012): from devices built from polymeric materials by using MEMS technologies, to assemblies that also include glass capillary nozzles.

The use of glass and ceramics in other applications is motivated by the need for higher mechanical and/or chemical performances. That is the case, for instance, of research dealing with direct deposition of metal (Vega et al., 2014). Ceramic nozzles have been produced by injection molding for GDVN devices for serial crystallography at X-ray Free-Electron Lasers (Beyerlein et al., 2015; Piotter et al., 2018). Sapphire nozzles are used, for example, at the bottom of the crucible of a drop-on-demand equipment (Cheng et al., 2005).

Among ceramic materials, glass nozzles offer some advantages that make them adequate for some applications, such as their chemical inertness, their smooth surface or their transparency, which allows observation of the fluid flow in the experiment. Borosilicate glass is a very common choice because its softening temperature is low enough to produce nozzles inexpensively. In addition, it has a low cost and adequate mechanical and thermal properties for a wide range of experiments. Borosilicate glass nozzles have been successfully used for direct deposition of a copper colloidal solution for electronic connections (Khan et al., 2012), or to produce low melting point metal droplets from a metal wire by induction heating (Vega et al., 2014).

1.5.4 Manufacturing methods for glass nozzles

In order to produce borosilicate glass nozzles, traditional glass working methods are used, since they are simple and effective. Starting from commercial capillaries, these often handcraft processes produce channel shapes with a desirable smoothness, similar to that of a liquid free surface.

The most common methods are pulling and fire shaping. The former achieves the diameter reduction by heating the central portion of the capillary first, and then pulling from its edges. So, two nozzles are produced at the same time, which may be separated by breakage or cutting. On the other hand, fire shaping uses a flame to heat the tip of the capillary up to a temperature for which the surface tension forces overcome the viscous ones, therefore causing the glass flow to reduce its free surface and internal diameter.

The geometry of the nozzles produced by these methods is radically different, as shown in Figure 1.4. Pulling produces convergent needle-shaped nozzles or pipettes with a significant increase of the length and decrease of the outer section, whereas fire shaping produces convergent-divergent nozzles shorter than the original capillary with a limited reduction in the outer diameter.

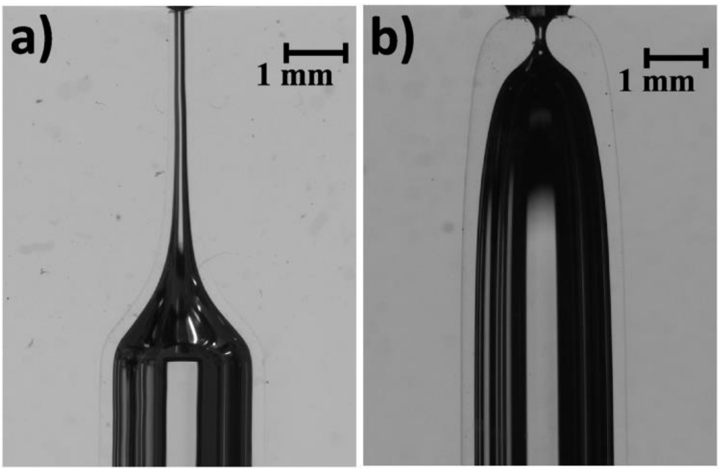

Figure 1.4 Nozzles of neck diameter ~200 μm manufactured by pulling (a) and fire shaping (b) from a borosilicate capillary of 2.77 mm inner diameter.

1.5.4.1 Pulling

The pulling method has been extensively used to produce pipettes for biological and medical studies with a high pipette consumption rate. For that reason, many commercial equipments have been developed, which are supplied with a cookbook providing the recommended process parameters to obtain a certain geometry. This type of equipment is also used to fabricate nozzles (or pipettes) to be assembled in microfluidic devices.

Before starting the pulling cycle, the capillary is cut to the desired length and gripped by two clamps, one at each side of the heating zone. The heat source (it may be a torch, a metallic filament or a CO_2 laser) will heat the material enough for the capillary to be stretched and get a thinner section. The pulling stage may continue until the capillary breaks into two pipettes or may stop earlier if the desired section is achieved, in which case a cutting device is needed.

The pulled nozzle geometry is usually characterized by the tip diameter and the taper length (or angle). They depend on the material of the capillary, its initial geometry (inner and outer diameter) and the fabrication cycle parameters (heating temperature or time, and the pulling velocity or force).

Although pulling is a well-established method, that has been developed commercially, it has several limitations:

I. Exact replication of the nozzle geometry from pull to pull is difficult (Grams et al., 2006). Specifically, this affects the tip taper, since even the two nozzles from the same pull have different lengths. There is also a variability in the resulting tip diameter (Grams et al., 2006; Malboubi et al., 2011), wich may be acceptable for some applications.

II. Pulled nozzles present a displacement or misalignment distance d_{mis} between the tip and the capillary axes (Levenstein et al., 2016) that may affect the proper alignment of the elements of the device, as shown in Figure 1.5. This turns to be very relevant for experimental devices where the nozzle is mounted by the capillary outer surface and the successful production of emulsions depend on the correct alignment of the orifices (Bayram et al., 2018; Gu et al., 2011; Utada et al., 2005).

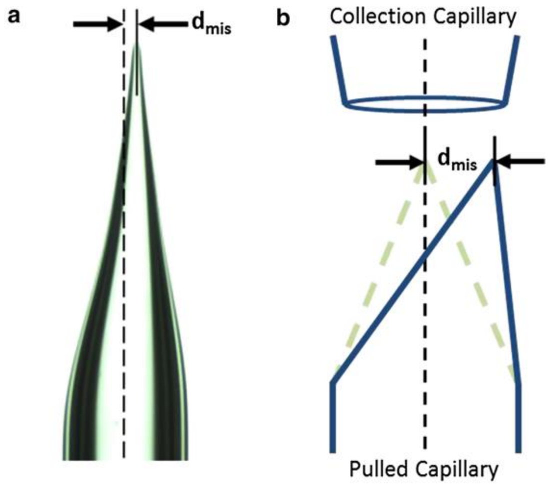

Figure 1.5 Misalignment of a pulled nozzle. (a) Optical micrograph with d_{mis} ~100 µm. (b) Schematic diagram of pulled (*bottom*) and collection (*top*) capillaries illustrating the effect of d_{mis} even when capillaries are axially aligned. Taken from Levenstein et al. (2016).

III. The edge of the pulled nozzles may be sharp due to the cutting or breaking procedure, or may present an unacceptable surface roughness that depend on the process parameters (Malboubi et al., 2011). This may make them unsuitable for particular applications, so normally a finishing process is necessary.

   a. Mechanical grinding of the tip is usual, but a thorough cleaning is required afterwards to avoid clogging of the nozzle (Braun et al., 1997).

   b. Another finishing option is flame polishing, in which the tip of the pipette is heated to turn its edge blunt. The heating element can be a metal filament (commercial microforges) or a flame. The tip diameter may be reduced due to the heating, but as a finishing operation, normally no changes in tip geometry are desired (Yaul et al., 2008).

IV. The overall process variability makes it necessary to validate each individual nozzle, either after or during manufacturing. Several methods have been developed to characterize the size and geometry of the pipette tip (Tognoni et al., 2016), normally based on automated microscopy (Stockslager et al., 2016). It would be desirable to find a sufficiently reproducible method that eliminates the need of this validation operation.

V. The geometrical parameters of the pulled nozzles cannot be controlled independently. For example, for the same heating time, a higher pulling velocity increases the tip length and decreases the tip diameter. So research is still carried on to investigate how the process parameters affect the pipette shape, how they relate to each other and to try to reduce that dependence (Pak et al., 2011; Tamizhanban et al., 2014; Wang et al., 2016).

VI. Even if the previous limitations are sorted out, the geometry of pulled nozzles may still not be convenient for some applications:

   a. The nozzle length increases significantly with the diameter reduction of the nozzle. So, large diameter reductions result in nozzles of an excessive length.

   b. Pulled nozzles show a reduced glass thickness around the long channels, which may produce nozzle breakage when dealing with high viscosity liquids. In these cases, the length rises the necessary pressure for the liquid to flow, and nozzle strength is reduced with such glass thickness.

c. They also present a large cooling surface, that may lead to clogging problems when dealing with molten materials, due to partial solidification along the nozzle.

Some researchers have proposed alternative variations to the standard pulling process, in order to get more convenient nozzle geometries (basically shorter nozzles). Nevertheless, some of the developed options, such as a four-step cycle apparatus (Xie et al., 2015) or the pressure polishing method (Benedusi et al., 2011; Goodman and Lockery, 2000), might add complexity to the manufacturing process.

1.5.4.2 Fire shaping

The second common method for manufacturing glass nozzles is the fire shaping procedure. Although similar to fire polishing -used as a finishing operation for pulling (as previously explained in point III.b)-, fire shaping is not used for finishing, but for directly producing convergent–divergent nozzles. Therefore a significant change in diameter is pursued here.

In fire-shaped nozzles, the diameter reduction occurs in a short length (Figure 1.4), thus overcoming geometry-related limitations of pulled nozzles (limitation VI). In addition, no finishing operations are required in fire shaping to get a smooth nozzle, as it would happen for pulling (limitation III). Only when convergent nozzles are desired, the divergent part must be mechanically polished away.

Many microfluidic devices include glass fire-shaped nozzles (Boutet et al., 2012; DePonte et al., 2008; Switzer, 1991). In several cases, the devices combine both fire-shaped and pulled nozzles, normally used as the collection and the injection tube respectively (Levenstein et al., 2016; Utada et al., 2005; Weierstall et al., 2012).

In spite of the wide use of fire shaping to fabricate nozzles, the process is still done mainly manually. The use of commercial equipment, such as microforges, is still limited to finishing operations as fire polishing for pulled pipettes. Therefore, the variability found for fire-shaped nozzles size and shape, and the lack of symmetry, have motivated in many cases the use of a different fabrication method, which implied a change in nozzle material. In contrast, Paper VI in this thesis intends to automate fire shaping in order to assess its performance systematically, while still using borosilicate glass as raw material.

So far, researchers have traditionally used a vertical flame, with the capillary heated either vertically with its end at the top of the flame (*TVF*) (DePonte et al., 2008; Switzer, 1991; Utada et al., 2005) or horizontally with its end on the side of the flame (*SVF*) (Montanero et al., 2010; Vega et al., 2014), which yields shorter nozzles. In this thesis (Paper VII), a new fire shaping approach is proposed, where a rotating vertical capillary is heated at the Top of a Lateral Flame (*TLF*). The three different fire shaping approaches are depicted in Figure 1.6.

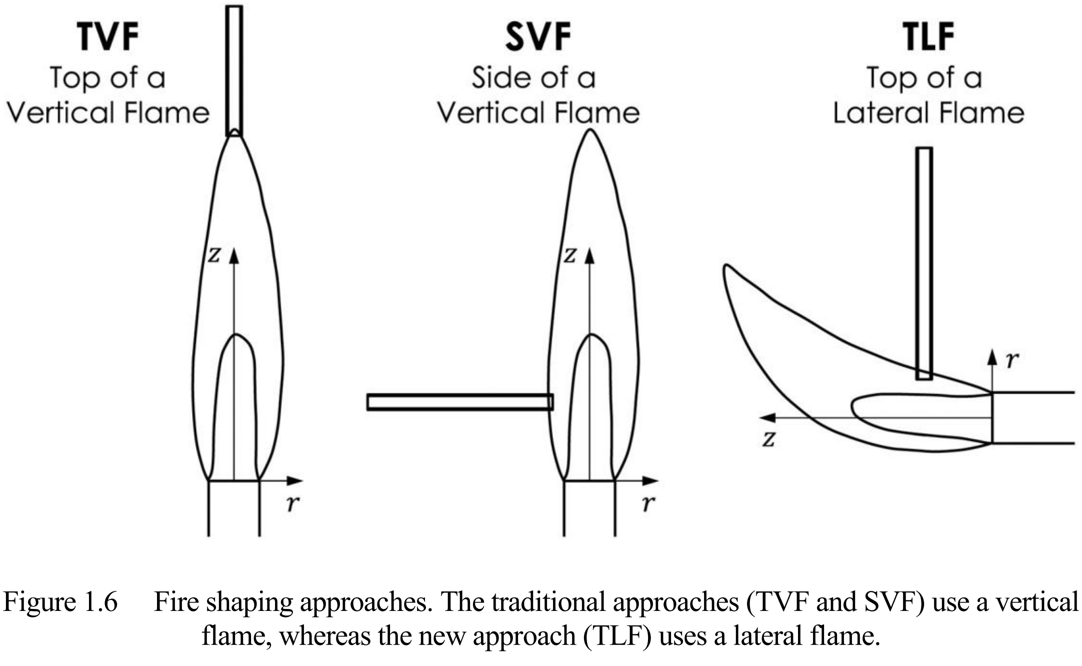

Figure 1.6 Fire shaping approaches. The traditional approaches (TVF and SVF) use a vertical flame, whereas the new approach (TLF) uses a lateral flame.

1.6 Interfacial tension measurement

Methods to measure the interfacial tension between a liquid and another fluid are usually based on the competition between the capillary and gravitational forces. Basically, these methods, through image analysis of a certain capillary system (liquid bridge, liquid lens or a pendant/sessile drop/bubble) at equilibrium, measure the gravity effect on the shape and then deduce the interfacial tension value (Hoorfar and W. Neumann, 2006). The Bond number

$$B = \frac{|\Delta\rho| g L^2}{\sigma} \tag{1-1}$$

determines the magnitude of the interface deformation caused by gravity. In its definition, $\Delta\rho$ is the difference between the densities of the two fluids, g is the gravitational acceleration, L is a characteristic length of the capillary system, and σ is the interfacial tension.

The main limitation of these drop shape methods appears for very small values of the Bond number. In such cases, the capillary system adopts the corresponding weightless shape independently of the interfacial tension value, so the interface shape cannot be used to infer the value of σ for $B \to 0$, even if the algorithm has properly converged to a certain solution of σ (Jaensson and Vermant, 2018; Saad and Neumann, 2016).

There are three scenarios where the Bond number takes very small values:

- Density-matched liquids ($\Delta\rho \to 0$)
- Microgravity conditions ($g \to 0$)
- Very small capillary shapes ($L \to 0$)

In the first case, when densities are very similar, there is an additional source of error for drop shape techniques: small errors in the measurement of densities will lead to significant relative errors in $\Delta\rho$, and therefore in the interfacial tension σ.

1.6.1 Overcoming limitation of drop shape tensiometry

Some attempts to solve this long-standing problem are based on alternative functional principles. For example, on the balance between a known overpressure in a drop submerged in a liquid bath and the interfacial tension force (Peters and Arabali, 2013). In other cases, the interface gets stretched by different means - depositing a small spherical silica particle (Neeson et al., 2014) or applying an electric field (Bateni et al., 2004) - so the interfacial tension can be measured from the resulting deformation that would not appear otherwise for such low Bond numbers.

Another approach consists in taking the system out of equilibrium to determine the interfacial tension from its dynamical response. For any capillary system, the resonance frequency is known to significantly depend on the interfacial tension. In the case of liquid bridges, this dependence involves the liquid bridge density, and, to a much lesser extent, the difference in densities $\Delta\rho$ between the bridge and surrounding fluid. Therefore, significant relative errors of $\Delta\rho$ do not translate into noticeable errors of the interfacial tension, thus overcoming a known source of errors for drop shape techniques.

For low and moderate viscosities liquid bridges, the transfer function (the ratio of the output to the input in the vibration response) exhibits a sharp peak at resonance, thus allowing the precise determination of the resonance frequency. This principle has been successfully applied to measure the interfacial tension of density-matched liquids by vibrating axially a liquid bridge of one of them submerged in the other, although the accuracy of the method was not assessed (Perales and Meseguer, 1992).

Nevertheless, the first transfer function peak observed in the lateral vibration of a liquid bridge is much higher and thinner than its axial counterpart (Ferrera et al., 2016), thus making the lateral vibration a much better candidate to measure the interfacial tension of density-matched liquids. The major obstacle to implement this method is to calculate the resonance frequency as a function of the interfacial tension and the rest of governing parameters, given the complexity of the theoretical problem involved.

In this way, Paper VIII proposes the Lateral Vibration Tensiometer (LaViT), which greatly simplifies such problem by equating the first resonance frequency to the first eigenfrequency (natural frequency) of the lateral ($m = 1$) mode. That eigenfrequency had been previously calculated analytically for inviscid cylindrical liquid bridges (Sanz and Diez, 1989), and the approximation is accurate for low and moderate viscosities.

2 OBJECTIVES

The main objectives of the present work are based on the general need of studying the fundamental aspects of droplet generation and impact. Nevertheless, this thesis can be regarded as application-driven, since it aims to offer practical insights into certain applications in engineering, such as biomimetics or additive manufacturing. This section comprises the gaps found for each field in the introduction and the set objectives to overcome in each paper.

2.1 Paper I: Droplet impact onto moving liquids

Although other scenarios for impacting droplets have been successfully studied through the years (static pools, static or moving solids), the impact onto moving liquids is still largely unexplored. Some practical difficulties might have held back studies in this area, especially the generation of a uniformly moving liquid pool that allows proper visualization of the impacting region.

Paper I overcomes such limitations by presenting an experimental setup to identify different regimes of behaviour for the impact of droplets onto moving pools of the same liquid.

2.2 Paper II: A novel technique to produce metallic microdrops for additive manufacturing

Paper II presents a novel technique to produce a continuous droplet stream of a low-melting-point alloy. The essential difference with respect to other methods described lies in the melting process occurring prior to the jet formation. Instead of using a crucible to maintain a reservoir of molten material, the tip of a metal wire is melted by an induction heating system as it is introduced in the nozzle.

Specifical objectives of this piece of work are:

I. To propose a new experimental setup that progressively heats a metal wire instead of using a crucible.
II. To characterize the wire tip melting in the induction coil.
III. To produce a quasi-steady metal jet by choosing the appropriate control parameters.
IV. To study the dynamics of the metal jet and its breakage.
V. To analyse the size of the metal droplets produced from the jet breakage.

2.3 Paper III: Generation of micro-sized PDMS particles by a flow focusing technique for biomicrofluidics applications

Whereas PDMS microparticles have been fabricated so far with dimensions in the order of hundreds of microns, some applications require them to be smaller. For example, to develop blood analogue fluids, PDMS microparticles must have close dimensions to the red blood cells (RBCs), i. e. below 10 µm. Objectives for Paper III are therefore:

I. To produce monodisperse PDMS microparticles below 10 μm with a needle-focusing technique (Acero et al., 2013).

II. To analyse the performance of such technique when working with viscous fluids as PDMS precursor.

III. To characterize the resulting PDMS microparticles.

2.4 Paper IV: Shrinkage and colour in the production of micro-sized PDMS particles for microfluidic applications

The diversity of applications for the generated PDMS microparticles (Paper III) requires a more complete understanding and characterization of the technique.

In particular, the shrinkage while curing was found to be significant, affecting the final dimension of the resulting microparticles. PDMS shrinkage is a highly variable phenomenon as many parameters are involved, especially when working in a multi-user environment without tightly controlled fabrication conditions (Moraes et al., 2009). Typically, it is characterized on a case-by-case basis and individual calibration or alignment methods are needed for each design (Lee and Lee, 2008). Shrinkage effect has been reported to increase with growing curing temperature, size, and mixing ratio of dilutant and curing agent (Jeong and Konishi, 2011; Lee and Lee, 2008); and also depends on the exposure to air (Lee et al., 2003). Nevertheless, previous studies focus on 2D structures at the millimetric scale, mainly molds or stamps, a very different geometry than that of microparticles.

On the other hand, some applications would benefit from the addition of colour to such small particles. The enhancement of contrast would make their visualization easier, for example, when flowing through microchannels (Bento et al., 2018b; Calejo et al., 2016; Rodrigues et al., 2015). However, just a few works can be found in literature about colouring PDMS, for example by embedding silicon nanowires into PDMS (Park et al., 2012) or by applying commercial pigments to PDMS micropillar arrays (Khare et al., 2015).

Taking into account the above, Paper IV is aimed:

I. To calibrate the shrinkage phenomenon for PDMS spherical particles of a few microns in size, exploring its dependence on the amount of curing agent in the PDMS precursor mixture.

II. To add colour to such particles in order to improve their later visualization/detection.

2.5 Paper V: Flexible PDMS microparticles to mimic RBCs in blood particulate analogue fluids

Blood analogues containing rigid particles have emulated some of the blood-flow phenomena that happen at both *in vivo* and *in vitro* environments (Calejo et al., 2016), but evidence shows that a close replication of all of them can only happen by using deformable microparticles.

Many studies have engineered deformable microparticles with different mechanical properties and biological behaviours, but none of them has shown evidence on how closely they mimic microscale blood-flow phenomena other than deformability.

Hence, Paper V checks whether PDMS microparticles manufactured by needle focusing (Paper III) verify such microcirculation phenomena, comparing them against human RBCs (both healthy and pathological) at similar *in vitro* conditions. Specifical objectives of this piece of work are:

I. To measure deformability for different types of PDMS microparticles (several crosslinking ratios and pigmentation) and human RBCs.

II. To obtain the steady shear viscosity curves with a rheometer, for the PDMS and RBCs suspensions.

III. To check the cell-free layer (CFL) effect and measure its thickness.

2.6 Paper VI: Borosilicate nozzles manufactured by reproducible fire shaping

The idea of fabricating a nozzle by heating a capillary with a flame seems straightforward. A clean-cut end of the capillary is brought in contact with the flame. The glass temperature rises, and the surface tension forces overcome the viscous ones causing the glass flow and the change in the shape. The glass flow shortens the capillary and reduces its inner diameter producing the nozzle. When the desired nozzle diameter is reached, the capillary is moved away from the flame and the cooling stops the shape change. At this moment, the heated capillary end has become a convergent–divergent nozzle with a smooth shape.

The apparent simplicity of this manufacturing process has made researchers produce fire-shaped nozzles mostly manually, with little control over the process. Not much work has been published about the relation between the nozzle shape and the process parameters.

Nevertheless, the underlying phenomena are really complex. In order to understand and control the governing parameters of fire shaping, Paper VI explores it in a systematic way through the following objectives:

I. To propose an experimental setup and procedure to fire shape nozzles through the two most common approaches: heating a horizontal capillary on the side of a vertical flame (SVF) and heating a vertical capillary at the top of a vertical flame (TVF).

II. To propose a complete characterization method to describe the geometry of the produced nozzles.

III. To analyse the flame and identify suitable working regions to manufacture nozzles.

IV. To study the performance of each fire shaping approach by analysing the shape and size of the resulting nozzles, and their reproducibility for the same manufacturing conditions.

2.7 Paper VII: A new fire shaping approach to produce highly axisymmetric and reproducible nozzles

Traditional fire shaping approaches present several limitations, even when tackled systematically with careful control of the parameters (Paper VI). The misalignment found for SVF or the lack of reproducibility in the size of TVF nozzles may discard fire-shaped nozzles for applications that strongly depend on the alignment of the elements or the neck diameter.

Nevertheless, fire shaping had been proposed as an alternative to pulling when the application required a different geometry than that of pulled pipettes, either in terms of the nozzle length, wall thickness or offset with respect to the capillary axis. Hence, fire shaping needs to be further explored to be presented as a controllable manufacturing process.

In this way, Paper VII proposes a new approach for fire shaping to overcome limitations found for SVF and TVF. It consists in heating a vertical capillary at the top of a lateral flame (TLF). This option can be evaluated through the following specific goals:

I. To propose an experimental setup and procedure for manufacturing nozzles by TLF.

II. To study the temperature profiles happening in the lateral flame and identify the best working region to produce nozzles.

III. To characterize the manufactured nozzles and evaluate their diameter reproducibility and symmetry.

IV. To compare TLF performance against previous fire shaping approaches: SVF and TVF.

V. To compare the results against the well-stablished method of pulling.

2.8 Paper VIII: A method for measuring the interfacial tension for density-matched liquids

Taking into account the limitation of drop shape techniques to measure the interfacial tension of liquids of similar density (section 1.6), Paper VIII makes use of the lateral vibration of a liquid bridge to determine its value.

In particular, this piece of work pursues the following objectives:

I. To propose a simple method (LaViT) to measure the interfacial tension of density-matched liquids.

II. To determine the best parameter conditions where LaViT is expected to work satisfactorily.

III. To assess the accuracy of such method and compare it against an established drop shape tensiometry method as Theoretical Fitting Image Analysis-Axisymmetric Interfaces (TIFA-AI) (Cabezas et al., 2006).

3 GLOBAL SUMMARY OF RESULTS AND DISCUSSION

3.1 Paper I: Droplet impact onto moving liquids

3.1.1 Experimental setup

A schematic view of the experimental setup is shown in Figure 3.1. The experiments consisted in the controlled production and visualisation of single droplets, which travelled vertically downwards onto a pool of the same liquid moving at a constant speed. The range of fluid properties and impacting speeds used in these experiments, once converted into dimensionless form, are well within the printability regime (i.e. where inkjetted droplets are known to occur) (Derby, 2010). Outside this range, surface tension or viscous effects are too strong to permit the production of individual droplets. The range of ratios between the tangential and normal speeds explored in this work were from 1.5 to 48.5.

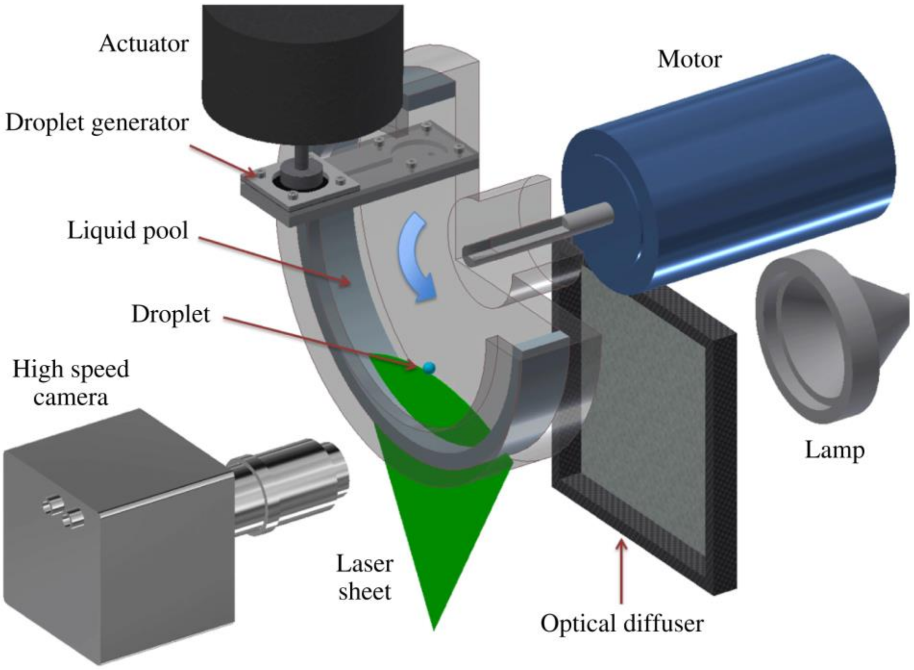

Figure 3.1 Experimental setup to study the impact of a droplet onto a moving pool of the same liquid.

3.1.1.1 Working fluids

The working fluids for both the droplets and pool consisted of water–glycerol mixtures with newtonian viscosities ranging from 1 to 200 mPa·s and surface tension values in the range of 61.9 to 70.8 mN/m. All the experiments were performed at 21.0 ± 0.2 °C under typical atmospheric conditions with air as the surrounding fluid.

3.1.1.2 Droplet generation

Single droplets of different sizes and speeds were formed either by dripping (i) or drop on demand (ii) with radius ranging from 1.0 to 2.2 mm. Experimental conditions were adjusted to produce near-spherical drops with shape aspect ratios > 0.9.

i. Simple dripping from polymethylpentene nozzles was used to produce impacting droplets with low impact velocities and large radius. Height and nozzle size were varied in this case to get different conditions.
ii. In order to achieve higher impact velocities (1.2 to 1.7 m/s), droplets were produced by means of a large-scale drop-on-demand generator (Figure 3.2), which is a modification of the one described by Castrejón-Pita et al. (2011). The system uses an electromagnetic shaker to transmit single-pressure pulses to the liquid reservoir through a rubber membrane. Therefore, liquid gets pushed out of a nozzle of 2.0 mm diameter. Droplet speed and size were controlled in this case by varying the actuator parameters.

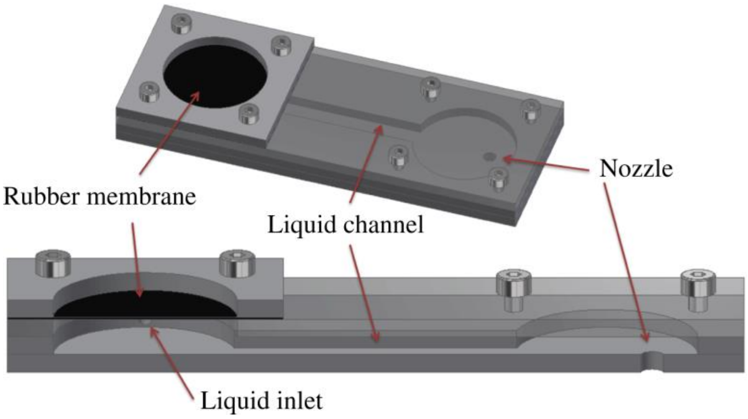

Figure 3.2 Cutaway view of the drop-on-demand generator device

3.1.1.3 Pool

The moving liquid pool was formed by an annular channel (internal radius of 70.0 mm and width of 20.0 mm) that rotates about a horizontal axis: the shaft of a DC electric motor. The channel was constructed of transparent acrylic in order to permit visualisation.

Practical limitations restricted rotational frequencies to be within the range of 4.0–25.5 Hz. Below this range the centripetal force is not enough to overcome gravity and retain the liquid within the channel, whereas above this range the rotation of the motor was found to be unstable. The rotation frequency was monitored by a laser–photodiode pair (frequency control within ±0.02 Hz).

The fluid depth of 6.0 mm was kept constant throughout all the experiments and solid-body rotation was assumed. The tangential relative speed of the liquid surface (v_t) at the point of drop impact was therefore controlled by simply varying the rotation frequency.

3.1.1.4 Visualization

The experimental setup allowed capturing the dynamics above and below the droplet–pool interface with different high-speed imaging techniques.

Greyscale shadowgraphy helps to clearly determine the impact dynamics over the surface of the liquid pool. Figure 3.1 shows the position of the lamp and an optical diffuser to get backlight illumination. In contrast, colour imaging requires front illumination, so the lamp was placed oblique to the camera and pointing towards the impact point.

In order to monitor the internal dynamics of the drop at the contact line, thus capturing mixing at the interface, some experiments were visualized by combining colour imaging and laser fluorescence. For these cases, a < 100 mm-thick sheet of illumination was produced by a 532 nm 500 mW laser and directed to the impacting zone as shown in Figure 3.1. Small amounts of sodium fluorescein (< 0.02 wt.% concentration) were added to the droplet fluid. The addition of this dye has been reported not to modify the fluid properties within experimental error (Castrejón-Pita et al., 2012)

3.1.2 Experimental procedure

Once the system was set in motion and reached the desired rotation rate, the channel was filled with the working fluid with the help of a small funnel or a pipette, until the depth of the pool was adjusted. Great care was taken to avoid introducing bubbles to the liquid pool or to splash droplets onto the channel walls, since they would interfere with the visualisation.

A spin-up time of at least 10 min was allowed before starting the experiments. This proved to be enough for any surface irregularities to die out.

After producing the droplet, the whole impact event was recorded to be later analysed. A Matlab routine was created to extract the droplet impact speed and radius for each experiment.

A typical experimental routine consisted in keeping the rotation constant while varying the impact speed of the drop. The rotation rate was then increased, and a new series of experiments carried out.

3.1.3 Regimes

The experiments show that the impact behaviour could be classified into four different regimes: droplet surfing, smooth coalescence, lamella jetting and splashing. The regimes of lamella jetting and splashing present features previously unreported.

I. **Surfing** is commonly found in higher viscosity liquids, low to medium impact speeds and high rotational velocities. The impacting drop never fully penetrates the liquid pool but bounces without coalescing and remains levitated by a thin film of air, just above the surface (Figure 3.3 a). Occasionally, a slight loss of liquid from the drop occurs upon impact, which becomes incorporated into the moving pool. The airborne drop moves slowly across the liquid surface in the direction of rotation of the pool, oscillating back and forth before reaching an equilibrium point, where it remains in a stable state, with the drag forces balancing the tangential component of its weight (Figure 3.3 d). A similar scenario had been formerly observed for tiny drops that remained hydroplaning over a thin layer of rapidly moving fluid (Thoroddsen and Mahadevan, 1997).

II. In **smooth coalescence**, the drop penetrates the pool smoothly and rapidly, with all its volume fully merging with the pool. Little mixing is observed at the interface and a clearly visible smooth lamella is often formed opposite to the direction of motion (indicated in Figure 3.3 b). The maximum penetration depth reached by the drop upon impact (Figure 3.3 e) is found for low rotation frequencies and high impact speeds. Such penetration is always below half of the total depth of the pool, ensuring wall effects to be kept to a minimum.

III. In **lamella jetting**, the drop partially coalesces at the first point of contact, but not all its volume merges into the pool (Figure 3.3 c). A large proportion of the drop remains surfing over the surface (or bounces back after the initial impact) and is dragged by the moving pool beyond the original impact point. A liquid filament is formed between the droplet and the pool, which remains connecting them, even if the droplet lifts and separates from the moving surface (Figure 3.3 f). The fluid in the drop continues to coalesce with the substrate through the ligament.

IV. In the **splashing** regime, the rear part of the impacting drop rapidly coalesces with the pool while a lamella emerges from the front of the drop. The inertia of the drop overcomes viscosity and surface tension, which leads to the breakup of the rim of the lamella into droplets. As shown in Figure 3.4, vortices are shed at the drop–pool contact line within the first moments of contact. Vortex shedding was only observed in the splashing regime, and they point towards a Kelvin–Helmholtz-type shear-driven instability (with all vortices in the chain with the same sign), in contrast with the von Kármán vortex street (of alternating sign) previously observed (Castrejón-Pita et al., 2012; Thoraval et al., 2013, 2012).

Figure 3.3 shows the temporal evolution of three of the regimes. Supplementary movies available online at https://doi.org/10.1017/jfm.2016.672 can probably help for a better understanding of the different behaviours.

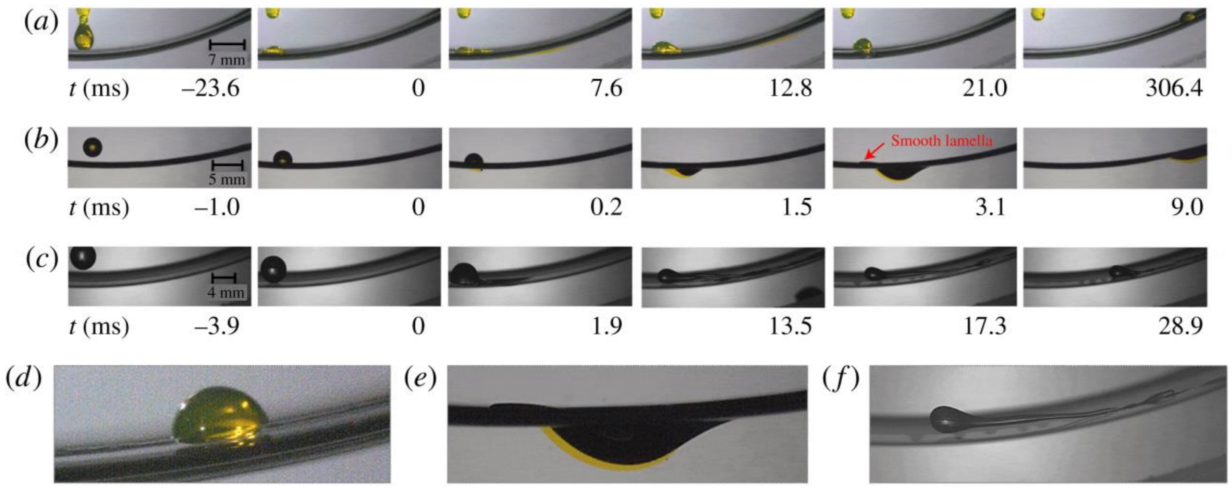

Figure 3.3 Temporal sequence for three different impact regimes. (a) Surfing. (b) Smooth coalescence. (c) Lamella jetting. Images (d–f) show frames for the sequences in (a–c) at higher magnification.

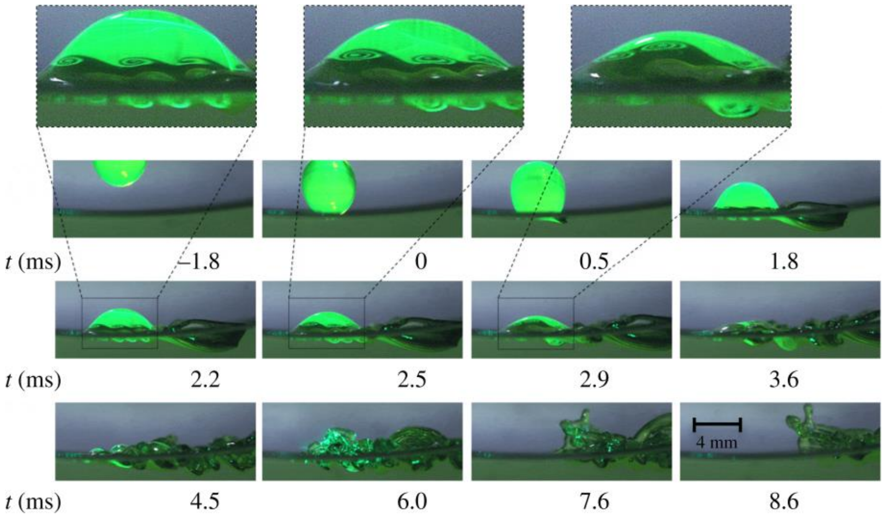

Figure 3.4 Time evolution of an impacting droplet in the splashing regime. Vortex shedding can be observed thanks to laser fluorescence imaging.

The impact behaviours are determined by the ratio of the drop to surface velocities and the liquid properties. By choosing the appropriate dimensionless numbers, a regime diagram (Figure 3.5) can be constructed, in which distinct dynamical regimes are clearly identified. The dimensionless groups previously known to regulate splashing on static substrates (Thoraval et al., 2012), when defined appropriately in terms of the droplet speed relative to the liquid substrate, also govern the impact dynamics here. Therefore, the regimes group well when plotted in terms of the dimensionless groups $K = We\sqrt{Re}$ and $(v_t/v_n)(1/\sqrt{Re})$ where v_t is the (tangential) speed of the substrate.

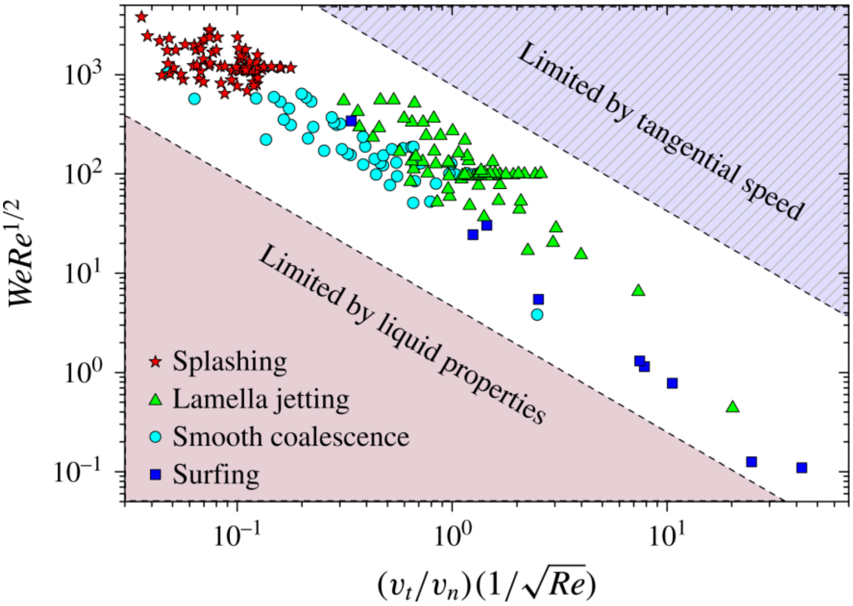

Figure 3.5 Regime diagram showing the different impact dynamics in terms of the relevant dimensionless numbers.

3.2 Paper II: A novel technique to produce metallic microdrops for additive manufacturing

3.2.1 Experimental setup

The progressive melting of the metal wire is achieved thanks to the elements in Figure 3.6. The converging nozzle through which the jet is emitted is manually formed and characterized following Montanero et al. (2010), with resulting orifice diameters d_0 ranging from 150 to 250 µm. A Sn95-Ag4-Cu1 (melting point: T = 217 °C) wire of 1.5 mm in diameter is introduced inside the inner capillary with a wire feeder driven by a stepper motor.

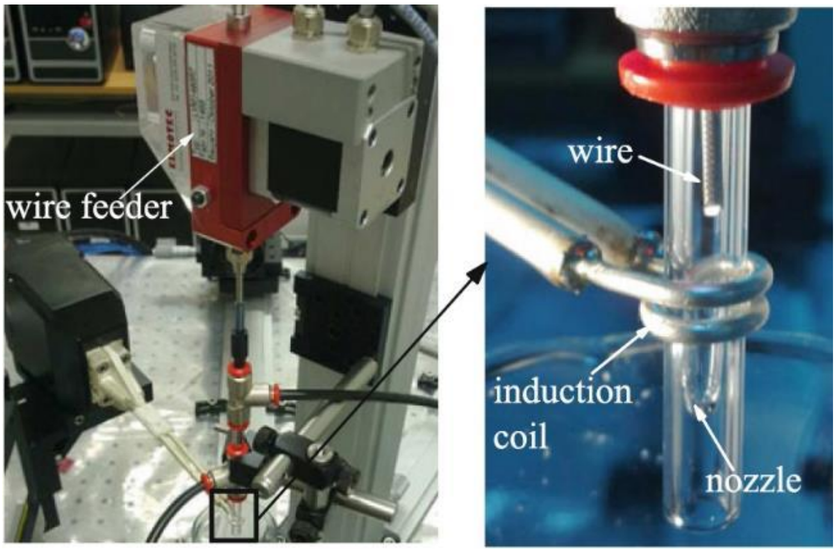

Figure 3.6 Main elements in the experimental setup

The induction heating system is typically used for industrial processes of heat treatment, brazing, and soldering on different types of metallic parts. It feeds the induction coil (C) and heating head (D) shown in Figure 3.7. These parts can be displaced by using a triaxial translation stage (E) to appropriately locate the induction coil with respect to the nozzle.

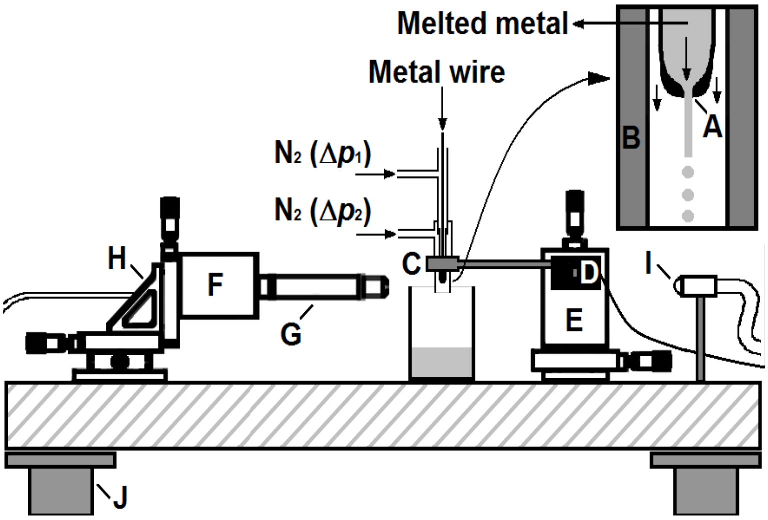

Figure 3.7 Sketch of the experimental setup for the proposed technique. (A) glass nozzle, (B) outer glass capillary, (C) induction coil, (D) heating head, (E) triaxial translation stage, (F) CCD camera, (G) optical lenses, (H) triaxial translation stage, (I) optical fiber, and (J) pneumatic anti-vibration isolation system.

Nitrogen is supplied at room temperature to both the inner and outer capillaries by applying the gauge pressures Δp_1 and Δp_2, respectively. The jet production process was automated with LabVIEW.

The performance of the device is assessed by means of the backlight optical imaging method (Vega et al., 2011). Images of the process are acquired at 30 fps using a CCD camera (F) equipped with optical lenses (G). To check the axisymmetry of the configuration, we use an auxiliary CCD camera (not shown in Figure 3.7) with an optical axis perpendicular to that of the main camera. In order to describe the jet breakage, the main CCD camera is replaced by an ultrahigh-speed CMOS camera and images are acquired at 10^4 fps.

3.2.2 Overview of the process

The jet formation consists of two processes, depicted in Figure 3.8, that must be necessarily decoupled:

I. Firstly, the wire tip must melt in the vicinity of the induction coil. As the wire tip approaches the coil at speed V, its temperature increases sharply until the melting point. Then, a pendant drop forms and hangs from the wire tip. The drop temperature continues to increase well above the melting point and the drop eventually falls into the nozzle, when its size is large enough for the gravitational force to overcome the surface tension. The metallic drops form a small pool which fills the nozzle.

II. Secondly, the metal pool is pushed by the nitrogen supplied to the nozzle at the gauge pressure Δp_1. That pressure excess will be mainly converted into kinetic energy, and thus, a jet is expelled through the nozzle orifice. The jet is shielded by a nitrogen stream driven by a small gauge pressure $\Delta p_2 << \Delta p_1$. (the role of Δp_2 is simply to establish the nitrogen shield and thus avoid the free-surface oxidation). Finally, the jet breaks up into droplets due to the capillary waves growing over the free surface.

Both processes take place simultaneously and continuously, since the liquid ejected in process II gets replaced by the dripping onto the pool. Therefore, the small liquid pool reaches quasi-steady conditions thanks to the continuous refill through wire melting.

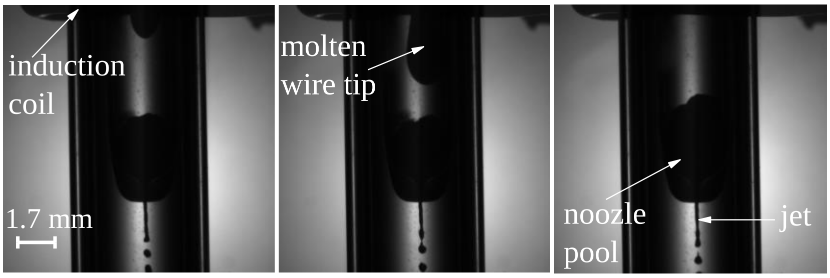

Figure 3.8 Three consecutive snapshots of the two processes leading to the metallic jet formation.

A quasi-steady jet production critically relies on the decoupling between the (thermal) melting and (dynamical) ejection processes described. There are two physical mechanisms which can couple these two processes: heat conduction between the wire tip and the pool and a significant dependence of the pool viscosity upon the drop temperature.

The first phenomenon precludes the system from reaching a steady regime because the cooling occurring when the liquid gets in contact with the nozzle would disrupt the drop formation if transmitted upstream. If the drop formation process does not take place in a continuous manner, the pool is not refilled at the appropriate rate, and a steady ejection is not feasible. Therefore, the induction coil is always placed well above the nozzle orifice (9 mm), so melted drops are totally detached from the wire when reaching the pool.

In the second place, above the melting point, metal viscosity significantly depends on temperature. Any cooling would make viscous forces dramatically increase in the nozzle, which could even block the flow through the nozzle orifice and make the pool level to raise towards the induction area. This nozzle clogging is avoided by heating the metal well above the melting point, so a high viscosity will not hinder the ejection.

3.2.3 Melting process

The wire tip melting was analysed as a function of the control parameters V (wire speed) and N (induction generator power). For this purpose, the nozzle was removed, so the drops directly falling from the wire tip could be studied.

Tests were done for two different induction coils: one with just one spiral and a double-spiral one. For each of them, three distinct working modes were identified for the melting process, as shown in Figure 3.9:

- Mode I corresponds to the periodic production of drops of approximately the same size.
- In mode II, the energy transferred to the wire tip is not sufficient to melt it completely. Metal elements in quasi-solid phase detach from the wire end.
- In mode III there is an excess of energy per unit volume captured by the wire and some undesirable effects appear: the resulting drops creep over the wire lateral surface and transport upwards their thermal energy, shifting up the melting region.

The double-spiral coil presents some advantages that restrict the rest of the study to this configuration. If two spirals are used, mode I is obtained for smaller N/V ratios, so energy is transferred more gradually and efficiently from the coil to the wire tip, thus improving the melting process. In addition, the area occupied by mode I significantly increases when the coil has two spirals, therefore widening the working region.

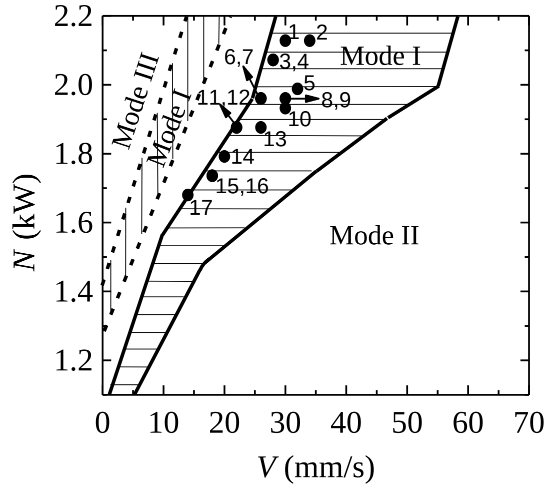

Figure 3.9 Drop production modes for wire melting. Regions marked with *vertical* and *horizontal lines* correspond to Mode I for one and two-spiral coils, respectively. The *dots* correspond to 17 steady jetting realizations.

In order to avoid the clogging of the nozzle, metal drops should be produced with a sufficiently high temperature, well above the melting point. Therefore, the boundary between modes I and III leads to the optimum results. The linear relationship $N = N(V)$ for such boundary represents the maximum energy per unit mass transmitted to the wire while yielding periodic dripping. For that reason, experimental realizations for steady jetting marked in Figure 3.9 tend to this boundary.

3.2.4 Jetting formation and breakage

Jets can be quasi-steadily emitted for different wire speeds V by appropriately setting the generator power N and the applied pressure drop Δp_1. Table 3-1 shows the corresponding values of the control parameters and nozzle orifice diameter d_0 for 17 different experimental realizations within melting mode I (Figure 3.9).

Table 3-1 Parameters for the steady jetting realizations in Figure 3.9

Realization	**V (mm/s)**	**N (kW)**	**Δp_1 (mbar)**	**d_0 (µm)**
1	30	2.13	170	217
2	34	2.13	180	225
3	28	2.07	180	194
4	28	2.07	190	193
5	32	1.99	300	181
6	26	1.96	320	169
7	26	1.96	360	149
8	30	1.96	290	178
9	30	1.96	285	179
10	30	1.93	185	208
11	22	1.88	305	152
12	22	1.88	290	154
13	26	1.88	320	169
14	20	1.79	265	160
15	18	1.74	285	141
16	18	1.74	280	140
17	14	1.68	190	156

The jet breaks up because of the growth of axisymmetric waves over its free surface, as shown in Figure 3.10 for the jet corresponding to realization 12 in Table 3-1. These waves are driven by surface tension and eventually pinch off the interface, producing a train of droplets which commensurate with the precursor jet.

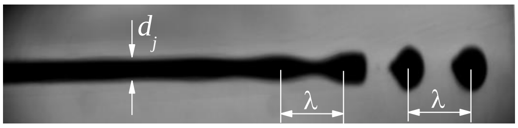

Figure 3.10 Snapshot of the breakage of a jet with diameter $d_j = 150 \pm 5$ µm and a dominant perturbation wavelength of $\lambda = 582 \pm 20$ µm.

It is usually assumed that the distance between two consecutive drops and, therefore, their diameters are essentially determined by the wavelength of the dominant perturbation arising in the linear regime. It is also generally accepted that Rayleigh's prediction (Rayleigh, 1878) provides an accurate value for that wavelength.

In Figure 3.10, varicose free-surface deformations of wavelength $\lambda = 582 \pm 20$ µm grow over a jet of diameter $d_j = 150$ µm. Two consecutive drops are separated by a distance which approximately equals λ. The ratio d_j/λ is 0.26 ± 0.02, while Rayleigh's prediction is 0.22.

The peak of the histogram in Figure 3.11 for the resulting droplets diameter roughly corresponds to Rayleigh's prediction $d_D \approx 1.89 d_j$.

The diameter of the droplets produced from such breakage was calculated by image analysis (Vega et al., 2011). A random sample was chosen to build the probability distribution of the droplet diameter. Figure 3.11 shows the high degree of monodispersity for the droplets resulting from breakage of the jet in Figure 3.10 (realization 12 from Table 3-1).

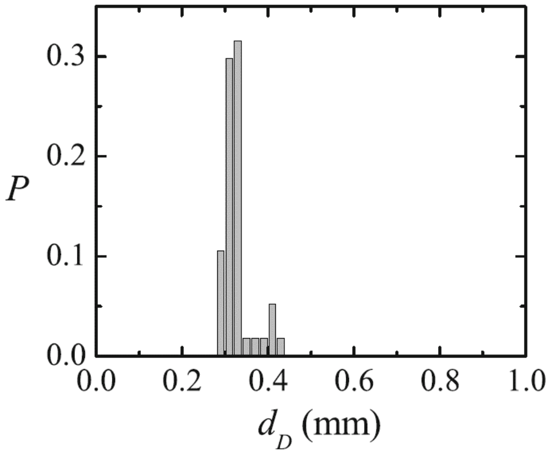

Figure 3.11 Probability distribution *P* for the droplet diameter d_D after the breakage of the jet in Figure 3.10

3.3 Paper III: Generation of micro-sized PDMS particles by a flow focusing technique for biomicrofluidics applications

3.3.1 Experimental setup and procedure

The technique is based on the needle-focusing principle proposed by Acero et al. (2013). PDMS precursor droplets are generated by means of the experimental setup depicted in Figure 3.12 to be later cured into solid particles.

The particles are fabricated from a common PDMS elastomer kit (Sylgard 186) which consists of two parts: a base of vinyl-terminated siloxane oligomers (Part A) and a curing agent of siloxane oligomers and catalyst (Part B). They are mixed in a proportion Part A:Part B of 6:4, which results in a viscosity around 827 cSt (Jiang et al., 2012). This mixture (PDMS precursor) is injected with a syringe pump through a hypodermic needle with an outer hydraulic radius r_t of a few microns in the tip (around 3 μm).

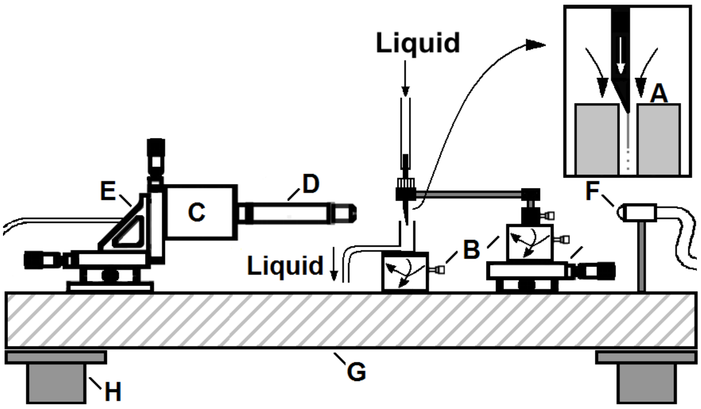

Figure 3.12 Experimental setup to generate PDMS droplets, consisting of: needle located inside a glass cylindrical capillary (A), high-precision orientation-translation systems (B), high-speed camera (C), optical lenses (D), triaxial translation stage (E), optical fiber (F), optical table (G), and pneumatic anti-vibration isolation system (H).

The needle tip is placed inside a glass capillary of 200 μm in diameter (A) by using high-precision orientation-translation systems (B). Both the needle and capillary are submerged within a bath of a mixture (9:1) of glycerol and surfactant to avoid the coalescence of the droplets downstream. This solution and PDMS precursor are immiscible. To produce the focusing effect, the outer bath is suctioned across the glass cylindrical capillary with another syringe pump at a constant flow rate.

Shadowgraph images are acquired with a high-speed CMOS camera (C), which is placed with a triaxial translation stage (E) to focus the jet. An example of the images taken throughout the droplets generation process is shown in Figure 3.13. An auxiliary CCD camera (not shown in Figure 3.12) helps to check the axisymmetric positioning of the needle with respect to the capillary.

When the precursor is injected, it forms a film/reservoir over the needle's outer surface. This film flows towards the needle tip and a liquid ligament is steadily ejected thanks to the dragging action of the coflowing stream of the glycerol bath. The co-flow provides the ligament with the necessary momentum to overcome the surface tension and form a small capillary jet (Figure 3.13 a). The jet eventually breaks up into droplets due to the growth of capillary waves, producing a micrometer emulsion (Figure 3.13 b and c). This method benefits from the remarkable stability of the fluidic structure from which the jet originates (Acero et al., 2013).

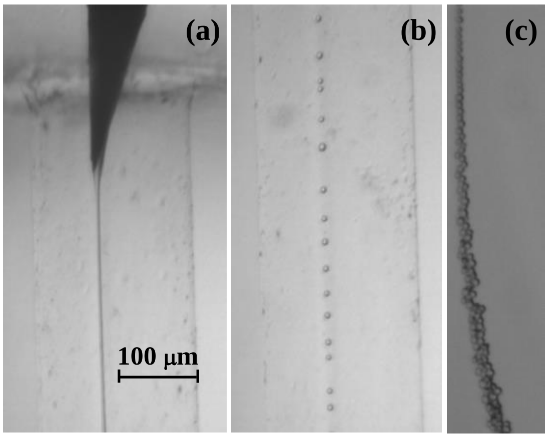

Figure 3.13 Images of the PDMS precursor droplets generation: (a) emitted jet attached to the needle tip, (b) PDMS droplets about 7 μm in diameter from the jet breakage, and (c) stream of these droplets downstream the glass capillary.

The experimental procedure can be summarized as follows:

1) An emulsion of PDMS precursor droplets is generated with the setup in Figure 3.12. A production time of 2 h is needed to get 4 ml. Images are taken along the process to characterize the jet and subsequent droplets.
2) The emulsion is deposited in a glass optical cell and heated up at 70 °C for 14 h to conduct crosslinking and cure the PDMS droplets in the solution.
3) Once it cools down to room temperature, the glass cell is scanned to characterize the cured PDMS solid particles within the bath by optical microscopy.

3.3.2 Technique characterization

In the first place, it must be noted that the the film of PDMS precursor around the needle is much larger than the jet emitted from the tip, and its volume grows slowly during the experiments. In other words, the film works as reservoir from which the system suctions the necessary flow rate to form a stable jet: the natural flow rate Q_n. The latter can be estimated with the acquired images, by multiplying the number of primary droplets produced over a certain time by their average volume.

The production of the liquid microjet entails the stretching of a tiny meniscus hanging on the needle tip (shown in Figure 3.14). That stretching takes place due to the combination of both extensional viscous stresses associated with the outer flow acceleration and the drag force due to the difference between the continuous and disperse phase velocities. In this sense, the phenomenon should be regarded as flow focusing rather than as a co-flow of two liquid streams (Gañán-Calvo et al., 2013).

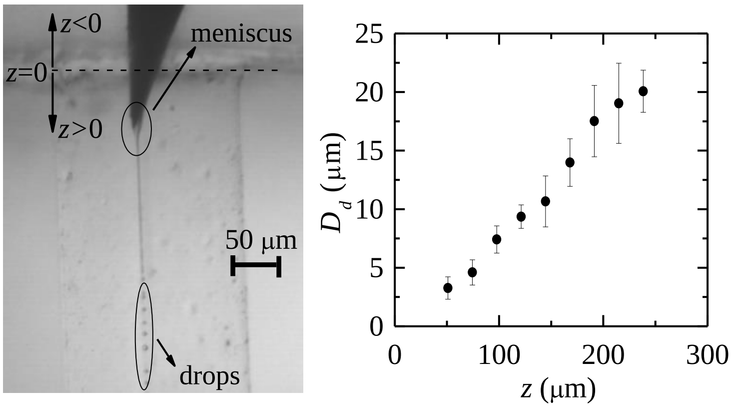

Figure 3.14 Dependence of the diameter D_d of focused PDMS droplets on the needle z position.

The technique was found to be very sensitive to the position of the needle tip within the glass capillary. If the tip is located in the capillary axis, the size of the PDMS precursor droplets can be precisely controlled by shifting the needle upstream or downstream along the axis, as shown in Figure 3.14, without varying the syringe pumps flow rates. The natural flow rate Q_n will be spontaneously adjusted by the system for each position. Such dependence of the jet diameter on the needle tip position confirms the focusing effect to be relevant.

The jet is eventually destabilized to break up into droplets (Tomotika, 1936), generating a quasi-monodisperse collection of primary drops whose diameter D_d roughly doubles the jet diameter D_j. Rayleigh's dispersion relation does not apply to this configuration due to the high viscosities of both the inner and outer streams, but Tomotika's dispersion relation for the Stokes regime (Tomotika, 1935) yields $D_d \approx 2.01 D_j$, thus supporting the experimental results.

The jet breakup gives rise to both primary and satellite droplets (Figure 3.15), whose size is characterized. Both collections exhibit a relatively high degree of monodispersity. The polydispersity can be partially explained by the observed fluctuations of the wavelength responsible for the jet pinch-off.

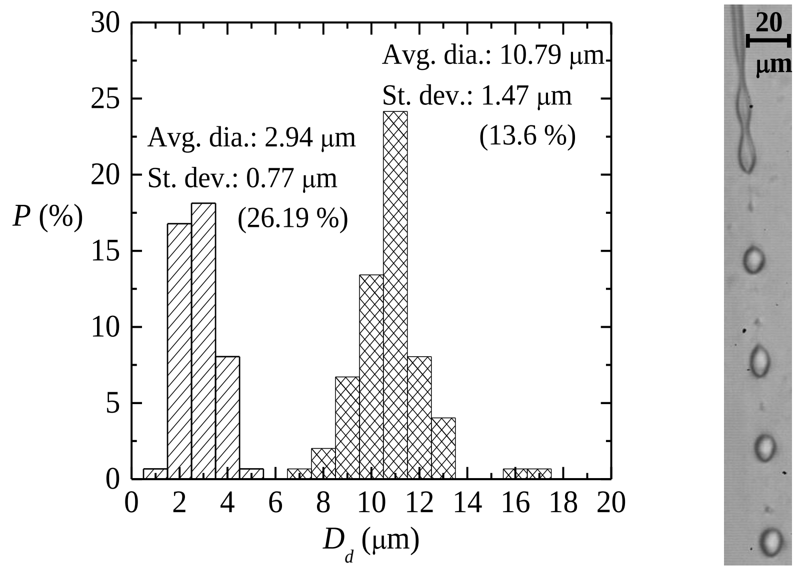

Figure 3.15 Breakup of a PDMS precursor jet produced for $z = 144$ μm, $Q_n \approx 10$ μl/h and the probability distribution for the diameter D_d of primary (meshed bars) and satellite (striped bars) drops.

The formation of satellites is determined by the rupture dynamics of the thread between two primary drops. In this viscous case, where the Stokes regime is reached and inertia neglected, they are produced by a highly nonlinear phenomenon (Tjahjadi et al., 1992) and their size depend on the viscosity ratio between the continuous and dispersed phases (Carrier et al., 2015).

Nevertheless, the use of surfactant in the outer stream could influence the formation and size of the satellite droplets. The presence of surfactants can greatly dampen and suppress surface waves, and therefore it would stabilize the rapidly stretching thread between two primary drops. Hence the thread volume grows and also does the volume of the subsequent satellite drops (Zhang and Basaran, 1995). On the other hand, the complexity of the dispersed phase (PDMS precursor) might be also participating in the jet breakup and production of satellites.

3.3.3 Particles characterization

Not only the size of the primary droplets D_d was measured, but also that of the subsequent solid particles D_p after curing. Results for several samples are shown in Figure 3.16. The shrinkage phenomenon found for other scales in PDMS manipulation is also present in the production of microparticles, since $\overline{D_p} < \overline{D_d}$ in all cases.

A curing shrinkage coefficient can be defined as:

$$C_s = \frac{\overline{D_d} - \overline{D_p}}{\overline{D_d}} \tag{3-1}$$

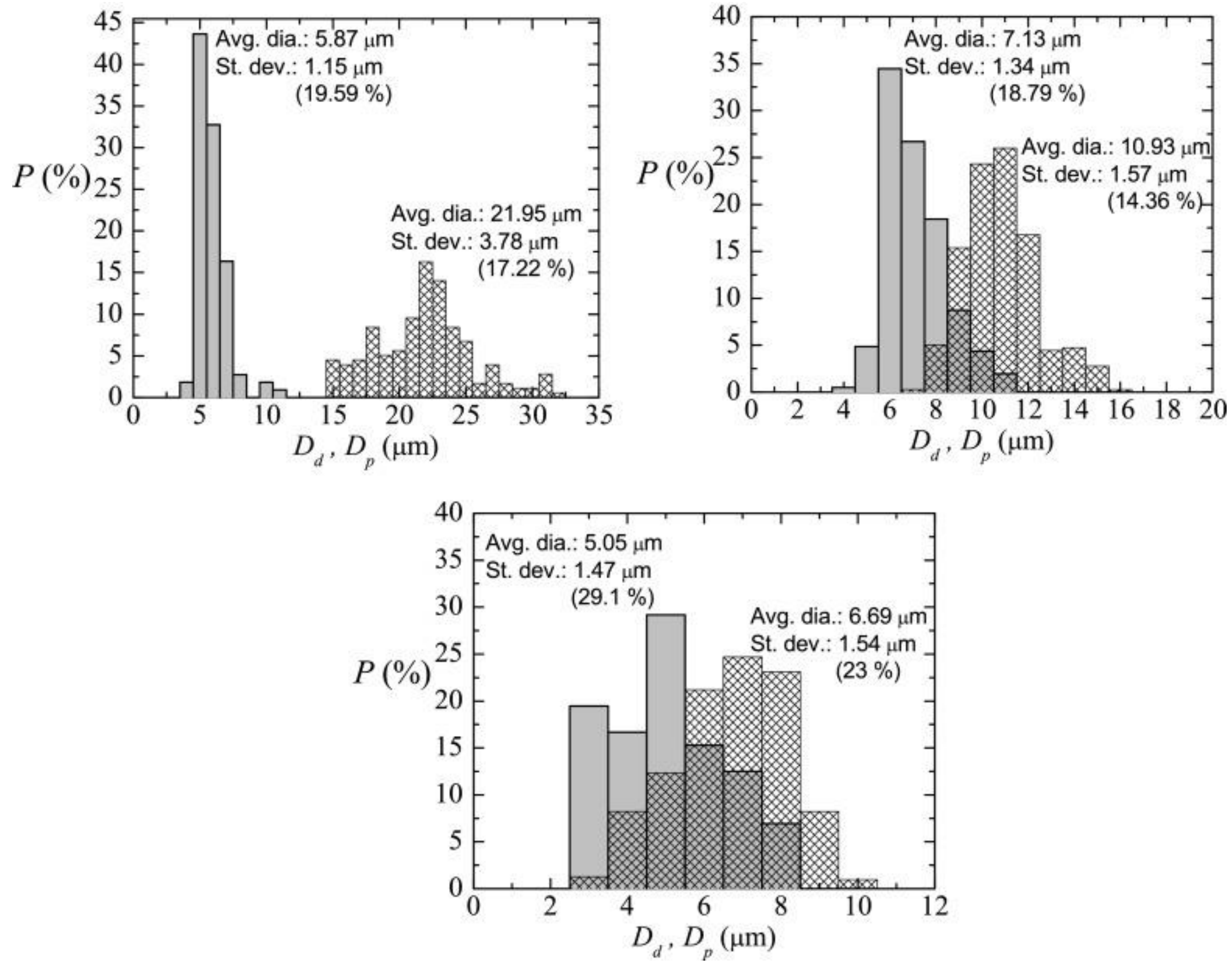

Figure 3.16 Probability distribution for the primary liquid droplet diameter D_d (meshed bars) and for the solid particle diameter after curing D_p (solid bars) of several samples: (a) $z = 240$ μm, $Q_n \approx 50$ μl/h, (b) $z = 144$ μm, $Q_n \approx 10$ μl/h, (c) $z = 90$ μm, $Q_n \approx 1$ μl/h.

For the liquid droplet diameters considered, C_s shows a linear dependency with $\overline{D_d}$, as depicted in Figure 3.17. Since shrinkage has been previously reported to be a complex phenomenon, it would need to be further explored for these microparticles.

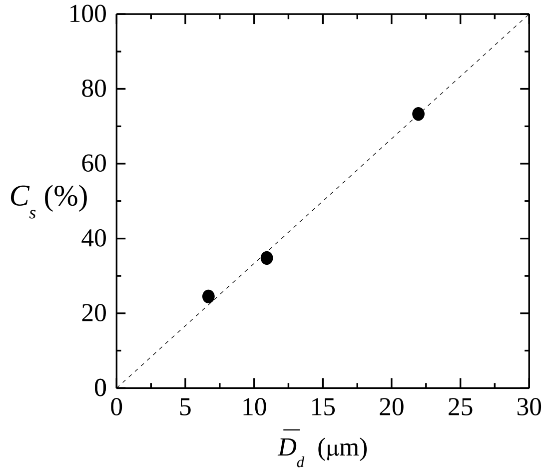

Figure 3.17 Curing shrinkage coefficient C_s of the samples in Figure 3.16 as a function of the average diameter in liquid phase $\overline{D_d}$. The dashed line indicates a possible fit to predict this shrinkage: $C_s = {}^{10}/_{3}\ \overline{D_d}$

3.4 Paper IV: Shrinkage and colour in the production of micro-sized PDMS particles for microfluidic applications

3.4.1 Shrinkage

The unusually high amount of curing agent in PDMS precursor appeared as a possible candidate to induce the important shrinkage of the samples in Paper III. Therefore, by using the technique described in section 3.3.1, some experiments were conducted to check the influence of the amount of curing agent on the shrinkage phenomenon. The same PDMS elastomer kit (Sylgard 186) was mixed in different proportions Part A:Part B, namely: 6:4 (used in Paper III), 8:2 and 10:1; whose viscosities were around 827 cSt, 1700 cSt, and 3196 cSt, respectively.

For each ratio, several samples were produced with different diameters for the liquid primary droplets. The size of these and that of the subsequent solid particles was analysed as done in Figure 3.16. In all cases, the monodispersity of the collections is relatively high, with similar values of the coefficient of variance. Further details can be found in Paper IV. The technique is hence proved to work with a wide range of viscosities.

The curing shrinkage coefficient C_s was calculated for such samples with Eq. (3-1). The results are represented in Figure 3.18, with all ratios showing the same linear dependency on liquid droplets diameter up to 24 µm. Therefore, the shrinkage found for these microparticles does not depend on the amount of curing agent in the PDMS precursor. Rather surface effects, while the particles are curing, would motivate this pronounced shrinkage due to the relatively large surface-to-volume ratio for these droplet sizes.

The range of primary liquid droplet diameter was also here extended with respect to that produced in Paper III. This allows exploring larger sizes where surface effects can be neglected. This is supported by the fact that in such cases, when liquid droplets are above 24 µm in diameter, C_s becomes constant (Figure 3.18).

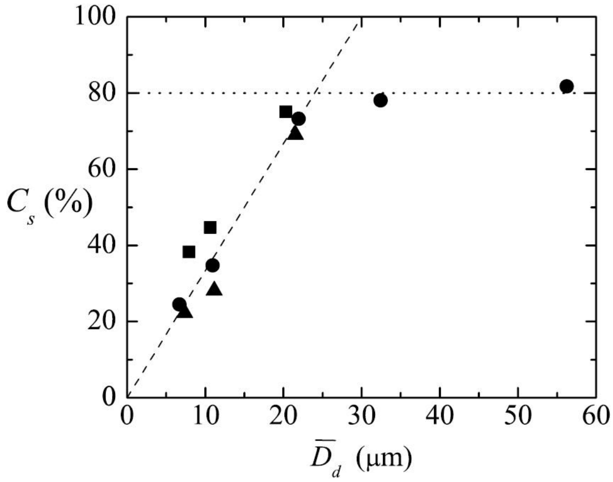

Figure 3.18 Curing shrinkage coefficient C_s for different PDMS ratios - 6:4 (circles), 8:2 (squares) and 10:1 (triangles) - as a function of the average diameter in liquid phase $\overline{D_d}$. The dashed line indicates a possible fit to predict this shrinkage: $C_s = {}^{10}/_{3}\,\overline{D_d}$ for diameters below 24 µm and a constant value for larger diameters.

3.4.2 Colour

To the best of the authors' knowledge, there is no specific colourant that is soluble in PDMS, so the addition of colour would result from the use of pigments. Due to the insolubility, the expected outcome when mixing PDMS precursor with the pigment is a fine dispersion/emulsion. Some preliminary colouring tests were performed with different commercial dyes/pigments. Each of them was carefully mixed with part A, and part B was later added to get the dyed PDMS precursor.

When the cured samples were observed with a microscope, the majority of them presented a heterogeneous microstructure, even if they appeared to be uniformly coloured at simple sight. For the gel-like dyes, large microspheres of dye were trapped within the solid bath. In the case of some pigments, solid aggregations of particles were found. Only one sample showed a suitable and homogeneous microstructure both in the preliminary tests and during the droplet generation phase: a red pigment paste for silicon.

On the other hand, the technique from section 3.3.1 was used to generate droplets with a PDMS precursor commercialized as 'black' PDMS (Sylgard 170). The images acquired in the course of experiments reveal that it is also a dispersion, made of usual PDMS with a special pigment.

Both the red-dyed and the black PDMS showed a similar monodispersity to previous samples of transparent PDMS, when the collections of liquid precursor droplets and the subsequent solid particles were analysed (further details in Paper IV). Therefore, the technique is valid to generate microparticles that encapsulate other nanoentities within.

The curing shrinkage coefficient C_s has been calculated for the coloured microparticles, following the same tendency than the transparent particles (Figure 3.19). Although the shrinkage is not affected by the addition of dye, other effects on the resulting particles need to be explored.

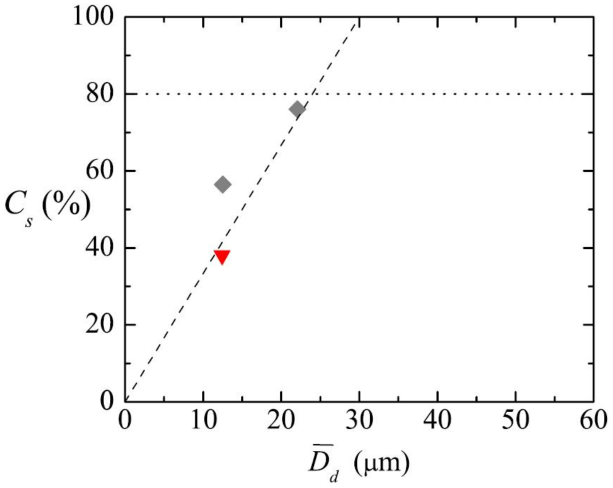

Figure 3.19 Curing shrinkage coefficient C_s for coloured PDMS – red-pigmented (red down triangles) and commercial black PDMS (grey diamonds) – as a function of the average diameter in liquid phase $\overline{D_d}$. The dashed lines show the same fit as Figure 3.18.

3.5 Paper V: Flexible PDMS microparticles to mimic RBCs in blood particulate analogue fluids

3.5.1 Microparticles and working fluids

PDMS microparticles for this study have been produced following the technique in section 3.3.1, always with approximately the size of human RBCs (~ 8 μm). PDMS precursor was obtained from a transparent elastomer kit (Sylgard 186) whose Part A and Part B were mixed in different ratios: 10:1, 8:2 and 6:4 (those used in section 3.4.1). On the other hand, coloured samples were also obtained from the precursors studied in section 3.4.2: a black PDMS (Sylgard 170, standard mixing ratio 1:1) and a transparent PDMS at ratio 10:1 dyed with 20 wt% of red pigment.

The resulting dispersions were diluted in water to be passed through a glass microfiber filter of 1.2 μm in pore size. In this way, PDMS solid microparticles got separated from the glycerol and surfactant bulk and get trapped in the filter. This is later cleaned with a stream of 1-propanol to drag the microparticles to a petri dish. After letting the propanol evaporate, the dried PDMS microparticles can be re-suspended in various media depending on the application; in this case, Dextran 40.

The suspensions of PDMS microparticles prepared with such method are summarized in Table 3-2, together with blood suspensions they will be compared against. The latter contain human RBCs, both healthy and pathological (from a patient diagnosed with Diabetes Mellitus type II), prepared as indicated in (Pinho et al., 2016; Pinto et al., 2015).

Table 3-2 Summary of working fluids prepared by suspending either PDMS microparticles or human RBCs. Hematocrit (Hct) corresponds to the concentration (v/v %) of RBCs in the sample.

	Composition of the fluid	**Acronym**
Suspending medium	Dextran 40 (solution in water at 10 wt%)	Dx 40
Suspensions of PDMS microparticles	Dx 40 + Transparent PDMS microparticles at 10:1	10:1
	Dx 40 + Transparent PDMS microparticles at 8:2	8:2
	Dx 40 + Transparent PDMS microparticles at 6:4	6:4
	Dx 40 + Black PDMS microparticles at 1:1	Black PDMS
	Dx 40 + Red-dyed PDMS microparticles at 10:1 (20 wt% of red pigment)	Red PDMS
	Dx 40 + Transparent PDMS microparticles at 10:1, 8:2, 6:4 (concentration of 8 %vol)	Final working fluid
Blood fluids	Dx 40 + Healthy RBCs (Hct of 8 %)	Healthy RBCs
	Dx 40 + Pathological RBCs (Hct of 8 %)	Pathological RBCs

3.5.2 Deformability

The ability of RBCs to deform is one of the most important properties to be mimicked by the microparticles. In order to evaluate it, the suspensions were made to flow through a microchannel with a hyperbolic-shaped contraction. This shape produces a controlled quasi-homogeneous extensional flow field through the contraction (constant strain rate), thus elongating the flexible microparticles/cells. The microentities were visualized with a high-speed video microscopy system (Rodrigues et al., 2015) while flowing at different flow rates.

The microchannel used, with a constant depth of about 15 µm, is shown in Figure 3.20. The microentities are evaluated individually when crossing the three marked regions (R1, R2 and R3) by image analysis (Yaginuma et al., 2013).

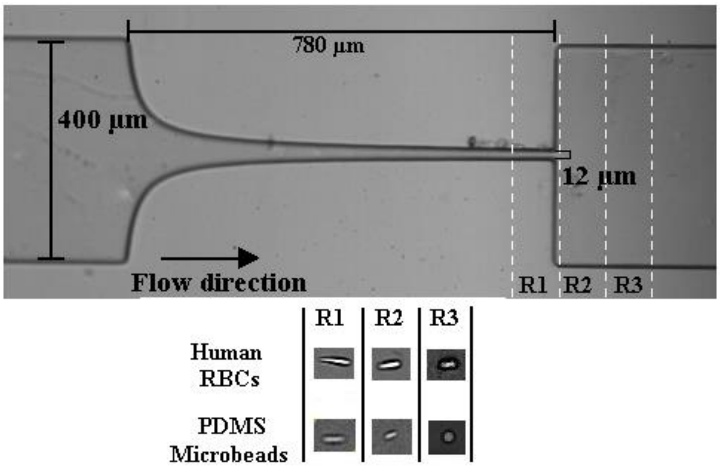

Figure 3.20 Hyperbolic microchannels with the three regions R1, R2 and R3 where deformability is evaluated. Typical deformations for each region are illustrated at the bottom.

The deformability is quantified through the deformation index (DI) defined in Figure 3.21, where X and Y are respectively the major and minor axis of the cells or microparticles (Bento et al., 2018b). DI values in R1, the narrowest region of the hyperbolic contraction, are expected to be the highest. Additional measurements are taken in R2 and R3, where there is an abrupt expansion and the microentities tend to recover their original shape.

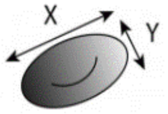

$$\mathrm{DI} = \frac{(X-Y)}{(X+Y)}$$

Figure 3.21 Schematic representation of a deformed particle and definition of the deformation index (DI).

The deformation index of all the working fluids is evaluated and compared in Figure 3.22 at different flow rates. 100 microparticles/cells were individually measured for each sample.

In the first place, all PDMS microparticles present some degree of deformability at region R1, which demonstrates PDMS to be a good option to develop flexible microparticles. It is also clear that their deformation increases with the flow rate, as it happens with RBCs, presenting, both PDMS microparticles and RBCs, the highest DI values for the flow rate of 10 µl/min.

On the other hand, DI at the recuperation regions R2 and R3 is much lower for the PDMS microparticles than for RBCs. All PDMS samples present a similar and fast retrieval of their original spherical shape, resulting in a DI value close to zero; whereas RBCs, due to their unique biomechanical properties, show a higher recovery time than PDMS microparticles (Pinho et al., 2017; She et al., 2013; Tomaiuolo, 2014).

When comparing the behaviour of the different PDMS samples, there is not a significant variation among the transparent mixtures (ratios of 10:1, 8:2 and 6:4). Their DI in R1 is a midway value between healthy and pathological RBCs. Transparent PDMS microparticles therefore arise as good candidates to mimic RBCs with a certain degree of disease, for example an intermediate status of Diabetes Mellitus type II.

On the contrary, the pigmented samples (red-dyed PDMS and commercial black PDMS) happen to be much less deformable than the transparent ones. The reduction in the Young's Modulus due to the addition of dye had already been observed in PDMS micropillars (Khare et al., 2015). Clearly, DI measurements for the pigmented samples are far from the human RBCs values, either the healthy or the pathological ones, so they do not seem adequate to represent RBCs in the development of particulate analogue fluids.

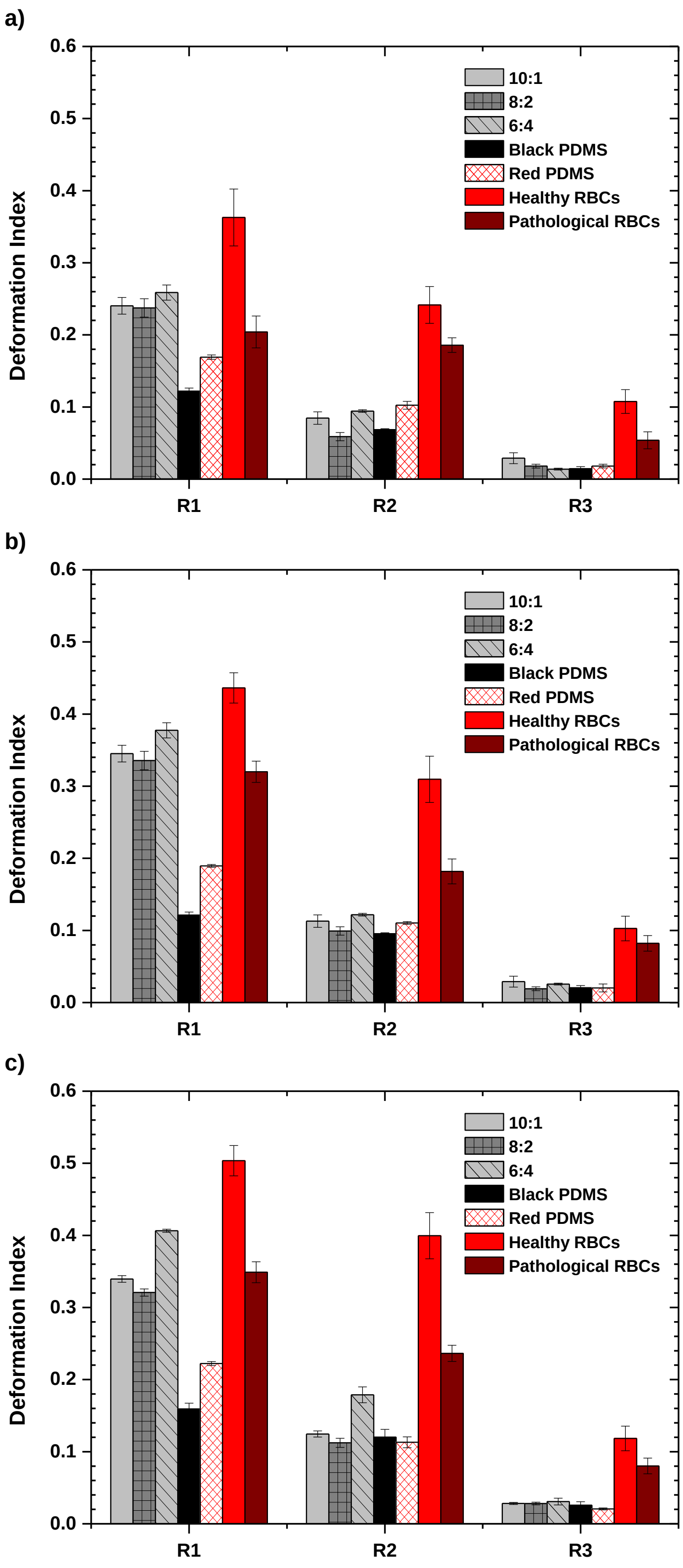

Figure 3.22 Deformation index at the regions in Figure 3.20 for all the produced PDMS microparticles and RBCs at the flow rates of: a) 5 µl/min; b) 8 µl/min and c) 10 µl/min. The error bars represent the confidence interval at a level of 95% for n = 100.

3.5.3 Rheological characterization

In order to compare the rheological behaviour of suspensions of PDMS microparticles and RBCs, steady shear flow was characterized at 22 ºC with a rheometer,by using a cone-plate geometry of 55 mm in diameter and a gap size of 30 µm. For each fluid, the measurements were performed three times with a fresh new sample of each, thus corroborating the reproducibility.

The low throughput of the production method motivated the preparation of a final working fluid (Table 3-2), with an increased concentration of particles (8 %vol). It contains the most deformable microparticles: transparent PDMS microparticles of 10:1, 8:2 and 6:4 ratios, all merged. This will be compared against suspensions of human RBCs, both the healthy and the pathological, at the same concentration.

The steady shear viscosity curves in Figure 3.23 show the constant viscosity of the suspending medium (Dx 40) over all the shear rates, whereas the particulate suspensions suffer a smooth shear thinning at small shear rates and constant viscosity (newtonian behaviour) at high shear rates. This Newtonian plateau viscosity gets increased over that of the suspending medium, due to the addition of either microparticles or RBCs.

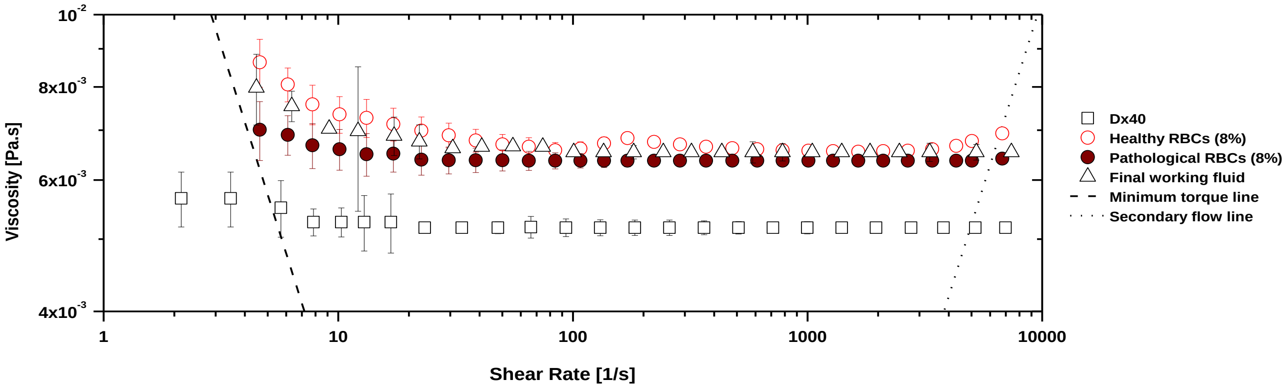

Figure 3.23 Steady shear viscosity curves for the suspending medium (Dx 40) and suspensions of different particles at a concentration of 8 %vol. The error bars represent the confidence interval at a level of 95%.

A closer look into the low shear-rate range reveals that the suspension of pathological RBCs has a smaller shear-thinning degree than the healthy RBCs. The final working fluid shows an intermediate behaviour between both of them. Therefore, transparent PDMS microparticles show a good agreement with the rheological properties of *in vitro* RBCs samples, with a midway shear-thinning degree that could mimic RBCs with a certain status of pathology.

3.5.4 Cell-free layer

The microchannel in Figure 3.20 also allows visualizing the cell-free layer that forms close to the walls, since hyperbolic contractions have a strong effect on the thickness of the downstream CFL (Rodrigues et al., 2016b). Processed images (Pinho et al., 2013, 2017) in Figure 3.24 show that a suspension of PDMS microparticles form such a layer in a similar way than suspensions of RBCs (either healthy or pathological). Additionally, the thickness of this microparticle-free layer grows with the increase of the flow rate, in the same trend as the suspensions of RBCs (Figure 3.25).

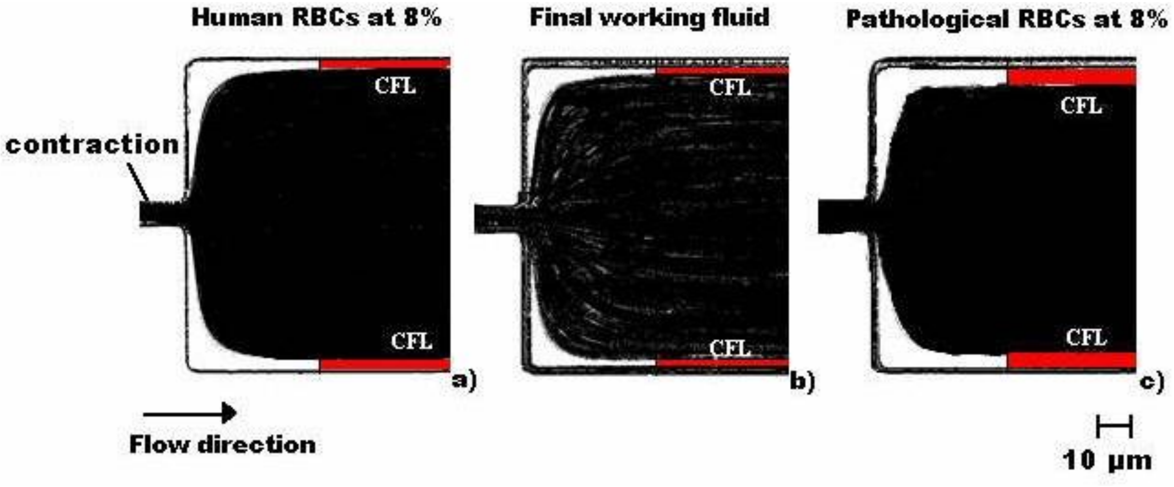

Figure 3.24 CFL marked in red in the microchannel at the flow rate of 8 µl/min for: a) suspension of healthy RBCs; b) final working fluid; c) suspension of pathological RBCs.

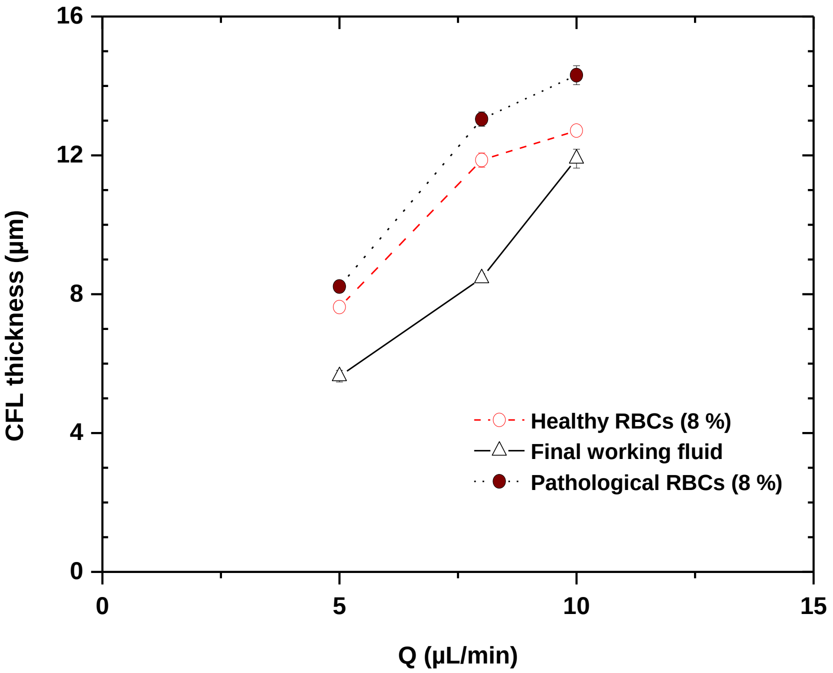

Figure 3.25 CFL thickness dependence on the flow rate for the different suspensions. The error bars represent the confidence interval at a level of 95%.

3.6 Paper VI: Borosilicate nozzles manufactured by reproducible fire shaping

3.6.1 Experimental setup

Figure 3.26 shows the apparatus to manufacture nozzles with a vertical flame, starting from cut-end borosilicate capillaries of 3.3 ± 0.1 mm outer diameter, 2.772 ± 0.1 mm inner diameter and 100.0 ± 0.5 mm length.

The flame was produced by a commercial Bunsen burner (A). The capillary (D) was held and rotated by a precision drill chuck (E) mounted on the shaft of a geared DC motor (F). The capillary axis, i.e., the motor shaft, could be oriented depending on the flame shaping approach: in Figure 3.26, the axis is vertical for the TVF configuration, whereas for SVF experiments it would be rotated to a horizontal axis.

The positioning of the capillary tip in the flame was done with high-precision translation stages, by moving either the motor (H) or the burner (G). The heating time was controlled by a micro-controller board (Arduino) that moved a ceramic plate (J) through a micro servo (I). The ceramic plate was either moved away during the heating time or placed between the flame and the capillary to separate both and stop the heating.

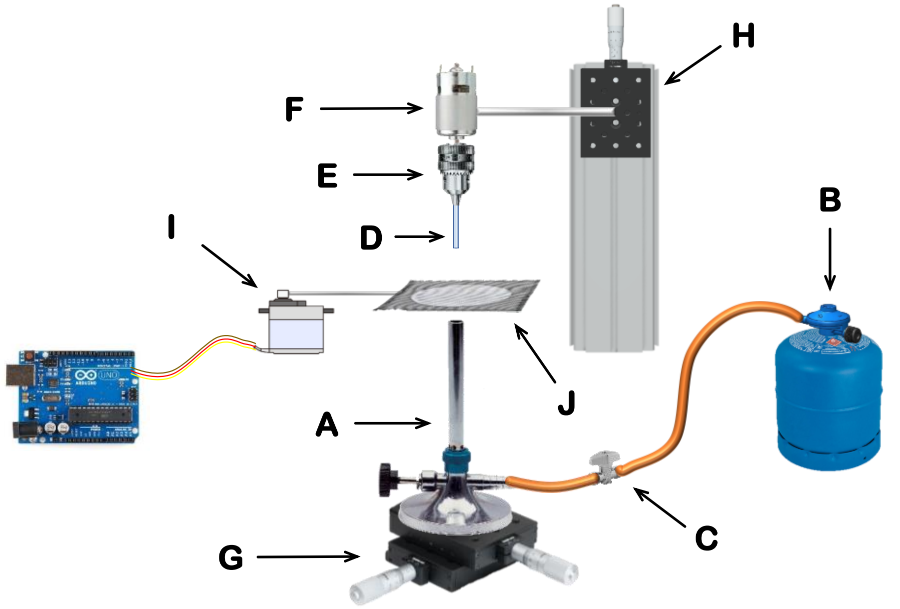

Figure 3.26 Experimental setup for flame shaping (TVF approach). (A) Bunsen burner, (B) butane bottle and regulator, (C) gas valve in the hose, (D) capillary, (E) drill chuck, (F) DC motor for capillary rotation, (G) two-axis translation stage for horizontal positioning, (H) one-axis translation stage for vertical positioning, (I) servo and (J) ceramic plate for heating time control.

3.6.2 Experimental procedure

The heating position of the capillary is defined in a coordinate system (r, z) associated to the burner tube (Figure 1.6), with its origin at the burner exit center. The radial r and axial z coordinate values correspond to the radial and axial distances of the capillary tip center to this reference point. Therefore, previous to manufacturing, a reference search is done to find the burner exit center position. During the experiments, the burner and gas bottle valves are kept fully open to maintain a constant flow rate, and only the gas valve (C) is operated to open and close the flow.

The manufacturing procedure for each nozzle consisted of the following steps:

1) The desired heating and cooling times are transferred to the Arduino board
2) The heating position is adjusted by using the translation stages
3) The capillary is mounted in the drill chuck and the DC motor starts rotating
4) The servo places the ceramic plate between the burner tube exit and the capillary, and the flame is lighted

5) The plate is moved away and the heating starts
6) When the desired heating time has passed, the Arduino board moves the ceramic plate back to the separation position, where the flame does not reach the capillary, and the heating stops
7) The flame is extinguished, and the capillary is kept rotating for a cooling time
8) Finally, the DC motor is stopped, and the capillary is released from the drill chuck

3.6.3 Optical characterization of the nozzles

The geometry of each resulting nozzle was studied by an optical characterization method similar to that described by Montanero et al. (2010). First, the capillary end opposite to the nozzle was connected to a compressed air source. Then, the nozzle end was inserted from below in a cubic cell full of glycerin, that has nearly the same refractive index as the borosilicate, to avoid optical distortion in the images. Backlight images were taken with a CCD camera. The air inside the nozzle shows up black whereas both the borosilicate and the glycerin show up grey (Figure 3.27a).

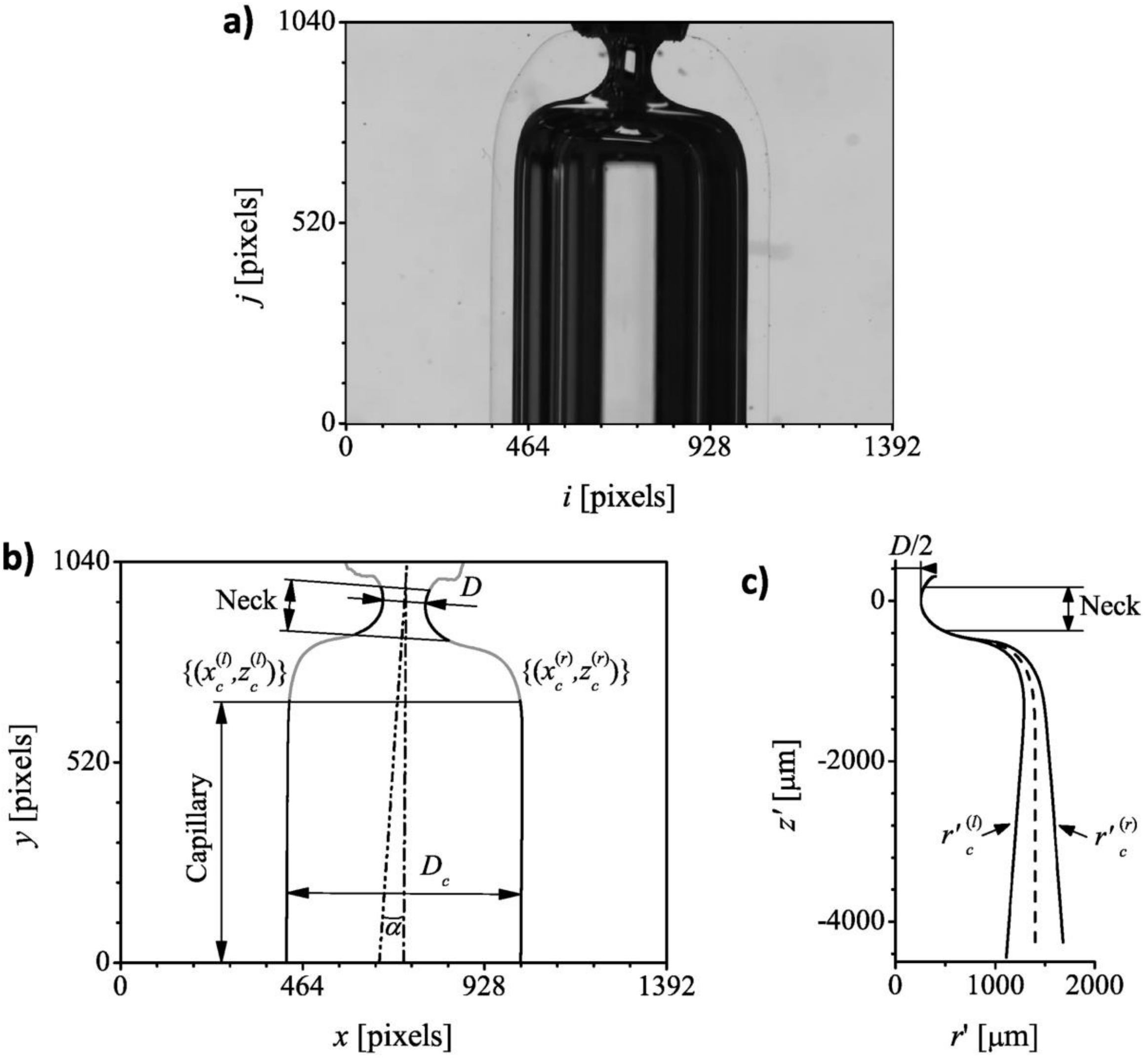

Figure 3.27 Optical characterization of a nozzle fabricated by SVF with a neck diameter D = 509 μm. (a) Backlight image. (b) Contours obtained by the edge detection routine, and calculated misalignment angle α between the capillary (dot-dash line) and the neck (two dot-dash line) symmetry axes. (c) Left and right contours (solid lines) and mean profile (dashed line) in the neck coordinate system.

Details of the two-stage edge detection routine can be found in Paper VI. The contours in Figure 3.27 b show the transition from the capillary inner diameter D_c to the neck diameter D in the convergent zone, and then the diameter increase in the divergent one. For the symmetry analysis, we consider two different regions: the lower capillary and the nozzle neck. A symmetry axis is obtained for each region and then a misalignment angle α between them is calculated.

Once the left and right profiles are detected, the mean profile (Figure 3.27 c) is used to calculate the neck diameter D. The mean deviation between the left and right profiles can be used to evaluate the symmetry in both the neck region and the whole capillary, through the values of e_n and e_g respectively. Since the neck symmetry axis is used for the new coordinate system, the left-right deviation at the neck region is always better than at the whole nozzle shape, that is, $e_n < e_g$ always.

To completely characterize the shape of each nozzle, we took three different views of the nozzle by rotating it about the capillary axis (Figure 3.28). Each image was processed to get the left, right and mean contour for each view in the neck coordinate system (Figure 3.29). Then, all the parameters described above are calculated for each view (Table 3-3). Global results for the nozzle are the mean values of the three images for the nozzle diameter D and deviations e_n and e_g with the standard deviation as an error estimation. However, the global nozzle misalignment angle α is calculated as the maximum of the values for the three views.

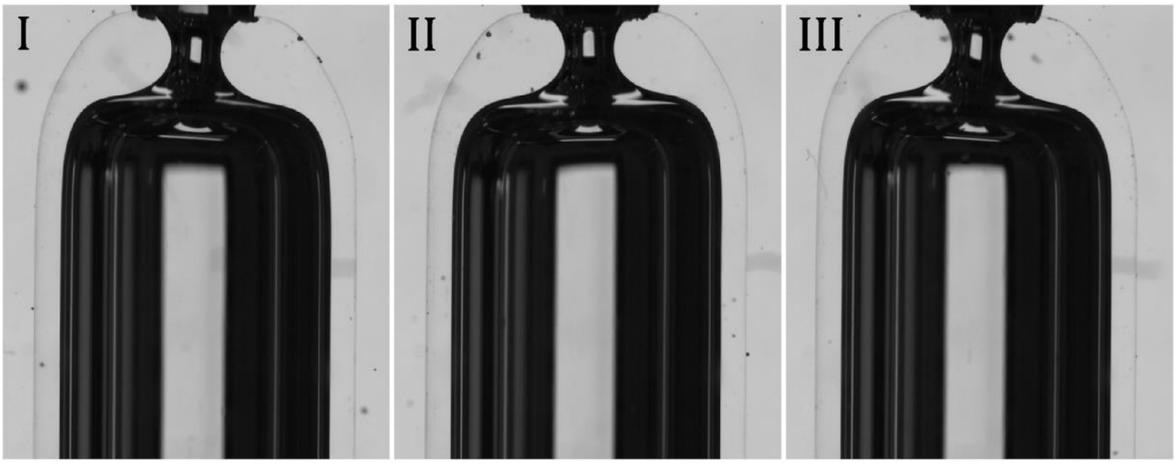

Figure 3.28 Three views of a nozzle manufactured on the side of a vertical flame (SVF)

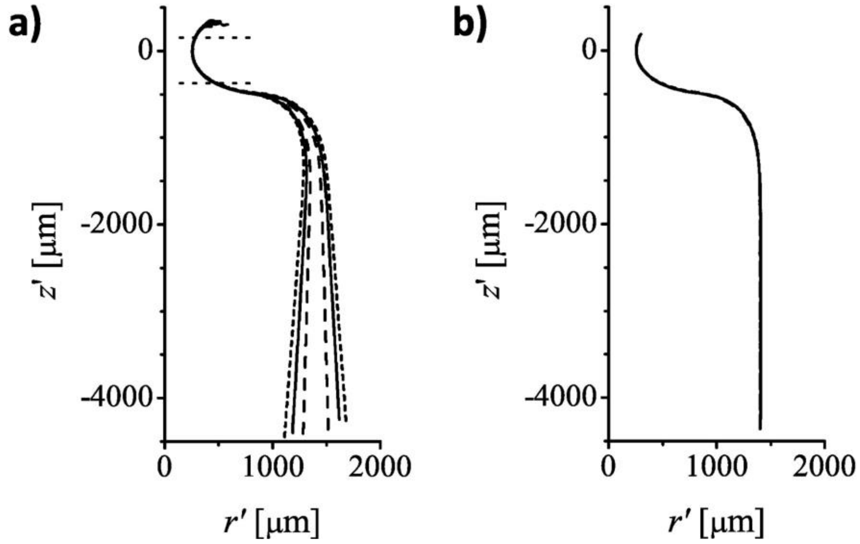

Figure 3.29 Detected profiles for Figure 3.28. (a) Six detected (left and right) profiles for view I (solid), view II (long-dashed), and view III (short-dashed). Horizontal dotted lines mark the neck region. (b) Three mean profiles overlapping.

The lack of symmetry for the nozzle in Figure 3.28 is clear, though more significant for view III. This misalignment produces a profile deviation that becomes larger as we move away from the neck (e_g). Nevertheless, the three mean profiles overlap even for the lower capillary region (Figure 3.29 b). This happens for every nozzle characterized, so a single mean profile can be used to characterize each nozzle.

Table 3-3 Characterization values for the three views in Figure 3.28 and global results for the nozzle.

View	D (µm)	α (°)	e_n (µm)	e_g (µm)
I	508.9	2.7	1.2	191.3
II	509.3	1.4	1.4	110.4
III	509.2	3.5	1.6	253.1
Nozzle	509.1 ± 0.2	3.5	1.4 ± 0.2	184.9 ± 71.6

3.6.4 Flame temperature analysis

Although the flame shaping idea is simple, the phenomena involved in the process are not. The temperature in the flame is not uniform, with the maximum occuring slightly above the inner blue cone in the flame axis. The temperature dependence of the magnitudes involved in the glass flow, surface tension and viscosity, is very high. Therefore, the capillary orientation and position during fire shaping seem to be key process parameters, as they determine not only the maximum heating temperature, usually at the capillary tip, but also the temperature profile in the heated portion.

The material involved in the flow, and so the nozzle length, depends on both the temperature profile in the heated portion and the heating time. The time to achieve a certain diameter reduction depends on both the temperature profile, which changes as the flow happens, and the material involved in the flow. The process is clearly complex, and producing a nozzle with a controlled size or shape is not straightforward.

Given the importance of the temperature in the shaping process, we performed a preliminary study in the regions where the capillary may be heated in our experiments. Temperature was measured by replacing the capillary and motor set in Figure 3.26 with a Type K thermocouple connected to a data-logger, orientating it both horizontally and vertically when approaching the flame.

Further details of this study can be found in Paper VI. Note that the temperature measurements do not match either the flame or the capillary temperature in the process. The presence of the thermocouple inside the flame disturbs the flow differently than the capillary does, and the geometry and physical properties of the elements involved are different as well. However, the measured values yield helpful information to analyse the shape of the nozzles depending on position or orientation.

3.6.5 Fire shaping a horizontal capillary on the side of the flame (SVF)

In order to manufacture reproducible short nozzles, a short heated length and low temperature fluctuations seem to be desirable. So, to evaluate this approach, and taking into account the results from section 3.6.4, experiments were carried out at the lowest possible level in our experimental setup (Figure 3.26): leaving the necessary space between the capillary and the burner exit for the ceramic plate. A series of ten nozzles was manufactured at that level ($z = 17$ mm) with the capillary tip just in contact with the flame ($r = 8$ mm). The heating time was adjusted ($t = 300$ s) to produce nozzles with a neck diameter close to 500 µm.

Table 3-4 Mean values of characterization for a series of 10 nozzles manufactured by SVF. Heating parameters: $r = 8$ mm, $z = 17$ mm and $t = 300$ s.

D (µm)	α (°)	e_n (µm)	e_g (µm)
470 ± 64	4.0 ± 1.2	2.9 ± 2.7	195.7 ± 56.4

One of those nozzles was shown in Figure 3.28, whose parameters (Table 3-3) are like the average for the whole series. Table 3-4 shows the mean characterization results for that series. The neck diameter dispersion is moderate, and the neck symmetry (e_n) is very good. However, there is a significant misalignment between the axis of the neck region and the capillary axis, probably due to the effect of gravity, so the symmetry for the whole nozzle (e_g) is poor.

As pointed out in section 1.5, it is very important to obtain a very low misalignment angle when manufacturing nozzles. In most experimental setups, the nozzles are aligned with other components through the capillary outer surface (Utada et al., 2005) or the inner one (DePonte et al., 2008). If the nozzle neck is tilted with respect to the capillary axis, the flow emitted by the nozzle will not be properly aligned with other elements in the experimental setup, and it may affect the performance of the experiments. Therefore, fire shaping a horizontal capillary on the side of a vertical flame (SVF) does not seem to be an adequate approach for producing satisfactory axisymmetric nozzles.

3.6.6 Fire shaping a vertical capillary at the top of the flame (TVF)

For this fire shaping approach, the capillary axis was aligned with that of the burner tube, as the temperature around this axis is more uniform (section 3.6.4). To choose an adequate heating position, it must be taken into account that the motor is located above the flame in our experimental setup (Figure 3.26), so it gets heated by the flame and the combustion gases. It may be damaged by overheating in two cases: (i) when it is too close to the flame, where the temperature is too high; or (ii) when it is too far over the flame, where, though the temperatures are lower, the heating time has to be long to produce the desired diameter reduction.

Considering the above, an adequate working region is found by positioning the capillary end at the limit of the visible flame and below (85 mm < z < 95 mm). In that region, the measured temperature is about 950 °C, and a capillary portion over 25 mm in length is heated above the softening point. The resulting nozzles are therefore expected to be long, and their geometry, as seen in Figure 3.30 and Table 3-5, is radically different to that of nozzles manufactured by the SVF approach (Figure 3.28 and Table 3-3), showing deformation for the whole field of view in the images.

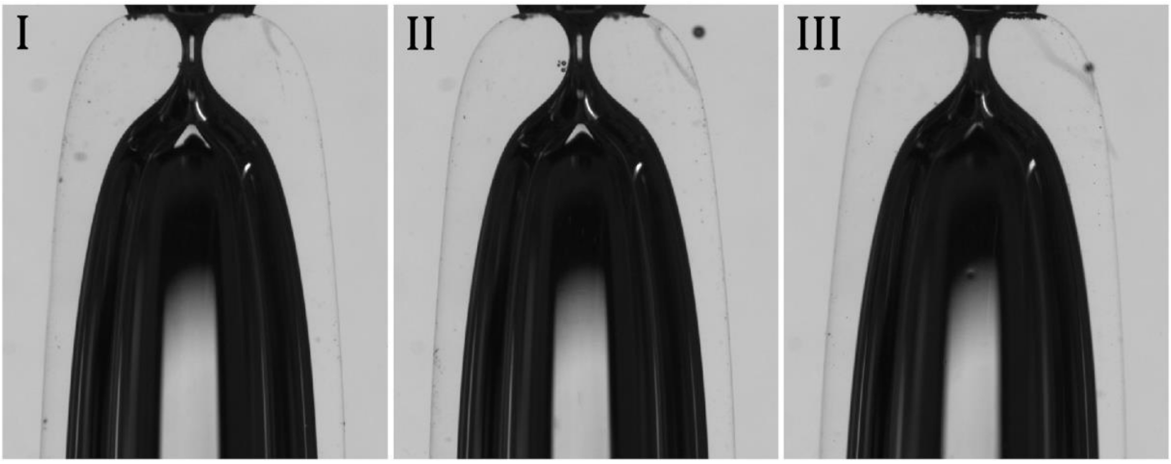

Figure 3.30 Three views of a nozzle manufactured at the top of a vertical flame (TVF). Heating parameters: $r = 0$ mm, $z = 95$ mm, $t = 30$ s.

Table 3-5 Characterization values for the three views in Figure 3.30 and global results for the nozzle.

View	***D*** **(µm)**	***α*** **(°)**	e_n **(µm)**	e_g **(µm)**
I	208.1	0.5	0.7	17.1
II	212.1	0.8	0.8	30.0
III	207.5	0.6	1.1	32.1
Nozzle	209.2 ± 2.5	0.8	0.9 ± 0.2	26.4 ± 8.1

To analyze the nozzle reproducibility of the TVF approach, we manufactured five series of ten nozzles for the same heating conditions (position and time), as shown in Table 3-6.

Table 3-6 Mean characterization values for five series of ten nozzles produced by fire shaping vertical capillaries at the top of the flame (TVF).

Series	***z* (mm)**	***t* (s)**	***D* (µm)**	***α* (°)**	**e_n (µm)**	**e_g (µm)**
1	95	20	1432 ± 499	0.4 ± 0.2	4.0 ± 2.1	19.8 ± 10.9
2	95	30	717 ± 419	0.6 ± 0.3	4.4 ± 2.0	30.8 ± 14.2
3	90	20	710 ± 306	0.7 ± 0.4	3.0 ± 1.5	33.9 ± 17.6
4	90	30	238 ± 166	0.7 ± 0.4	2.2 ± 0.7	29.5 ± 16.7
5	85	30	461 ± 493	0.6 ± 0.3	3.0 ± 1.8	26.7 ± 16.3

There are large differences in the neck diameter of the nozzles of a series, produced in the same heating conditions (the standard deviation is of the order of the mean value). Also, for different heating conditions, the nozzle neck diameter ranges overlap. Therefore, for the TVF fire shaping approach, the heating time does not seem to be an appropriate parameter to control the resulting nozzle diameter for a particular position.

However, Table 3-6 shows some positive results regarding the nozzle shape for the 5 series: the neck symmetry (e_n) is very high and the misalignment (α) between the nozzle neck and the capillary axes is always below 1°, much lower than SVF nozzles (Table 3-4). Consequently, the global symmetry for TVF nozzles is very good, with relatively low values for the mean profile deviation (e_g).

3.6.6.1 Capillary shortening

Additionally to the optical characterization parameters, the capillary shortening ΔL was calculated by measuring the length of the capillary before and after the nozzle fabrication with a caliper.

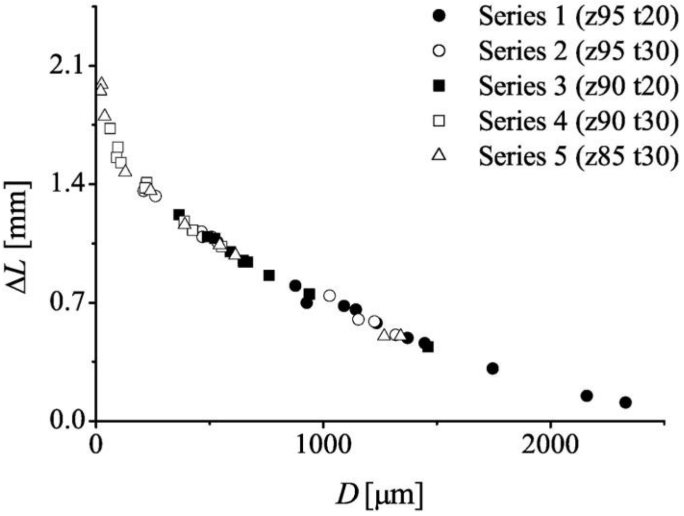

Figure 3.31 Capillary shortening versus neck diameter for the five series of TVF nozzles.

The analysis of the capillary shortening versus the neck diameter (Figure 3.31) produces a very interesting result. As expected, the capillary shortening is greater for smaller nozzle neck diameters. However, the most surprising fact is that all results fall on the same curve, even for different manufacturing conditions. Therefore, within the range of heating positions studied, the capillary shortening can be used to estimate the neck diameter. This value, instead of the heating time, arises as a possible control parameter to produce nozzles of a particular neck diameter by TVF approach.

3.6.6.2 Shape reproducibility

When comparing nozzles of similar diameters from different series (different manufacturing parameters), not only the shortening but also the shape happens to coincide. Figure 3.32 shows the shape comparison of four pairs of nozzles with similar diameters that were produced in different conditions, which are specified in Table 3-7.

The excellent overlapping in all cases, for a wide range of diameters, indicates that the shape of TVF nozzles is not affected by the heating conditions, being only dependent on the neck diameter produced.

In other words, the reproducibility of the nozzle shape is very good within the range studied, and nozzles with the same neck diameter have the same shape.

Table 3-7 Heating conditions and diameter of the TVF nozzles compared in Figure 3.32

	Nozzle 1			**Nozzle 2**		
Set	***D*** **(µm)**	***z*** **(mm)**	***t*** **(s)**	***D*** **(µm)**	***z*** **(mm)**	***t*** **(s)**
1	216 ± 5	90	30	209 ± 3	95	30
2	389 ± 6	90	30	391 ± 3	85	30
3	534 ± 2	95	30	546 ± 13	85	30
4	1234 ± 9	95	20	1225 ± 8	95	30

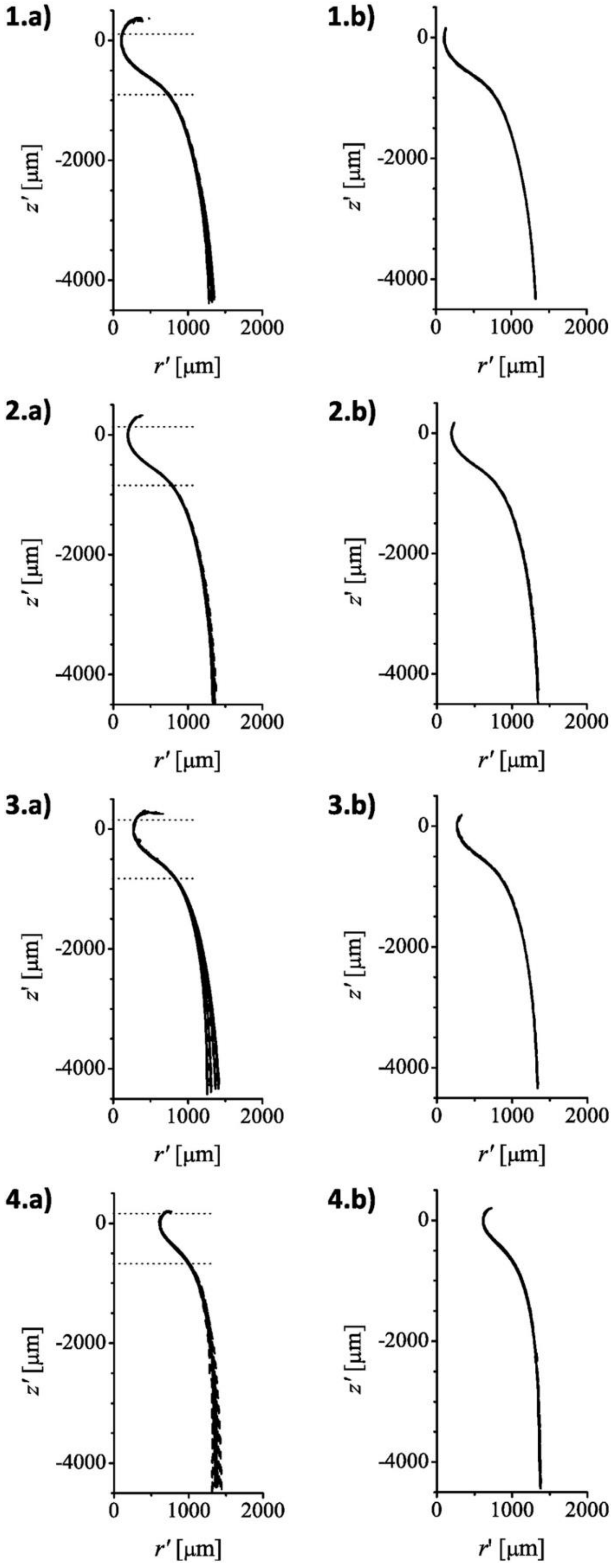

Figure 3.32 Shape comparison between sets of two nozzles of similar diameters manufactured in different conditions (given in Table 3-7). Continuous lines correspond to the first nozzle in the set, and the dashed lines to the second. Horizontal dotted lines limit the neck region. (a) Twelve detected (left and right) profiles for the three views of each nozzle. (b) Six corresponding mean profiles for each set.

3.7 Paper VII: A new fire shaping approach to produce highly axisymmetric and reproducible nozzles

3.7.1 Experimental setup and procedure

The experimental setup involves the same elements seen in section **¡Error! No se encuentra el origen de la referencia.**. The only change consists in orientating the burner horizontally as shown in Figure 3.33, thus getting a lateral flame which is not symmetric. The heating position of the capillary continues to be defined in a coordinate system (r, z) associated to the burner tube (Figure 1.6 right). The procedure is exactly the same as that used to manufacture nozzles by SVF and TVF approaches (section 3.6.2).

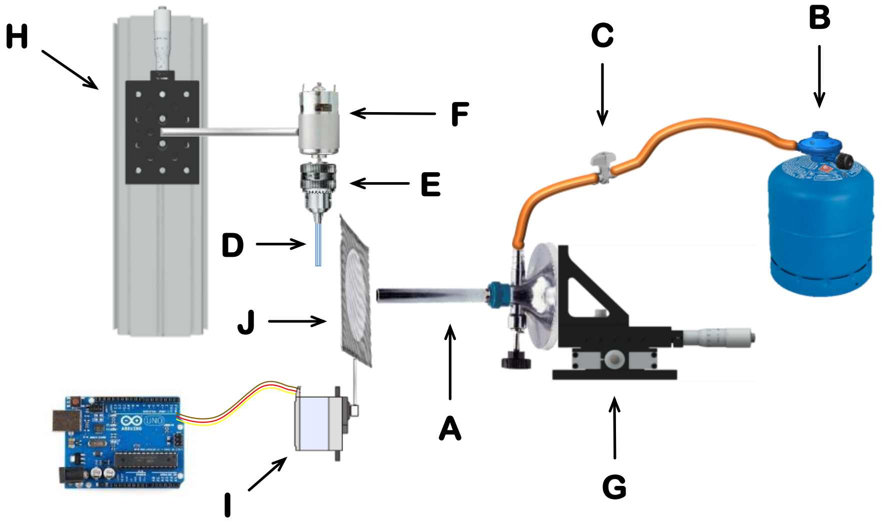

Figure 3.33 Experimental setup for TLF flame shaping. (A) Bunsen burner, (B) butane bottle and regulator, (C) gas valve in the hose, (D) capillary, (E) drill chuck, (F) DC motor for capillary rotation, (G) burner holding element on a two-axis translation stage and for horizontal positioning, (H) one-axis translation stage for vertical positioning, (I) servo and (J) ceramic plate for heating time control.

3.7.2 Optical characterization of the nozzles

Nozzle geometry can be analysed thanks to the optical characterization method described in section 3.6.3. The evaluation of nozzle symmetry was improved: instead of using the old values e_n and e_g that measured the deviation between left and right profiles at different sections, it gets replaced by a single offset value e, thus simplifying nozzle description.

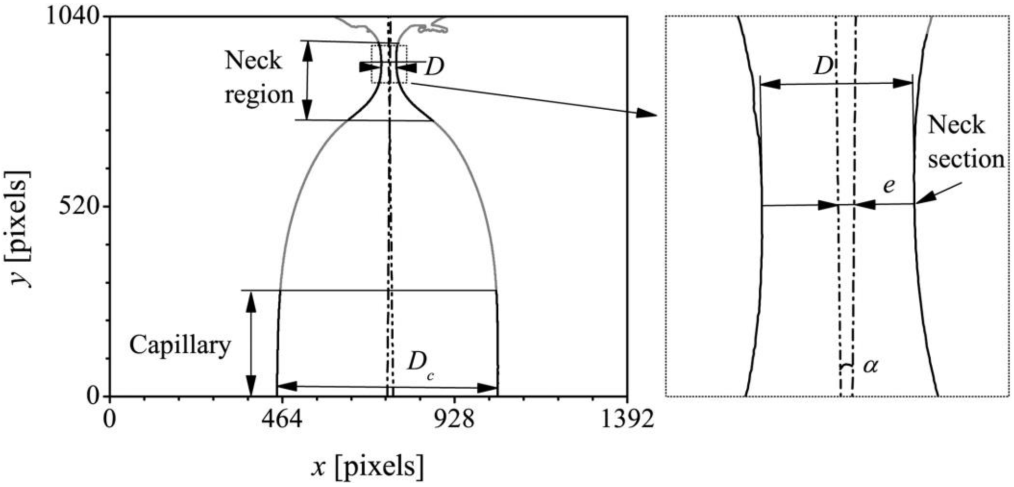

Figure 3.34 Detected contours for a TLF nozzle, capillary (dash-dot line) and neck (dash-dot-dot line) symmetry axes, misalignment angle α and offset distance e at the neck plane.

The offset e measures the distance between the two axes (neck and capillary) at the neck plane. So together with the misalignment angle α, they completely describe the symmetry of the nozzle (or the lack of it), as shown in Figure 3.34.

In sum, for each nozzle we obtain three sets of values D, α and e, each one corresponding to one view. To get the global values for the nozzle, neck diameter is calculated as the mean value of the views, with the standard deviation as an estimation of the measurement uncertainty. In contrast, the axes misalignment angle α and offset distance e for the nozzle are the maximum of the three views.

As mentioned in section 3.6.3, the three mean profiles (one per view) overlap over the whole length, even if the six detected lef-right contours do not due to asymmetry. From now on, one single mean profile is used to characterize each nozzle shape.

3.7.3 Flame temperature analysis

The heating temperature and the temperature profile affect not only the heating time to produce a particular diameter nozzle, but also the nozzle shape. The same procedure than for the vertical flame (section 3.6.4) allowed the lateral flame to be characterized. More details can be found in Paper VII.

Although these measurements do not match the capillary temperature, the measured temperature jump in the radial coordinate relates with the gradient that will appear in the glass along the capillary axis, and therefore with the length of the resulting nozzle.

The slope of this jump for the lateral flame is between those found in the vertical flame when approached from the side (SVF, steep jump) or from the top (TVF, smooth temperature variation). Then, it seems reasonable to think that nozzles produced by TLF will be longer than those produced by SVF, but still shorter than those produced by TVF.

3.7.4 Diameter reproducibility and symmetry

To analyze the reproducibility of the nozzle diameter with the new TLF approach, series of ten nozzles were manufactured with the same heating conditions. In total, six series of experiments were done (conditions shown in Table 3-8). Three different heating positions (r, z) were chosen to have the same measured temperature at the flame (about 900 °C). For each of them, two different heating times t were chosen arbitrarily to get neck diameters in the range between 50 and 400 μm.

Table 3-8 Mean characterization values and shaping conditions for six series of nozzles produced by TLF.

Series	***z* (mm)**	***r* (mm)**	***t* (s)**	***D* (μm)**	***α* (°)**	***e* (μm)**	***ΔL* (mm)**
1	15	8	65	179 ± 16	0.7 ± 0.5	13 ± 4	1.25 ± 0.05
2	15	8	130	54 ± 11	1.0 ± 0.4	16 ± 9	1.44 ± 0.04
3	20	10.25	70	151 ± 12	0.6 ± 0.3	9 ± 5	1.21 ± 0.03
4	20	10.25	85	98 ± 18	0.5 ± 0.3	8 ± 5	1.27 ± 0.03
5	25	12.5	50	375 ± 39	0.7 ± 0.2	13 ± 7	1.01 ± 0.03
6	25	12.5	70	263 ± 31	0.5 ± 0.3	9 ± 5	1.07 ± 0.03

The average geometrical results from Table 3-8 show that diameter reproducibility for TLF is good, similar to that obtained with the SVF approach (Table 3-4), and definitely much higher than the corresponding for TVF (Table 3-6). The nozzle symmetry is also very good, with a misalignment angle α of the neck and capillary axes typically below 1° and an offset distance e between them below 20 μm at the neck section. So the symmetry is comparable to that produced by TVF and much better than that obtained by SVF. We can conclude here that TLF overcomes the two main limitations of nozzles manufactured with a vertical flame.

3.7.5 Shape reproducibility

Shape reproducibility is analysed by comparing the mean profiles of nozzles of about the same neck diameter. Table 3-9 summarizes the sets of two nozzles whose shape will be compared. First, six sets of two nozzles from the same series, i.e. that have been produced with the same heating conditions, are compared in Figure 3.35. The overlapping of the profiles is really good for all the cases. Therefore, for the same manufacturing parameters (same series), not only the diameter is highly reproducible, but also the shape.

Sometimes, a similar diameter was obtained for nozzles produced under different conditions. On the one hand, this can happen when keeping the same heating position but varying the heating time. Examples of this are sets G and H, whose shape comparison is shown in Figure 3.36. Despite the significant difference in heating time between the nozzles in each set, the overlapping of the profiles is very good. So it is reasonable to think that the nozzle shape in TLF is mostly determined by the heating position.

Table 3-9 Geometrical parameters for sets of two nozzles of similar diameters manufactured by TLF.

Set	Series	Nozzle	D (µm)	α (°)	e (µm)	ΔL (mm)
A	1	1	173 ± 3	1.3	15	1.23
		2	176 ± 1	0.8	13	1.28
B	2	1	50 ± 1	0.6	5	1.42
		2	51 ± 2	0.5	8	1.42
C	3	1	152 ± 1	1.1	17	1.20
		2	154 ± 1	0.4	10	1.20
D	4	1	80 ± 1	0.9	13	1.30
		2	84 ± 4	0.3	1	1.30
E	5	1	384 ± 5	0.4	8	0.99
		2	389 ± 4	0.9	21	1.01
F	6	1	214 ± 3	0.7	9	1.11
		2	228 ± 1	0.6	4	1.11
G	3	1	141 ± 2	1.2	16	1.26
	4	2	139 ± 6	0.2	8	1.26
H	5	1	309 ± 3	0.4	5	1.04
	6	2	293 ± 2	0.5	11	1.03
I	3	1	165 ± 7	1.0	12	1.17
		2	170 ± 2	0.5	7	1.18
J	1	1	151 ± 6	1.4	21	1.30
		2	152 ± 5	0.5	11	1.39
K	2	1	68 ± 6	2.0	36	1.48
		2	70 ± 3	1.2	19	1.42
L	1	1	199 ± 1	0.4	11	1.22
		2	202 ± 6	0.5	13	1.21

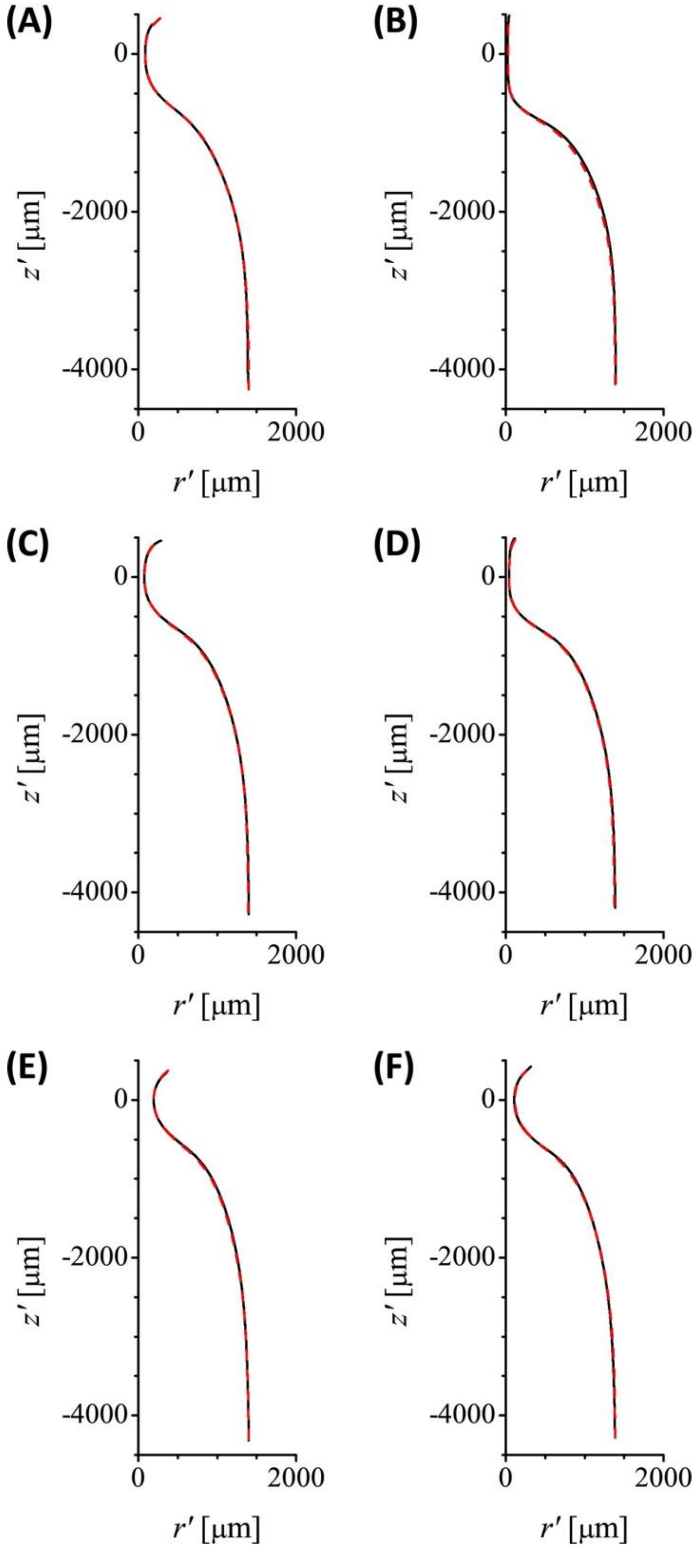

Figure 3.35 Shape comparison of nozzles of the same diameter from the same series (equal manufacturing conditions). Each graph shows nozzle 1 (black solid line) and nozzle 2 (red dashed line) of the set at the top-left corner. Corresponding geometrical parameters are given in Table 3-9.

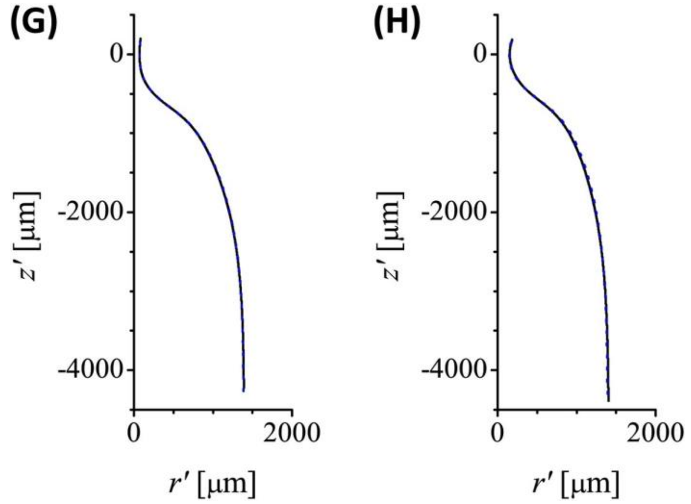

Figure 3.36 Shape comparison of nozzles of the same diameter produced in the same position, but with different heating times. Each graph shows nozzle 1 (black solid line) and nozzle 2 (blue dashed line) of the set at the top-left corner. Corresponding geometrical parameters are given in Table 3-9.

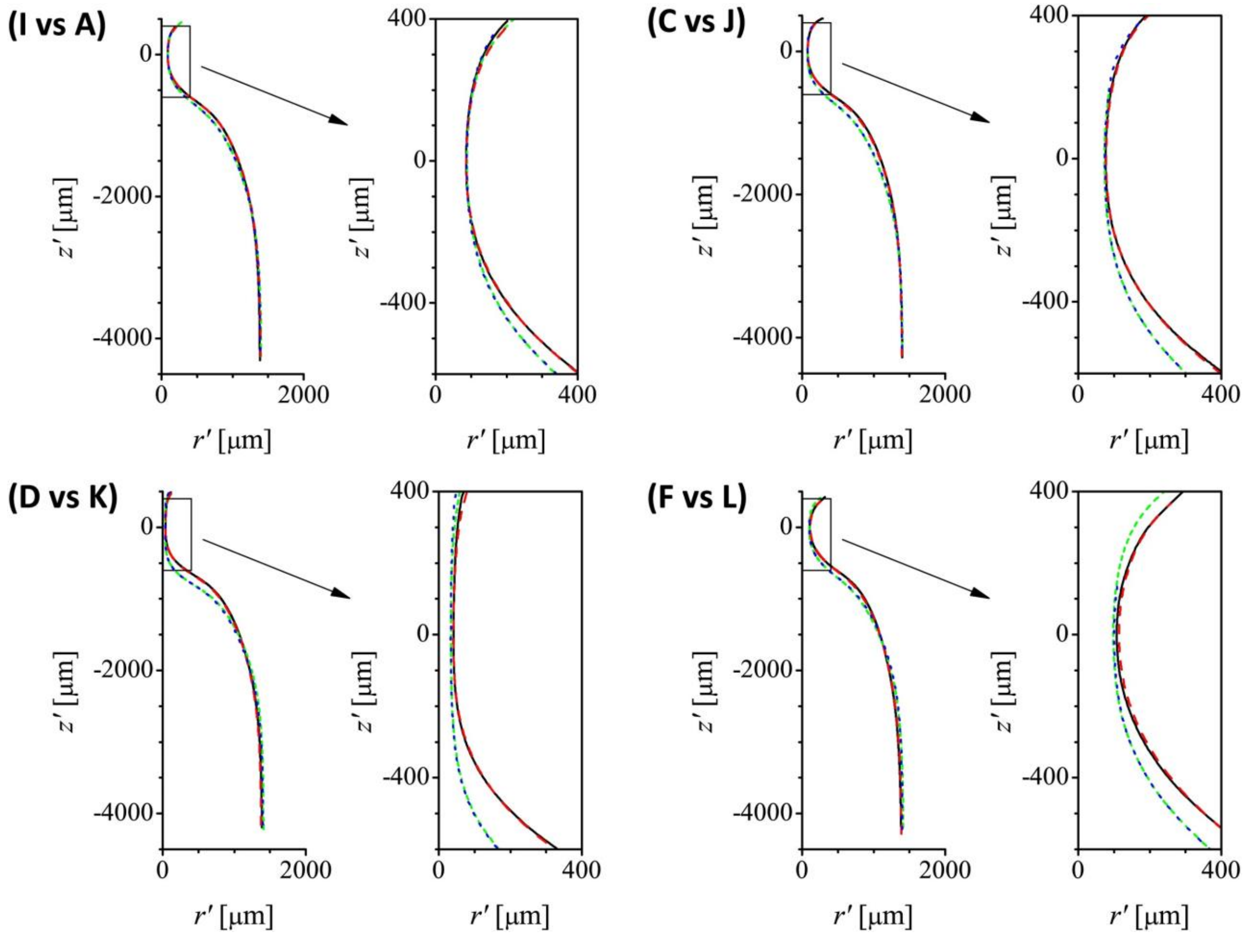

Figure 3.37 Shape comparison of nozzles of the same diameter produced in different conditions (position and time). Each graph compares four nozzles of the sets at the top-left corner: nozzle 1 (black continuous) and nozzle 2 (red dashed) of the first set (always further to the burner exit), and nozzle 1 (green short-dashed) and nozzle 2 (blue dotted) of the second set. Corresponding geometrical parameters are given in Table 3-9.

On the other hand, the same diameter can be achieved for different heating positions, but this also requires the heating time to be different. Figure 3.37 compares the shape of sets of nozzles of similar diameter manufactured in different conditions, so four nozzles are shown in each graph. As discussed for Figure 3.35 and Figure 3.36, when the two nozzles are manufactured in the same position, the profiles overlap perfectly. However, the change in the heating position implies a significant change in shape, probably caused by the different capillary temperature profiles during the process. Sets of nozzles heated closer to the burner (green short-dashed and blue dotted lines) have a longer neck channel, with the diameter reduction happening more gradually along the capillary axis.

3.7.6 Shape comparison with fire-shaped nozzles using a vertical flame

As already pointed out, the nozzle shape depends on the temperature gradient appearing in the capillary. Therefore it is affected by the fire shaping approach, which yields different temperature profiles in the flame characterization.

In order to compare the shape of nozzles manufactured by different approaches, the heating position (r, z) is given in all cases according to the burner coordinate system (Figure 1.6). The comparison is always performed for nozzles of the same diameter.

Nozzles to illustrate the previous approaches TVF and SVF are taken from Muñoz-Sánchez and Cabezas (2018), and their geometrical parameters are shown in Table 3-10. On the other hand, the geometrical parameters for TLF nozzles used for this comparison can be found among the sets in Table 3-9.

Table 3-10 Geometrical parameters of nozzles shaped with a vertical flame to be compared against TLF.

Approach	**z (mm)**	**r (mm)**	**t (s)**	**D (μm)**	**α (°)**	**e (μm)**	**ΔL (mm)**
SVF	17	8	300	393 ± 11	6.0	17	-
TVF	90	0	30	67 ± 1	1.1	33	1.68

When comparing TLF (nozzle E2 from Table 3-9) against SVF (Table 3-10), Figure 3.38 shows that both approaches get a similar length of the neck channel for the same diameter reduction. However, a much shorter length of the capillary is involved in the flow in SVF, which causes both the inner and outer diameter reduction to occur more sharply than in TLF. As discussed earlier, the temperature profile at SVF is quite steep, so the region of the capillary heated up to a high enough temperature is very short. This might also cause the long heating time (300 s) needed by SVF to produce the same neck diameter as TLF, which obtains it six times faster. Note the advantage in terms of manufacturing times that TLF approach implies.

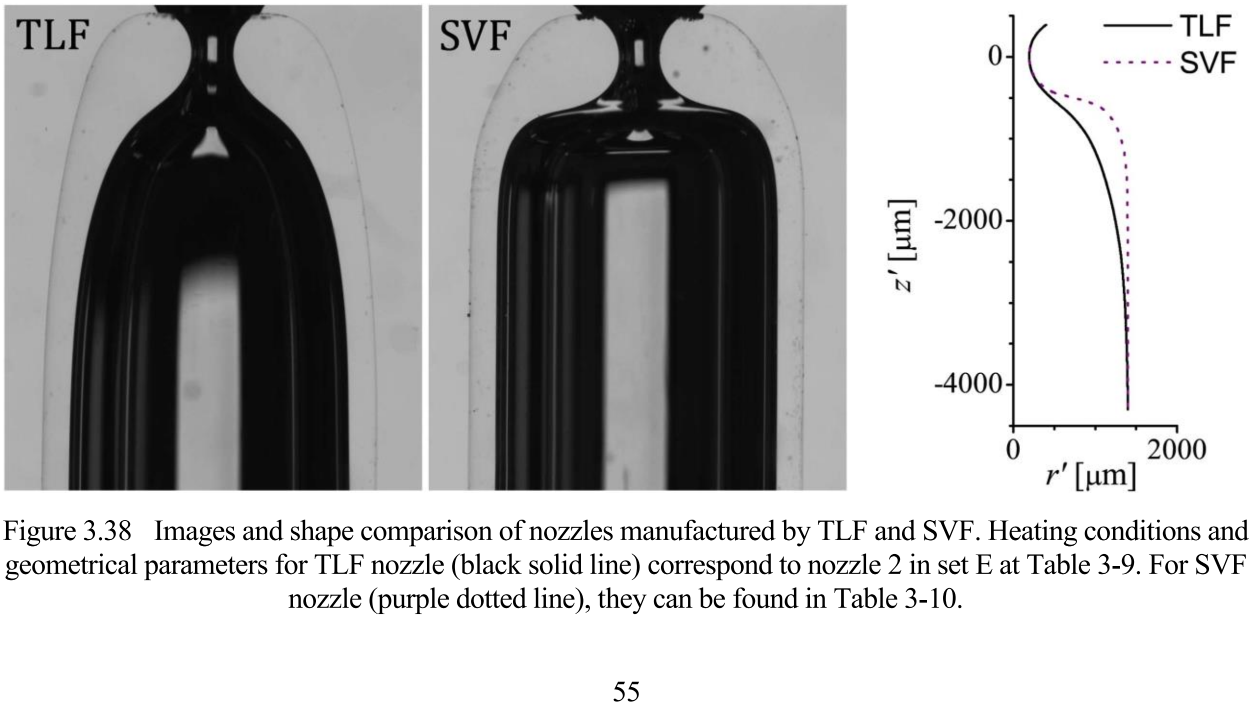

Figure 3.38 Images and shape comparison of nozzles manufactured by TLF and SVF. Heating conditions and geometrical parameters for TLF nozzle (black solid line) correspond to nozzle 2 in set E at Table 3-9. For SVF nozzle (purple dotted line), they can be found in Table 3-10.

With regard to the comparison with TVF approach, Figure 3.39 shows three nozzles of similar diameter: two produced by TLF in different heating conditions - the labels correspond to the set (letter) and nozzle (number) from Table 3-9 -, and one produced by TVF (geometrical parameters in Table 3-10). Vertical lines mark the outer capillary diameter, and the horizontal line helps to visually compare the neck length of the three nozzles.

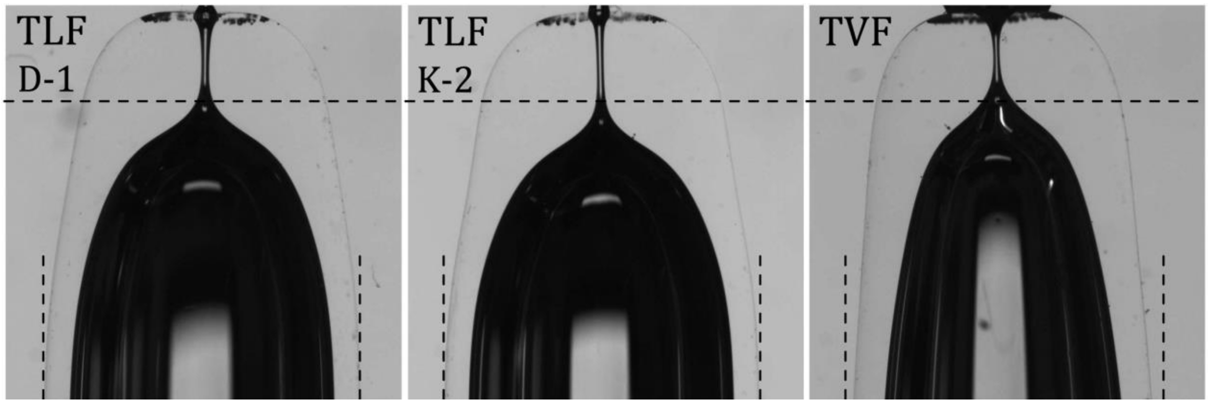

Figure 3.39 Images of nozzles manufactured by TLF (left and center), and TVF (right) whose contours are compared in Figure 3.40. Parameters for TLF nozzles are indicated in Table 3-9 for the set (letter) and nozzle (number) in the label. TVF nozzle parameters appear in Table 3-10.

The shape of the three nozzles is compared in the mean profiles graph in Figure 3.40. The most significant difference between TLF and TVF nozzles lies in the length of the capillary that participates in the diameter reduction. This is again related to the temperature gradients appearing in the capillary during the process. For TVF, a longer portion of the capillary is heated up to participate in the flow, and to a higher temperature. There is more material to produce the thickening of the walls, as shown in Figure 3.39-TVF, where the outer diameter is deformed all along the nozzle. For this reason, TVF nozzles are much longer and have a shorter neck channel than TLF. In addition, heating time is much shorter for TVF (30 s) than for TLF (85 and 130 s).

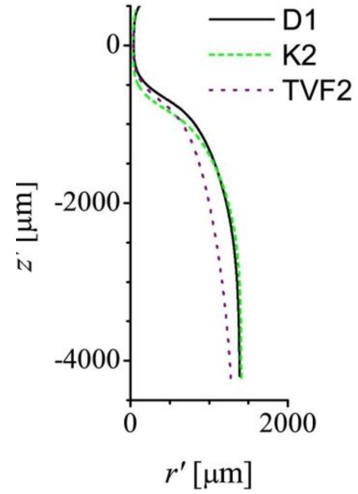

Figure 3.40 Shape comparison of nozzles shown in Figure 3.39 manufactured by TLF (black solid and green dashed lines) and TVF (purple dotted line).

3.7.7 Comparison with pulled nozzles

In order to compare TLF fire shaping against the well-established method of pulling, a set of ten pulled nozzles provided by our capillary supplier were characterized with the method from section 3.7.2. The pipettes were requested to have a 200 µm orifice diameter and the shortest possible taper length.

Figure 3.41 shows, for a typical pulled nozzle, the clear asymmetry already discussed in section 1.5.4.1 and previously reported (Levenstein et al., 2016). Although the misalignment α between the capillary and nozzle axis is below 1°, the offset e between them is really large, as shown in Table 3-11. Therefore, in terms of alignment, TLF nozzles have a superior geometry than pulled pipettes (as shown in Table 3-8 and Table 3-9). Nevertheless, this lack of axisymmetry does not prevent the three mean profiles of the pulled nozzles views to overlap, so a single mean profile can be used to describe each nozzle, as it would happen for fire-shaped nozzles.

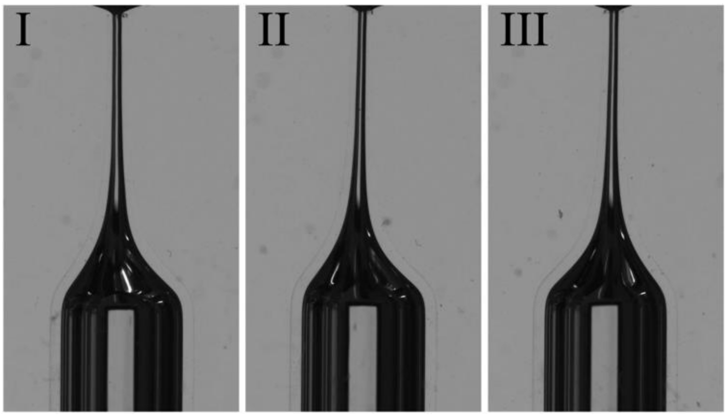

Figure 3.41 Three views of a pulled nozzle

Table 3-11 Geometrical parameters for each view and global for the pulled nozzle in Figure 3.41.

View	D (µm)	α (°)	e (µm)
I	198	0.1	150
II	190	0.9	77
III	198	0.4	128
Nozzle	195 ± 5	0.9	150

In order to assess reproducibility of the pulling process, and as previously done for fire shaping approaches (Table 3-4 for SVF, Table 3-6 for TVF and Table 3-8 for TLF), the geometrical parameters of the ten pulled nozzles series are averaged. The results are shown in Table 3-12. The diameter variability seems to be smaller in pulling than in TLF fire shaping, although further studies in TLF might improve this aspect. The lack of shape reproducibility for pulled nozzles is shown in Figure 3.42, a limitation that is clearly overcome by TLF.

Table 3-12 Mean values of characterization for a series of 10 pulled nozzles.

D (µm)	α (°)	e (µm)
203 ± 8	0.7 ± 0.2	153 ± 33

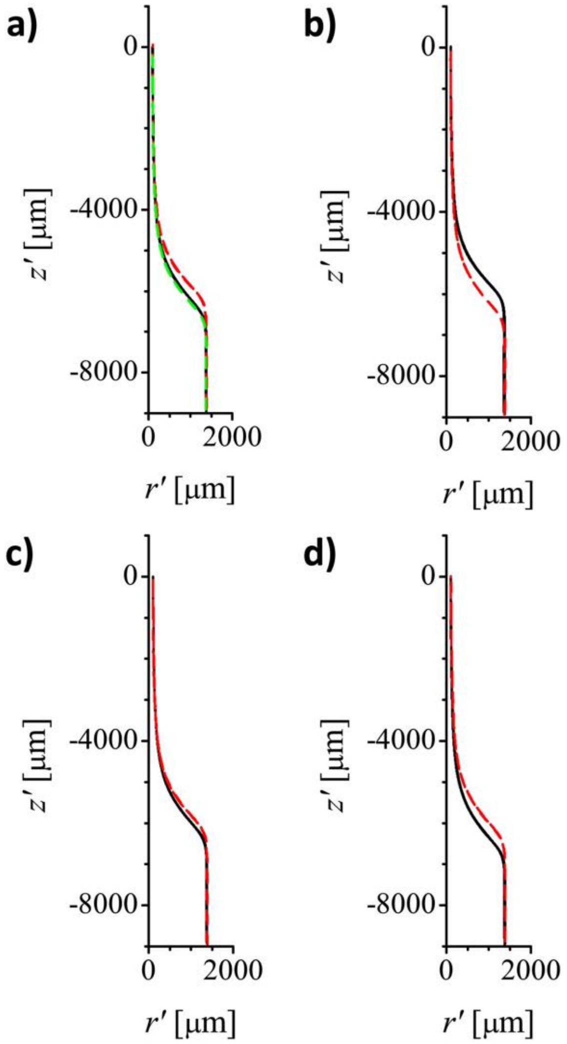

Figure 3.42 Comparison of the mean profiles of different pulled nozzles, grouped to have the same neck diameter.

3.8 Paper VIII: A method for measuring the interfacial tension for density-matched liquids

3.8.1 Theoretical analysis

A liquid bridge of volume $\mathcal{V}$, density ρ_1 and viscosity μ_1 is formed between two horizontal and coaxial disks of radius R_1 separated by a distance H. The surrounding bath (density ρ_2 and viscosity μ_2) has the same height and a radius R_2. The interfacial tension between the two immiscible liquids is σ. In a cylindrical coordinate system as defined in Figure 3.43, the function $\tilde{F}(\tilde{r}, \theta, \tilde{z}; \tilde{t})$ represents the distance between an interface element and the liquid bridge axis.

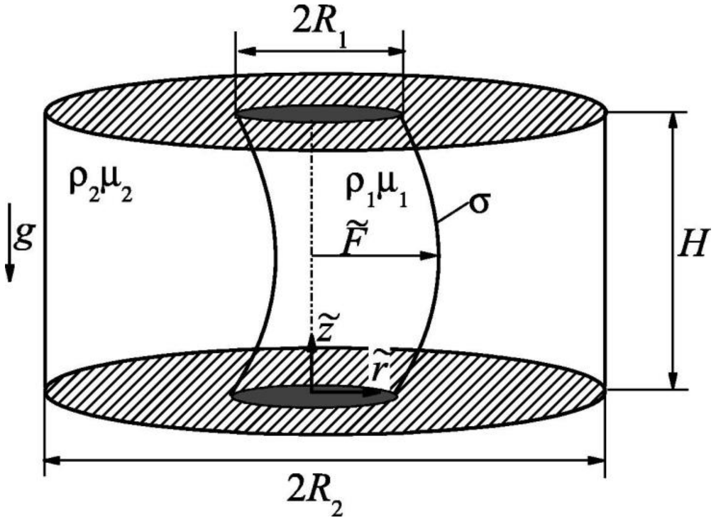

Figure 3.43 Sketch of a liquid bridge within a bath

The governing dimensionless numbers in this problem are the volume ratio $V = \mathcal{V}/(\pi R_1^2 H)$, the slenderness $\Lambda = H/(2R_1)$, the ratio $R = R_2/R_1$ between the radius of the surrounding bath and that of the disks, the density and viscosity ratios $\rho = \rho_2/\rho_1$ and $\mu = \mu_2/\mu_1$, the Bond number $B = |\rho_2 - \rho_1| g R_1^2/\sigma$, and the Ohnesorge number $Oh = (\mu_1\mu_2)^{1/2}(\rho_1 R_1 \sigma)^{-1/2}$.

If the liquid bridge is subjected to a harmonic forcing of frequency ω, which excites the first lateral mode (whose associated resonance frequency is ω_r) along with others, sharp resonance will take place for $\omega \approx \omega_r$. The first lateral mode has been reported to be the most intense amplifier among both axisymmetric and non-axisymmetric linear modes (Ferrera et al., 2016).

In the linear stability analysis, the eigenvalue $\Omega = \Omega_r + i\Omega_i$ characterizing the first lateral mode can be determined as a function of the governing parameters $\{V, \Lambda, R, \rho, \mu, B, Oh\}$. If the Ohnesorge number takes small enough values, $\omega_r \simeq \Omega_i$. This means that the interfacial tension between two immiscible liquids with low or moderate viscosities can be measured by vibrating laterally a bridge of one of those liquids surrounded by the other. In this case, the vibration frequency at resonance ω_r can be equated to the first lateral eigenfrequency Ω_i in dimensional terms:

$$\widetilde{\omega_r} = \frac{1}{2\pi}\left(\frac{\rho_1 R_1^3}{\sigma}\right)^{-1/2} \Omega_i(V, \Lambda, R, \rho, \mu, B, Oh) \tag{3-2}$$

The problem gets simpler for cylindrical ($V = 1$) and inviscid ($Oh = 0$) bridges surrounded by density-matched ($\rho - 1 = B = 0$) liquids contained in large tanks ($R \to \infty$), where the eigenfrequency $\Omega_i = \Omega_{0i}(\Lambda)$ can be calculated analytically (Sanz and Diez, 1989). In these conditions, Eq. (3-2) is transformed in:

$$\sigma = \rho_1 R_1^3 \left[\frac{2\pi\widetilde{\omega_r}}{\Omega_{0i}(\Lambda)}\right]^2 \tag{3-3}$$

In the LaViT method, the resonance frequency $\widetilde{\omega_r}$ is determined by vibrating horizontally the upper disk of the liquid bridge, so the interfacial tension can be calculated from Eq. (3-3). Given that the equation involves the liquid bridge density ρ_1, but not the density difference $\Delta\rho$, the method can be safely applied even when the latter is not accurately known, thus overcoming the limitations of other tensiometry methods, as explained in section 1.6.

A detailed analysis of the appropriate parameter region for LaViT can be found in Paper VIII. The method can provide accurate interfacial tension values taking into account the following conditions:

- The Ohnesorge number must be sufficiently small ($Oh \lesssim 0.01$)
- The radius of the bath lateral wall should be at least five times larger than that of the supporting disks ($R \gtrsim 5$)
- The bridge should be formed with the most viscous liquid
- The liquid bridge slenderness should take intermediate values ($1.5 \lesssim \Lambda \lesssim 2$)
- The liquid bridge volume in the experiments should approximately match cylindrical volume

3.8.2 Experimental analysis

This section analyses the experimental frequency response of liquid bridges of bromodecane ($\rho_1 = 1066$ kg/m^3 and $\mu_1 = 2.33$ mPa·s) surrounded by distilled water ($\rho_2 = 997$ kg/m^3 and $\mu_2 = 0.89$ mPa·s), which have very low mutual solubility. Their small but non-negligible difference in densities ($\Delta\rho = 69$ kg/m^3) allow TIFA-AI to provide reliable measurements of the interfacial tension. Therefore, the experimental resonance frequencies can be checked against those calculated from Eq. (3-3).

The experimental setup in Figure 3.44 allows one to vibrate horizontally the upper disk with a magnetic shaker while the rest of solid surfaces remain still. The liquid bridge is formed between two disks of 2 mm in radius, by injecting the prescribed volume through the lower disk. The bridge is submerged in a bath that is filled manually. The latter is contained in a cubic transparent cell of 40 mm in side and closed at the top.

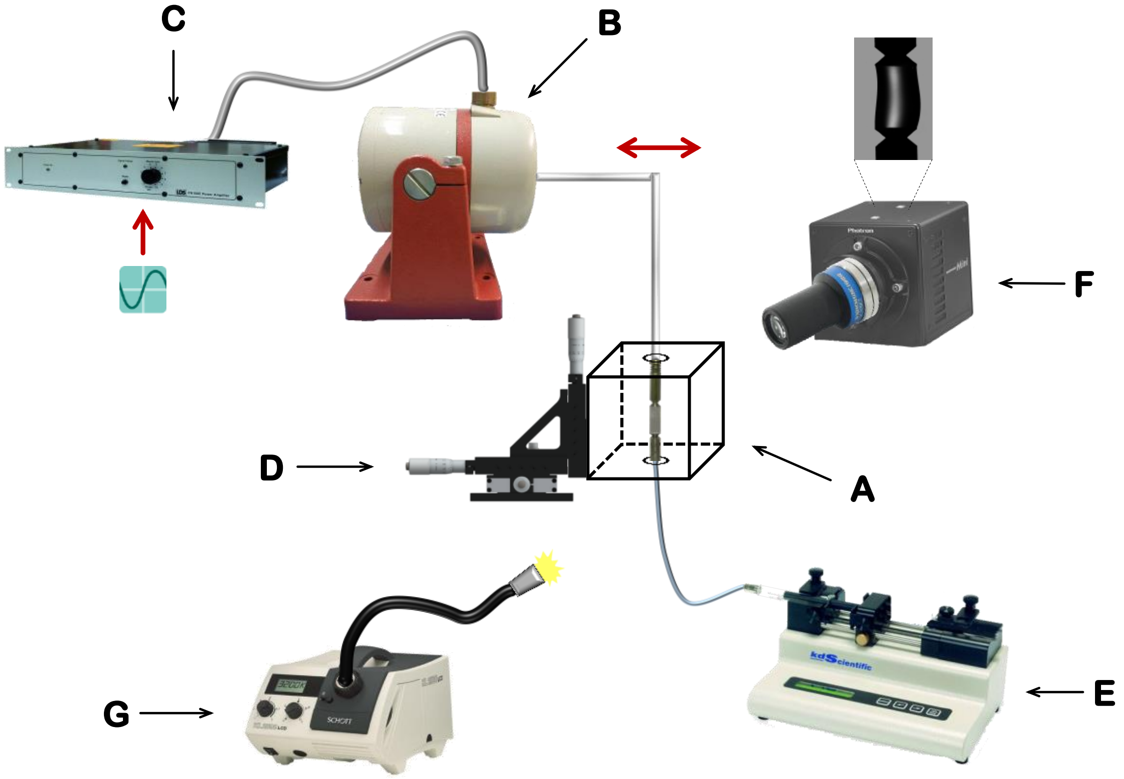

Figure 3.44 Experimental setup for lateral vibration of a liquid bridge submerged in a bath. (A) methacrylate cell, (B) permanent magnetic shaker, (C) amplifier, (D) 3-axis translation stage, (E) syringe pump, (F) high-speed camera equipped with bi-telecentric lens, (G) light source.

The translation stages allow the liquid bridge to be formed with the desired slenderness and to be placed in front of the camera, which acquires shadowgraph images.

Once the liquid bridge is formed, a typical experimental run consists of the following steps:

1) Images of the liquid bridge at equilibrium are acquired and processed with TIFA-AI (Cabezas et al., 2006) to determine the interfacial tension σ, the liquid bridge volume ratio V, and the slenderness Λ.
2) The upper disk is vibrated horizontally with a given amplitude A and frequency $\tilde{\omega}$
3) After some seconds, images of the liquid bridge oscillations are recorded
4) The oscillation frequency $\tilde{\omega}$ is increased while keeping the oscillation amplitude A practically constant
5) The liquid bridge vibration is recorded again for the new frequency value

This procedure is followed until the resonance frequency $\tilde{\omega_r}$ is clearly exceeded. The last step is to take equilibrium images of the liquid bridge to check whether there has been any variations in volume, slenderness, triple contact line position or interfacial tension.

The images of the oscillations are processed to determine (i) the free surface location as a function of time ($\tilde{F}$ in Figure 3.43), and (ii) the trajectory of the upper disk to calculate the vibration amplitude $\tilde{A}$ with sub-pixel resolution (Vega et al., 2011). The results are fitted by a harmonic function. The interface contours are analyzed to determine the maximum deformation $\Delta\tilde{F}_{max}$ with respect to the equilibrium shape for each recorded frequency $\tilde{\omega}$. The transfer function can be calculated as:

$$T(\tilde{\omega}) = \frac{\Delta\tilde{F}_{max}}{\tilde{A}} \tag{3-4}$$

In order to examine the resonance frequency shift due to the nonlinear effects, the transfer function is evaluated for two different oscillation amplitudes, one of them with a relatively large magnitude. Figure 3.45 reveals the little influence of the nonlinear effects, since the two sets of points practically overlap, also showing a good experimental reproducibility. In addition, the observed resonance frequency differs in less than 2.5% from the value calculated with Eq. (3-2).

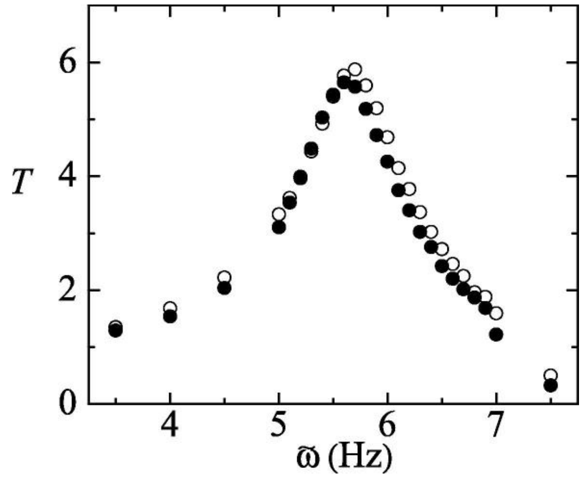

Figure 3.45 Transfer function $T(\tilde{\omega})$ for $\tilde{A}$ = 30 (open symbols) and 57 µm (solid symbols). The results were obtained for {Λ = 1.47, V = 1.04, ρ = 0.933, μ = 0.396, B = 0.152, Oh = 0.0081}.

The possible hysteresis behavior was checked by reversing the forcing frequency sweep for the same liquid bridge. The comparison in Figure 3.46 shows hysteresis to be almost negligible, which confirms that nonlinear effects play no significant role. In this case, the resonance frequency deviated in less than 0.8% from the theoretical prediction (Eq. (3-2)).

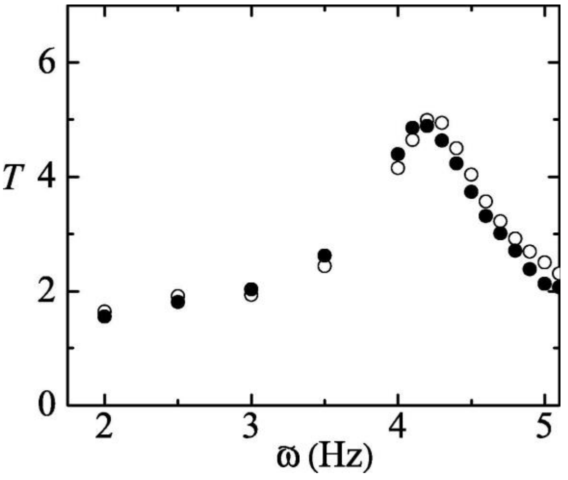

Figure 3.46 Transfer function $T(\tilde{\omega})$ for $\tilde{A}$ = 26 μm measured by increasing (open symbols) and decreasing (solid symbols) the vibration frequency. The results were obtained for $\{\Lambda = 1.99, V = 0.99, \rho = 0.933, \mu = 0.396, B = 0.146, Oh = 0.0079\}$.

The resonant peaks in Figure 3.45 and Figure 3.46 are wider than predicted in the theoretical analysis, due to the relative motion between the solid elements when only the upper disk is vibrated. Therefore, this section approaches a simple alternative to sharpen the peak: the horizontal vibration of the surrounding bath while both disks remain still.

Ideally, a completely filled and hermetically closed cell would be vibrated together with the disks as a solid body. Nevertheless, this would complicate the experimental setup, so the bath is left open with a free surface. In this case, the existence of another free surface makes the bath resonate. So, as shown in Figure 3.47 for two different heights of the bath, the liquid bridge acts a sensor of the bath resonance, rather than a resonant system itself.

For both cases depicted, the first resonance peak corresponds to the first modal frequency of the surface waves produced by the bath vibration (Feng, 1997). This frequency depends on the liquid bath height and is similar to that of the bridge. In addition, the resonance peak can be higher for the bath than for the liquid bridge (as it happens in the experiment with closed symbols). Such interference prevents the use of this simple vibration system since it may yield misleading results.

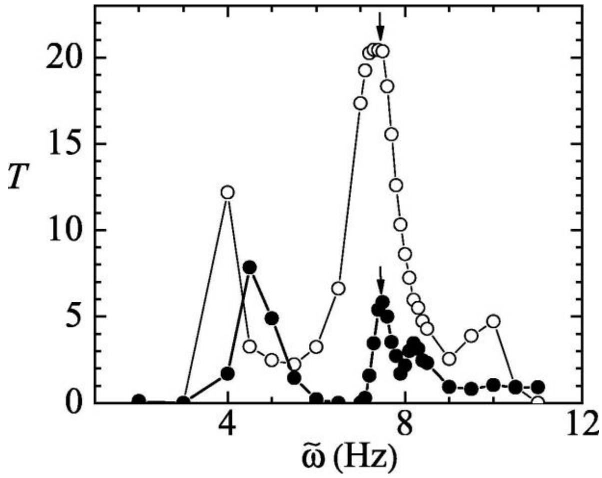

Figure 3.47 Transfer function $T(\tilde{\omega})$ when the surrounding liquid bath is vibrated horizontally with two different heights around the same liquid bridge. The arrows mark the liquid bridge resonance frequency. The results were obtained for $\{\Lambda = 1.47, V = 0.858, \rho = 0.933, \mu = 0.396, B = 0.117, Oh = 0.0071\}$.

3.8.3 The LaViT method

The LaViT method is based on forming a cylindrical liquid bridge of the most viscous fluid with $\Lambda \simeq 2$, whose upper disk will be vibrated following the experimental run described in section 3.8.2.

If the camera in Figure 3.44 is replaced by a camera with a large exposure time, the resonance frequency is easy to identify with the naked eye when the blurred bridge contour widens the most. In the case illustrated in Figure 3.48, resonance occurs for 4.0 Hz.

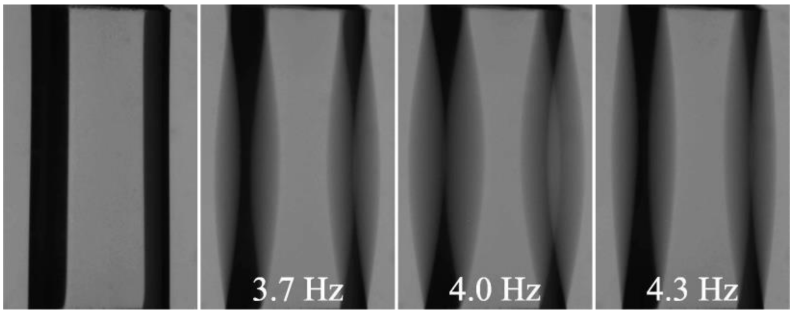

Figure 3.48 Images of a liquid bridge of bromodecane-toluene (1:0.97 molar ratio) submerged in water at equilibrium (left-hand image) or vibrating horizontally at different frequencies.

Once the resonance frequency $\widetilde{\omega_r}$ is determined, the interfacial tension σ can be calculated from Eq. (3-3), where $\Omega_{0i}(\Lambda)$ can be approximated by the function:

$$\Omega_{0i}(\Lambda) = 0.162\,\Lambda^2 - 0.938\,\Lambda + 1.804 \qquad (3\text{-}5)$$

Eq. (3-5) constitutes a fit to the inviscid analytical solution obtained by Sanz and Díez (1989) for values ($1.7 \lesssim \Lambda \lesssim 2.5$). Figure 3.49 shows the good agreement between this simplification (solid circles) and the use of the full numerical solution (triangles).

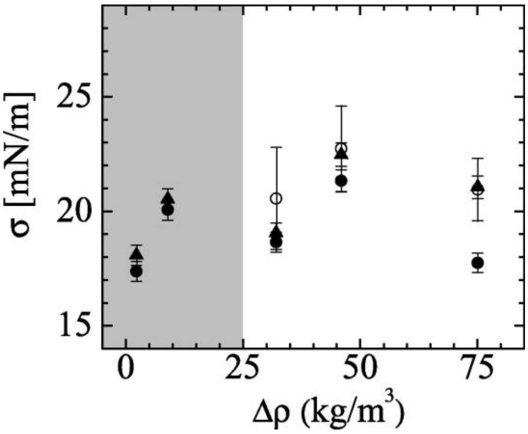

Figure 3.49 Interfacial tension σ between water and several mixtures of bromodecane-toluene characterized by the density difference $\Delta\rho$, measured with TIFA-AI (open circles) and LaViT -either calculated with Eq. (3-5) (solid circles) or the full numerical solution (triangles)-. The grey region indicates the range of $\Delta\rho$ for which the TIFA-AI algorithm does not properly converge to an interfacial tension value.

With this simple method, accurate values of the interfacial tension can be obtained, as checked when comparing against TIFA-AI (Cabezas et al., 2006) (open symbols in Figure 3.49). For the grey region, where $\Delta\rho$ takes small values, TIFA-AI was found unable to converge to an interfacial tension solution; whereas LaViT can still lead to an accurate result even for $\Delta\rho \rightarrow 0$. Therefore, LaViT is proved to overcome the inability of any drop shape technique to provide reliable results when the Bond number vanishes. In addition, the uncertainty in the measurement of the densities is responsible of the large error bars for TIFA-AI. This is not a significant source of error for LaViT, which shows much smaller error bars, calculated from the resonance frequency uncertainty (± 0.05 Hz).

Additionally to the accuracy in the interfacial tension measurement, the advantages of LaViT can be summarized as:

- The experimental setup is relatively simple. Given that resonance frequency is expected to take values in the order of a few hertz, an even simpler mechanical shaker can be used.
- The vibration amplitude does not require to be controlled as far as it is kept practically constant throughout the experimental run.
- Since the resonance frequency is a robust property of the liquid bridge, the method is hardly affected by little defects of the experimental setup, like the slight misalignment of the supporting disks or small differences between their sizes.
- Image processing is not required, as it would happen for drop shape techniques.
- The method does not require to know the density difference $\Delta\rho$ between the liquids, but only the liquid bridge density ρ_1.

4 CONCLUSIONS

4.1 Paper I: Droplet impact onto moving liquids

I. The regime diagram in Figure 3.5 could be used to predict the splashing behaviour for different conditions. Some practical applications might need to enhance mixing by vortex shedding (splashing regime), whereas other industrial environments where good droplet placement is necessary (e. g. inkjet printing) would aim for smooth coalescence. In addition, the regime map should constitute a valuable tool to validate numerical models for a wide range of parameters.

II. The different behaviours of drops impacting a moving liquid pool are well parameterised by the common splashing parameter *K*, which encompasses all the drop properties and had formerly described drop impact onto stationary liquid films (Josserand and Zaleski, 2003; Thoraval et al., 2012) and onto moving solid substrates (Bird et al., 2009).

III. The onset of splashing in our experiments occurs for $K = 800$, a much lower value than that found for impact of drops on static thin liquid films ($K \sim 2000$) (Cossali et al., 1997; Yarin, 2006). This might be caused by the extra inertia added to the system by the moving liquid target.

4.1.1 Future directions

I. Recent studies suggested that the surrounding gas also plays a role in regulating splashing on solids (Liu et al., 2015; Riboux and Gordillo, 2014). For impact onto liquids, some evidence indicates that the splashing threshold is also affected by the ratio between the liquid and the gas viscosities, effectively introducing a third dimensionless parameter, μ_l/μ_g (Josserand and Thoroddsen, 2016; L. V Zhang et al., 2012). Further experimental studies could concentrate on the effect of these factors, thus offering an additional insight into novel methods to suppress the undesired effects of splashing.

II. Experiments in this work were all performed at a pool depth of 6.0 mm. Preliminary experiments had shown that the impact behaviour is not affected by the pool depth as long as it is deeper than 5.0 mm. Nevertheless, the impact behaviour of fast droplets onto stationary pools is known to depend on the pool depth (Thoraval et al., 2013) and this effect might be a matter for a future work.

4.2 Paper II: A novel technique to produce metallic microdrops for additive manufacturing

I. A novel technique to produce a continuous droplet stream of a low-melting-point alloy has been proposed and its performance analysed.

II. The tip of a metal wire is melted by an induction coil as it is introduced in the ejecting nozzle. This melting process has been optimized to get a periodic dripping onto the metal pool formed in the nozzle.

III. Liquid metal is ejected through the nozzle by applying a pressure on the pool free surface. Conditions of quasi-steady jetting have been reached by properly adjusting the control parameters.

IV. Jet breakage occurs spontaneoulsy by the growth of capillary waves over the free surface, giving raise to a train of droplets. Both the wavelength of the dominant perturbation and the resulting droplets diameter roughly agree with Rayleigh's prediction (Rayleigh, 1878).

4.2.1 Future directions

I. The technique could be adapted to process alloys of higher melting points. For this purpose, the maximum power of the induction coil must be increased, and the glass nozzle must be replaced by, for instance, one made of quartz.

II. The performance of the technique could get improved by applying the "surface jetting" concept (Vega et al., 2013). If the gauge pressure Δp_2 is significantly increased, a high-speed coflowing stream of nitrogen is established. This current stabilizes the jet by dragging the surface waves, therefore producing jets with smaller kinetic/interfacial energy ratios.

    a. The drag of capillary waves can be considerably enhanced by increasing the nitrogen temperature (viscosity).

    b. A proper alignment between the inner and outer nozzles and a fine tuning of their diameter and shape are necessary to control the coflowing stream. Therefore any advances in fabrication of fire-shaped nozzles through Paper VI and Paper VII will benefit the application of "surface jetting".

III. The technique is proposed to be applied to a manufacturing method. The complete apparatus would consist of a chamber containing the described droplet generator, mounted onto a vertical translation system, and a substrate platform to be displaced horizontally. A control system would coordinate the droplet generation, the horizontal and vertical movements, and the chamber temperature.

IV. Non-continuous droplet production might be helpful to implement the manufacturing method. If this need is detected, drop on demand generation could be explored through pneumatic actuation over the ejection pressure Δp_1. In this case, it would be critical to coordinate the periodic dripping that feeds the pool from melting and the ejection rate produced by the pressure pulses, in order to keep a fairly constant level of the metal pool.

4.3 Paper III: Generation of micro-sized PDMS particles by a flow focusing technique for biomicrofluidics applications

I. A flow focusing technique has been applied to produce PDMS microparticles with diameters below 10 µm and a relatively high degree of monodispersity.

II. Such small particles are produced with orifices of about 200 µm in diameter, thereby avoiding the clogging of the injection system.

III. The size of the PDMS precursor droplets can be selected and controlled by shifting the needle position along the axis of the glass capillary.

IV. A pronounced shrinkage of these droplets has been found to occur while curing into solid microparticles.

V. Preliminary measurements of a suspension with these particles have shown a similar rheological behaviour than a suspension of ovine RBCs. The generated PDMS particles seem to have a great potential to mimic the mechanical properties of blood cells.

4.3.1 Future directions

I. The degree of monodispersity could be improved by precisely controlling the wavelength of the breakage of the jet, e.g., by using a piezoelectric mechanism.

II. The shrinkage phenomenon needs to be further explored and characterized, so the diameter of the resulting cured particles is the desired one. This aspect is addressed in Paper IV of this thesis.

III. Although the size is controlled, other mechanical properties of the microparticles need to be characterized, so their use can be evaluated for different biomedical applications, for example to develop blood analogues. Paper V of this thesis explores this issue in detail.

IV. The low production rate of the technique (approximately 2 ml of emulsion per hour) would need to be improved.

4.4 Paper IV: Shrinkage and colour in the production of micro-sized PDMS particles for microfluidic applications

I. The shrinkage phenomenon in PDMS curing has been calibrated for the production of microparticles. Nor the amount of curing agent neither the presence of enclosed micro/nanoparticles within the PDMS precursor affect shrinkage. It is rather determined by the surface-to-volume ratio of the liquid precursor droplets (Figure 3.18), which is relevant for small diameters but negligible for larger ones.

II. The technique is able to work within a wide range of viscosities from the different PDMS precursors, always obtaining microparticles with a relatively high degree of monodispersity.

III. The visualization/detection of the particles has been improved by developing an in-house simple protocol to colour PDMS precursor.

IV. The technique is able to encapsulate micro/nanoparticles within PDMS spheres of a few microns in diameter. Such microcapsules can be potentially applied to a wide range of technological fields, from biomedicine (Kalambur et al., 2005; Rodrigues et al., 2016a; Saidur et al., 2011) to industrial applications as cooling or solar thermal energy (Khullar et al., 2014; Verma and Tiwari, 2015).

4.4.1 Future directions

Despite the fact that the ratio Part A:Part B of the PDMS precursor or the addition of pigment have no influence on the production phase of the PDMS, a natural question is whether the properties (e. g. flexibility) of the resulting particles depend on these factors. Paper V of this thesis will evaluate this aspect.

4.5 Paper V: Flexible PDMS microparticles to mimic RBCs in blood particulate analogue fluids

I. Several microcirculation phenomena have been checked for suspensions of PDMS microparticles with different crosslinking ratios and pigmentation. Their flow behaviour has been compared against suspensions of human RBCs, both healthy and pathological.

II. For the first time, the Deformation Index (DI) has been measured and compared for different PDMS microparticles, by visualizing the flow through a hyperbolic-shaped contraction.

   a. All PDMS microparticles present some ability to elongate when passing through the smallest dimension of the microchannel. Nevertheless, they recover their spherical shape in the expansion regions faster than RBCs.

   b. The samples with the highest DI were the transparent PDMS mixtures. All the crosslinking ratios showed a comparable deformability among them, yielding a midway DI value between healthy and pathological RBCs.

   c. However, pigmented microparticles show reduced DI values, so they do not seem adequate to replicate RBCs in the development of particulate analogue fluids.

III. Rheological measurements have shown that a suspension of transparent PDMS microparticles reproduces the viscosity curve of human RBCs suspensions, showing an intermediate shear-thinning degree between healthy and pathological RBCs.

IV. Such suspension of transparent PDMS microparticles forms a cell-free layer (CFL) near the walls of the microchannel, in the same way as suspensions of human RBCs (either healthy or pathological).

V. Transparent PDMS microparticles produced by needle focusing emerge as good candidates to mimic diseased RBCs, such as those with an intermediate status of Diabetes Mellitus type II. They show a great potential to develop particulate blood analogue fluids with hemorheological behaviour similar to *in vitro* blood suspensions.

4.5.1 Future directions

I. Since visualization is enhanced for coloured microparticles when flowing through microchannels, it would be desirable to further develop this type of particles in terms of deformability.

II. A scale-up of the production to obtain a higher concentration of microparticles would allow more detailed studies and applications.

4.6 Paper VI: Borosilicate nozzles manufactured by reproducible fire shaping

I. Fire shaping of glass nozzles with a vertical flame has been systematically studied for the first time.

II. A new experimental setup has been proposed. It automates the manufacturing process in contrast to manual methods used by researchers to produce fire-shaped nozzles in the past.

III. The two traditional configurations for vertical flames have been explored: a horizontal capillary heated on the side of the flame (SVF), and a vertical capillary heated at the top of the flame (TVF).

IV. The performance and reproducibility of both approaches have been assessed by optically characterizing the resulting nozzles, through a whole set of parameters that evaluate nozzle geometry.

V. The flame temperature profile for different heating positions has been measured and analysed, given its influence in the process.

VI. SVF approach presents a steep temperature profile with low fluctuations. Resulting nozzles are therefore short, with a small neck diameter dispersion for the same process parameters. Nevertheless, SVF nozzles neck is significantly misaligned with respect to the original capillary. This asymmetry makes these nozzles unacceptable for some applications, since the capillary is typically used to align the nozzle in the experimental setup.

VII. In TVF, temperature fluctuations are more important, and the profile varies smoothly troughout a longer region. Resulting nozzles are longer than in SVF, with a gradual reduction of the inner and outer diameters of the capillary. Asymmetry from SVF is here overcome, since the misalignment of the nozzle neck and the capillary was very low. However, the nozzle size is difficult to reproduce, with a very high dispersion of the neck diameter for the same conditions.

   a. Controlling the resulting neck diameter with the heating time is not possible for TVF. Nevertheless, the relation between the neck diameter and the shortening of the capillary falls on one single curve, even for different conditions. Hence the capillary shortening may be an alternative parameter to control the nozzle size.

   b. Shape reproducibility is extremely good for TVF. Even for different process parameters (heating position and time), nozzles of the same diameter have essentially the same shape.

4.6.1 Future directions

The misalignment found for SVF or the lack of reproducibility in the size of TVF nozzles may discard fire-shaped nozzles for applications that strongly depend on the alignment of the elements or the neck diameter.

However, it is worth further exploring fire shaping, in order to produce nozzles with a very different geometry than that of pulled pipettes. Therefore, Paper VII intends to overcome the two main limitations of nozzles manufactured with a vertical flame.

4.7 Paper VII: A new fire shaping approach to produce highly axisymmetric and reproducible nozzles

I. A new fire shaping approach (TLF) has been proposed to combine the benefits of previous ones, which were based on a vertical flame (SVF and TVF). TLF heats the tip of a rotating vertical capillary at the top of a lateral flame.

II. The lateral flame has been characterized. The temperature profile, with an intermediate steepness between those of SVF and TVF, suggests that TLF will not be able to produce nozzles as short as SVF.

III. TLF has successfully produced nozzles with neck sizes between 2% and 15% of the original capillary inner diameter. Although it would be possible to produce smaller neck nozzles by increasing the heating time, this study has been limited to capillary-neck diameter reductions of common use.

IV. Its performance has been analysed and compared against other fire shaping approaches and the commercial pulling method.

V. TLF shows an adequate reproducibility for the nozzle size. Both nozzle symmetry and shape reproducibility are excellent. Different shapes can be achieved when varying the heating conditions.

VI. TLF overcomes the two main limitations of nozzles manufactured with a vertical flame: the poor diameter reproducibility for TVF and the misalignment found for SVF.

VII. When compared against pulling, TLF nozzles show a significantly smaller offset than that found for pulled nozzles, thus overcoming an important limitation of pulling (the lack of axisymmetry). For the heating conditions studied, TLF size reproducibility is smaller but comparable to a set of pulled nozzles.

4.7.1 Future directions

I. It would be interesting to find experimental conditions that improve the size reproducibility.

II. A further study could explore the process limits, including the possibility of producing nozzles as short as SVF.

III. A mathematical function could be searched to describe the nozzle shape.

4.8 Paper VIII: A method for measuring the interfacial tension for density-matched liquids

I. A simple method (LaViT) has been proposed to measure the interfacial tension of density-matched liquids. It consists in vibrating laterally a cylindrical bridge of one of the two liquids submerged in the other, and measure the first resonance frequency. The latter is equated to the eigenfrequency of the first lateral mode so the interfacial tension can be calculated.

II. Unlike drop tensiometry methods, LaViT does not involve the density jump across the interface. Therefore, its accuracy is affected neither by the smallness of the gravitational Bond number nor by significant relative errors of the density difference.

III. The first lateral ($m = 1$) oscillation mode of a liquid bridge immersed in a bath has been analyzed theoretically for arbitrary values of the governing parameters. For the first time, both the eigenfrequency and damping rate of this mode have been calculated, thus extending previous results for non-surrounded (Ferrera et al., 2016; Higuera and Nicolás, 1997; Tsamopoulos et al., 1992) and inviscid (Sanz and Diez, 1989) liquid bridges. These numerical simulations have allowed us to determine the parameter region where LaViT is expected to work satisfactorily, namely:

   a. The Ohnesorge number must be sufficiently small ($Oh \lesssim 0.01$)

   b. The shape and size of the outer bath is irrelevant as long as its radius is at least five times larger than that of the supporting disk ($R \gtrsim 5$)

   c. The bridge should be formed with the most viscous liquid and intermediate values for the slenderness ($1.5 \lesssim \Lambda \lesssim 2$)

IV. The required experimental setup is relatively simple, and the procedure does not require the use of imaging processing techniques. The method is robust and hardly affected by little defects of the experimental setup.

V. The functional principle of LaViT has been experimentally analysed by measuring the transfer function that characterizes the frequency response:

   a. Non-linear effects have been proved to be negligible (boh the hysteresis and the possible resonance shift due to a large oscillation amplitude)

   b. The vibration of the outer bath has been discarded as an alternative, since the resonance of the bath interferes with that of the liquid bridge

VI. The accuracy of LaViT has been assessed by applying it to liquid bridges with sufficiently large Bond numbers, where standard drop shape tensiometry still provides accurate measurements The interfacial tension results agree remarkably well with those measured by TIFA-AI. In addition, LaViT can measure in a region where TIFA-AI is not valid anymore.

4.8.1 Future directions

Although LaViT provides reliable measurements of the interfacial tension for low and moderate viscosities, the resonance frequency could be determined more precisely by reducing the width of the resonance peak. This may be relevant for relatively large Ohnesorge numbers. For such cases, the two disks could be jointly vibrated with a completely filled and hermetically closed cell, which would considerably complicate the liquid bridge formation process. Therefore, a future study would need to explore a simple setup so the method can be extended to higher viscosity liquids.

REFERENCES

Abkarian, M., Faivre, M., Horton, R., Smistrup, K., Best-Popescu, C.A., Stone, H.A., 2008. Cellular-scale hydrodynamics. Biomed. Mater. 3, 034011. https://doi.org/10.1088/1748-6041/3/3/034011

Acero, A.J., Ferrera, C., Montanero, J.M., Gañán-Calvo, A.M., 2012. Focusing liquid microjets with nozzles. J. Micromechanics Microengineering 22, 065011. https://doi.org/10.1088/0960-1317/22/6/065011

Acero, A.J., Rebollo-Muñoz, N., Montanero, J.M., Gañán-Calvo, A.M., Vega, E.J., 2013. A new flow focusing technique to produce very thin jets. J. Micromechanics Microengineering 23, 065009. https://doi.org/10.1088/0960-1317/23/6/065009

Ahn, S., Doerr, S.H., Douglas, P., Bryant, R., Hamlett, C.A.E., McHale, G., Newton, M.I., Shirtcliffe, N.J., 2013. Effects of hydrophobicity on splash erosion of model soil particles by a single water drop impact. Earth Surf. Process. Landforms 38, 1225–1233. https://doi.org/10.1002/esp.3364

Anastasiou, A.D., Spyrogianni, A.S., Koskinas, K.C., Giannoglou, G.D., Paras, S.V., 2012. Experimental investigation of the flow of a blood analogue fluid in a replica of a bifurcated small artery. Med. Eng. Phys. 34, 211–218. https://doi.org/10.1016/j.medengphy.2011.07.012

Anna, S.L., 2016. Droplets and Bubbles in Microfluidic Devices. Annu. Rev. Fluid Mech. 48, 285–309. https://doi.org/10.1146/annurev-fluid-122414-034425

Anna, S.L., Bontoux, N., Stone, H.A., 2003. Formation of dispersions using "flow focusing" in microchannels. Appl. Phys. Lett. 82, 364–366. https://doi.org/10.1063/1.1537519

Anselmo, A.C., Zhang, M., Kumar, S., Vogus, D.R., Menegatti, S., Helgeson, M.E., Mitragotri, S., 2015. Elasticity of nanoparticles influences their blood circulation, phagocytosis, endocytosis, and targeting. ACS Nano 9, 3169–3177. https://doi.org/10.1021/acsnano.5b00147

Baroud, C.N., Gallaire, F., Dangla, R., 2010. Dynamics of microfluidic droplets. Lab Chip 10, 2032–2045. https://doi.org/10.1039/C001191F

Basaran, O.A., 2002. Small-scale free surface flows with breakup: Drop formation and emerging applications. AIChE J. 48, 1842–1848. https://doi.org/10.1002/aic.690480902

Basaran, O.A., Gao, H., Bhat, P.P., 2013. Nonstandard Inkjets. Annu. Rev. Fluid Mech. 45, 85–113. https://doi.org/10.1146/annurev-fluid-120710-101148

Bateni, A., Susnar, S.S., Amirfazli, A., Neumann, A.W., 2004. Development of a New Methodology To Study Drop Shape and Surface Tension in Electric Fields. Langmuir 20, 7589–7597. https://doi.org/10.1021/la0494167

Bayram, A., Serhatlioglu, M., Ortac, B., Demic, S., Elbuken, C., Sen, M., Solmaz, M.E., 2018. Integration of glass micropipettes with a 3D printed aligner for microfluidic flow cytometer. Sensors Actuators A Phys. 269, 382–387. https://doi.org/10.1016/j.sna.2017.11.056

Benedusi, M., Aquila, M., Milani, A., Rispoli, G., 2011. A pressure-polishing set-up to fabricate patch pipettes that seal on virtually any membrane, yielding low access resistance and efficient intracellular perfusion. Eur. Biophys. J. 40, 1215–1223. https://doi.org/10.1007/s00249-011-0727-y

Bennett, W.D., Brown, J.S., Zeman, K.L., Hu, S.-C., Scheuch, G., Sommerer, K., 2002. Targeting Delivery of Aerosols to Different Lung Regions. J. Aerosol Med. 15, 179–188. https://doi.org/10.1089/089426802320282301

Bento, D., Pereira, A.I., Lima, J., Miranda, J.M., Lima, R., 2018a. Cell-free layer measurements of in vitro blood flow in a microfluidic network: an automatic and manual approach. Comput. Methods Biomech. Biomed. Eng. Imaging Vis. 6, 629–637. https://doi.org/10.1080/21681163.2017.1329029

Bento, D., Rodrigues, R., Faustino, V., Pinho, D., Fernandes, C., Pereira, A., Garcia, V., Miranda, J., Lima, R., 2018b. Deformation of Red Blood Cells, Air Bubbles, and Droplets in Microfluidic Devices: Flow Visualizations and Measurements. Micromachines 9, 151. https://doi.org/10.3390/mi9040151

Berkland, C., Pollauf, E., Pack, D.W., Kim, K. (Kevin), 2004. Uniform double-walled polymer microspheres of controllable shell thickness. J. Control. Release 96, 101–111. https://doi.org/10.1016/J.JCONREL.2004.01.018

Beyerlein, K.R., Adriano, L., Heymann, M., Kirian, R., Knoška, J., Wilde, F., Chapman, H.N., Bajt, S., 2015. Ceramic micro-injection molded nozzles for serial femtosecond crystallography sample delivery. Rev. Sci. Instrum. 86, 125104. https://doi.org/10.1063/1.4936843

Binder, K.W., Allen, A.J., Yoo, J.J., Atala, A., 2011. Drop-on-demand inkjet bioprinting: a primer. Gene Ther. Regul. 06, 33–49. https://doi.org/10.1142/S1568558611000258

Bird, J.C., Dhiman, R., Kwon, H.-M., Varanasi, K.K., 2013. Reducing the contact time of a bouncing drop. Nature 503, 385–388. https://doi.org/10.1038/nature12740

Bird, J.C., Tsai, S.S.H., Stone, H.A., 2009. Inclined to splash: triggering and inhibiting a splash with tangential velocity. New J. Phys. 11, 063017. https://doi.org/10.1088/1367-2630/11/6/063017

Boutet, S., Lomb, L., Williams, G.J., Barends, T.R.M., Aquila, A., Doak, R.B., Weierstall, U., DePonte, D.P., Steinbrener, J., Shoeman, R.L., Messerschmidt, M., Barty, A., White, T.A., Kassemeyer, S., Kirian, R.A., Seibert, M.M., Montanez, P.A., Kenney, C., Herbst, R., Hart, P., Pines, J., Haller, G., Gruner, S.M., Philipp, H.T., Tate, M.W., Hromalik, M., Koerner, L.J., van Bakel, N., Morse, J., Ghonsalves, W., Arnlund, D., Bogan, M.J., Caleman, C., Fromme, R., Hampton, C.Y., Hunter, M.S., Johansson, L.C., Katona, G., Kupitz, C., Liang, M., Martin, A. V, Nass, K., Redecke, L., Stellato, F., Timneanu, N., Wang, D., Zatsepin, N.A., Schafer, D., Defever, J., Neutze, R., Fromme, P., Spence, J.C.H., Chapman, H.N., Schlichting, I., 2012. High-Resolution Protein Structure Determination by Serial Femtosecond Crystallography. Science (80-.). 337, 362–364. https://doi.org/10.1126/science.1217737

Braun, J., Day, P.K., Toennies, J.P., Witte, G., Neher, E., 1997. Micrometer-sized nozzles and skimmers for the production of supersonic He atom beams. Rev. Sci. Instrum. 68, 3001–3009. https://doi.org/10.1063/1.1148233

Cabezas, M.G., Bateni, A., Montanero, J.M., Neumann, A.W., 2006. Determination of Surface Tension and Contact Angle from the Shapes of Axisymmetric Fluid Interfaces without Use of Apex Coordinates. Langmuir 22, 10053–10060. https://doi.org/10.1021/la061928t

Calejo, J., Pinho, D., Galindo-Rosales, F., Lima, R., Campo-Deaño, L., 2016. Particulate Blood Analogues Reproducing the Erythrocytes Cell-Free Layer in a Microfluidic Device Containing a Hyperbolic Contraction. Micromachines 7, 4. https://doi.org/10.3390/mi7010004

Campo-Deaño, L., Dullens, R.P.A., Aarts, D.G.A.L., Pinho, F.T., Oliveira, M.S.N., 2013. Viscoelasticity of blood and viscoelastic blood analogues for use in polydymethylsiloxane in vitro models of the circulatory system. Biomicrofluidics 7, 034102. https://doi.org/10.1063/1.4804649

Cao, W., Miyamoto, Y., 2006. Freeform fabrication of aluminum parts by direct deposition of molten aluminum. J. Mater. Process. Technol. 173, 209–212. https://doi.org/10.1016/j.jmatprotec.2005.11.028

Cardoso, C., Fernandes, C.S., Lima, R., Ribeiro, J., 2018. Biomechanical analysis of PDMS channels using different hyperelastic numerical constitutive models. Mech. Res. Commun. 90, 26–33. https://doi.org/10.1016/j.mechrescom.2018.04.007

Carneiro, J., Doutel, E., Campos, J.B.L.M., Miranda, J.M., 2016. PDMS droplet formation and characterization by hydrodynamic flow focusing technique in a PDMS square microchannel. J. Micromechanics Microengineering 26, 105013. https://doi.org/10.1088/0960-1317/26/10/105013

Carrier, O., Dervin, E., Funfschilling, D., Li, H.-Z., 2015. Formation of satellite droplets in flow-focusing junctions: volume and neck rupture. Microsyst. Technol. 21, 499–507. https://doi.org/10.1007/s00542-013-1905-x

Castrejón-Pita, A.A., Castrejón-Pita, J.R., Hutchings, I.M., 2012. Experimental observation of von Kármán vortices during drop impact. Phys. Rev. E 86, 045301. https://doi.org/10.1103/PhysRevE.86.045301

Castrejón-Pita, J.R., Morrison, N.F., Harlen, O.G., Martin, G.D., Hutchings, I.M., 2011. Experiments and Lagrangian simulations on the formation of droplets in continuous mode. Phys. Rev. E 83, 016301. https://doi.org/10.1103/PhysRevE.83.016301

Chao, Y.-P., Qi, L.-H., Xiao, Y., Luo, J., Zhou, J.-M., 2012. Manufacturing of micro thin-walled metal parts by micro-droplet deposition. J. Mater. Process. Technol. 212, 484–491. https://doi.org/10.1016/j.jmatprotec.2011.10.015

Chen, K., Merkel, T.J., Pandya, A., Napier, M.E., Luft, J.C., Daniel, W., Sheiko, S., DeSimone, J.M., 2012. Low modulus biomimetic microgel particles with high loading of hemoglobin. Biomacromolecules 13, 2748–2759. https://doi.org/10.1021/bm3007242

Cheng, S.X., Li, T., Chandra, S., 2005. Producing molten metal droplets with a pneumatic droplet-on-demand generator. J. Mater. Process. Technol. 159, 295–302. https://doi.org/10.1016/j.jmatprotec.2004.05.016

Choi, J., Chang, Y., 2005. Characteristics of laser aided direct metal/material deposition process for tool steel. Int. J. Mach. Tools Manuf. 45, 597–607. https://doi.org/10.1016/j.ijmachtools.2004.08.014

Christopher, G.F., Anna, S.L., 2007. Microfluidic methods for generating continuous droplet streams. J. Phys. D. Appl. Phys. 40, R319–R336. https://doi.org/10.1088/0022-3727/40/19/R01

Chua, C.K., Chou, S.M., Wong, T.S., 1998. A study of the state-of-the-art rapid prototyping technologies. Int. J. Adv. Manuf. Technol. 14, 146–152. https://doi.org/10.1007/BF01322222

Cossali, G.E., Coghe, A., Marengo, M., 1997. The impact of a single drop on a wetted solid surface. Exp. Fluids 22, 463–472. https://doi.org/10.1007/s003480050073

Cui, J., Björnmalm, M., Liang, K., Xu, C., Best, J.P., Zhang, X., Caruso, F., 2014. Super-Soft Hydrogel Particles with Tunable Elasticity in a Microfluidic Blood Capillary Model. Adv. Mater. 26, 7295–7299. https://doi.org/10.1002/adma.201402753

Deegan, R.D., Brunet, P., Eggers, J., 2008. Complexities of splashing. Nonlinearity 21, C1–C11. https://doi.org/10.1088/0951-7715/21/1/C01

DePonte, D.P., Weierstall, U., Schmidt, K., Warner, J., Starodub, D., Spence, J.C.H., Doak, R.B., 2008. Gas dynamic virtual nozzle for generation of microscopic droplet streams. J. Phys. D. Appl. Phys. 41, 195505. https://doi.org/10.1088/0022-3727/41/19/195505

Derby, B., 2010. Inkjet Printing of Functional and Structural Materials: Fluid Property Requirements, Feature Stability, and Resolution. Annu. Rev. Mater. Res. 40, 395–414. https://doi.org/10.1146/annurev-matsci-070909-104502

Derby, B., 2008. Bioprinting: inkjet printing proteins and hybrid cell-containing materials and structures. J. Mater. Chem. 18, 5717. https://doi.org/10.1039/b807560c

Djuric, Z., Grant, P., 2001. Two-dimensional simulation of liquid metal spray deposition onto a complex surface: II. Splashing and redeposition. Model. Simul. Mater. Sci. Eng. 9, 111–127. https://doi.org/10.1088/0965-0393/9/2/305

do Nascimento, D.F., Avendaño, J.A., Mehl, A., Moura, M.J.B., Carvalho, M.S., Duncanson, W.J., 2017. Flow of Tunable Elastic Microcapsules through Constrictions. Sci. Rep. 7, 11898. https://doi.org/10.1038/s41598-017-11950-2

Doshi, N., Zahr, A.S., Bhaskar, S., Lahann, J., Mitragotri, S., 2009. Red blood cell-mimicking synthetic biomaterial particles. Proc. Natl. Acad. Sci. U. S. A. 106, 21495–21499. https://doi.org/10.1073/pnas.0907127106

Eggers, J., Villermaux, E., 2008. Physics of liquid jets. Reports Prog. Phys. 71, 036601. https://doi.org/10.1088/0034-4885/71/3/036601

Erkal, A., D'Ayala, D., Sequeira, L., 2012. Assessment of wind-driven rain impact, related surface erosion and surface strength reduction of historic building materials. Build. Environ. 57, 336–348. https://doi.org/10.1016/j.buildenv.2012.05.004

Fang, M., Chandra, S., Park, C.B., 2008. Building three-dimensional objects by deposition of molten metal droplets. Rapid Prototyp. J. 14, 44–52. https://doi.org/10.1108/13552540810841553

Faustino, V., Pinho, D., Yaginuma, T., Calhelha, R.C., Ferreira, I.C.F.R., Lima, R., 2014. Extensional flow-based microfluidic device: deformability assessment of red blood cells in contact with tumor cells. BioChip J. 8, 42–47. https://doi.org/10.1007/s13206-014-8107-1

Feng, Z.C., 1997. Transition to Traveling Waves from Standing Waves in a Rectangular Container Subjected to Horizontal Excitations. Phys. Rev. Lett. 79, 415–418. https://doi.org/10.1103/PhysRevLett.79.415

Ferrera, C., Herrada, M.A., Montanero, J.M., 2016. Analysis of a resonance liquid bridge oscillation on board of the International Space Station. Eur. J. Mech. - B/Fluids 57, 15–21. https://doi.org/10.1016/j.euromechflu.2016.02.003

Field, J.E., Camus, J.-J., Tinguely, M., Obreschkow, D., Farhat, M., 2012. Cavitation in impacted drops and jets and the effect on erosion damage thresholds. Wear 290–291, 154–160. https://doi.org/10.1016/j.wear.2012.03.006

Fujiwara, T., Johnston, I.D., Tracey, M.C., Tan, C.K.L., 2010. Increasing pumping efficiency in a micro throttle pump by enhancing displacement amplification in an elastomeric substrate. J. Micromechanics Microengineering 20, 065018. https://doi.org/10.1088/0960-1317/20/6/065018

Gañán-Calvo, A.M., 1998. Generation of Steady Liquid Microthreads and Micron-Sized Monodisperse Sprays in Gas Streams. Phys. Rev. Lett. 80, 285–288. https://doi.org/10.1103/PhysRevLett.80.285

Gañán-Calvo, A.M., Montanero, J.M., Martín-Banderas, L., Flores-Mosquera, M., 2013. Building functional materials for health care and pharmacy from microfluidic principles and Flow Focusing. Adv. Drug Deliv. Rev. 65, 1447–1469. https://doi.org/10.1016/j.addr.2013.08.003

Ghanbari, A., Nock, V., Johari, S., Blaikie, R., Chen, X., Wang, W., 2012. A micropillar-based on-chip system for continuous force measurement of C. elegans. J. Micromechanics Microengineering 22, 095009. https://doi.org/10.1088/0960-1317/22/9/095009

Gibson, I., Rosen, D.W., Stucker, B., 2010. Additive manufacturing technologies: Rapid prototyping to direct digital manufacturing, Additive Manufacturing Technologies: Rapid Prototyping to Direct Digital Manufacturing. Springer US. https://doi.org/10.1007/978-1-4419-1120-9

Goodman, M.B., Lockery, S.R., 2000. Pressure polishing: a method for re-shaping patch pipettes during fire polishing. J. Neurosci. Methods 100, 13–15. https://doi.org/10.1016/S0165-0270(00)00224-7

Grams, M.P., Cook, A.M., Turner, J.H., Doak, R.B., 2006. Microscopic fused silica capillary nozzles as supersonic molecular beam sources. J. Phys. D. Appl. Phys. 39, 930–936. https://doi.org/10.1088/0022-3727/39/5/006

Gu, D.D., Meiners, W., Wissenbach, K., Poprawe, R., 2012. Laser additive manufacturing of metallic components: Materials, processes and mechanisms. Int. Mater. Rev. 57, 133–164. https://doi.org/10.1179/1743280411Y.0000000014

Gu, Y., Kojima, H., Miki, N., 2011. Theoretical analysis of 3D emulsion droplet generation by a device using coaxial glass tubes. Sensors Actuators A Phys. 169, 326–332. https://doi.org/10.1016/j.sna.2011.02.043

Higuera, M., Nicolás, J.A., 1997. Linear nonaxisymmetric oscillations of nearly inviscid liquid bridges. Phys. Fluids 9, 276–285. https://doi.org/10.1063/1.869148

Hoorfar, M., W. Neumann, A., 2006. Recent progress in Axisymmetric Drop Shape Analysis (ADSA). Adv. Colloid Interface Sci. 121, 25–49. https://doi.org/10.1016/j.cis.2006.06.001

Hou, H.W., Bhagat, A.A.S., Lin Chong, A.G., Mao, P., Wei Tan, K.S., Han, J., Lim, C.T., 2010. Deformability based cell margination—A simple microfluidic design for malaria-infected erythrocyte separation. Lab Chip 10, 2605. https://doi.org/10.1039/c003873c

Howison, S.D., Ockendon, J.R., Oliver, J.M., 2004. Oblique slamming, planing and skimming. J. Eng. Math. 48, 321–337. https://doi.org/10.1023/B:engi.0000018156.40420.50

Huh, D., Torisawa, Y., Hamilton, G.A., Kim, H.J., Ingber, D.E., 2012. Microengineered physiological biomimicry: Organs-on-Chips. Lab Chip 12, 2156. https://doi.org/10.1039/c2lc40089h

Jaensson, N., Vermant, J., 2018. Tensiometry and rheology of complex interfaces. Curr. Opin. Colloid Interface Sci. 37, 136–150. https://doi.org/10.1016/j.cocis.2018.09.005

Jeong, O.C., Konishi, S., 2011. Controlling the size of replicable polydimethylsiloxane (PDMS) molds/stamps using a stepwise thermal shrinkage process. Microelectron. Eng. 88, 2286–2289. https://doi.org/10.1016/j.mee.2010.12.005

Jiang, K., Thomas, P.C., Forry, S.P., DeVoe, D.L., Raghavan, S.R., 2012. Microfluidic synthesis of monodisperse PDMS microbeads as discrete oxygen sensors. Soft Matter 8, 923–926. https://doi.org/10.1039/C2SM06685H

Jiang, X.-S., Qi, L.-H., Luo, J., Huang, H., Zhou, J.-M., 2010. Research on accurate droplet generation for micro-droplet deposition manufacture. Int. J. Adv. Manuf. Technol. 49, 535–541. https://doi.org/10.1007/s00170-009-2403-2

Johnston, I.D., McCluskey, D.K., Tan, C.K.L., Tracey, M.C., 2014. Mechanical characterization of bulk Sylgard 184 for microfluidics and microengineering. J. Micromechanics Microengineering 24, 35017. https://doi.org/10.1088/0960-1317/24/3/035017

Josserand, C., Thoroddsen, S.T., 2016. Drop Impact on a Solid Surface. Annu. Rev. Fluid Mech. 48, 365–391. https://doi.org/10.1146/annurev-fluid-122414-034401

Josserand, C., Zaleski, S., 2003. Droplet splashing on a thin liquid film. Phys. Fluids 15, 1650. https://doi.org/10.1063/1.1572815

Ju, X., Wang, X., Liu, Z., Xie, R., Wang, W., Chu, L., 2017. Red-blood-cell-shaped chitosan microparticles prepared by electrospraying. Particuology 30, 151–157. https://doi.org/10.1016/j.partic.2016.05.011

Kalambur, V.S., Han, B., Hammer, B.E., Shield, T.W., Bischof, J.C., 2005. In vitro characterization of movement, heating and visualization of magnetic nanoparticles for biomedical applications. Nanotechnology 16, 1221–1233. https://doi.org/10.1088/0957-4484/16/8/041

Khan, A., Rahman, K., Kim, D.S., Choi, K.H., 2012. Direct printing of copper conductive micro-tracks by multi-nozzle electrohydrodynamic inkjet printing process. J. Mater. Process. Technol. 212, 700–706. https://doi.org/10.1016/j.jmatprotec.2011.10.024

Khare, S.M., Awasthi, A., Venkataraman, V., Koushika, S.P., 2015. Colored polydimethylsiloxane micropillar arrays for high throughput measurements of forces applied by genetic model organisms. Biomicrofluidics 9, 014111. https://doi.org/10.1063/1.4906905

Khullar, V., Tyagi, H., Hordy, N., Otanicar, T.P., Hewakuruppu, Y., Modi, P., Taylor, R.A., 2014. Harvesting solar thermal energy through nanofluid-based volumetric absorption systems. Int. J. Heat Mass Transf. 77, 377–384. https://doi.org/10.1016/j.ijheatmasstransfer.2014.05.023

Korobkin, A.A., 1988. Inclined entry of a blunt profile into an ideal fluid. Fluid Dyn. 23, 443–447. https://doi.org/10.1007/BF01054755

Kupitz, C., Basu, S., Grotjohann, I., Fromme, R., Zatsepin, N.A., Rendek, K.N., Hunter, M.S., Shoeman, R.L., White, T.A., Wang, D., James, D., Yang, J.H., Cobb, D.E., Reeder, B., Sierra, R.G., Liu, H., Barty, A., Aquila, A.L., Deponte, D., Kirian, R.A., Bari, S., Bergkamp, J.J., Beyerlein, K.R., Bogan, M.J., Caleman, C., Chao, T.C., Conrad, C.E., Davis, K.M., Fleckenstein, H., Galli, L., Hau-Riege, S.P., Kassemeyer, S., Laksmono, H., Liang, M., Lomb, L., Marchesini, S., Martin, A. V., Messerschmidt, M., Milathianaki, D., Nass, K., Ros, A., Roy-Chowdhury, S., Schmidt, K., Seibert, M., Steinbrener, J., Stellato, F., Yan, L., Yoon, C., Moore, T.A., Moore, A.L., Pushkar, Y., Williams, G.J., Boutet, S., Doak, R.B., Weierstall, U., Frank, M., Chapman, H.N., Spence, J.C.H., Fromme, P., 2014. Serial time-resolved crystallography of photosystem II using a femtosecond X-ray laser. Nature 513, 261–265. https://doi.org/10.1038/nature13453

Leble, V., Lima, R., Dias, R., Fernandes, C., Ishikawa, T., Imai, Y., Yamaguchi, T., 2011. Asymmetry of red blood cell motions in a microchannel with a diverging and converging bifurcation. Biomicrofluidics 5, 044120. https://doi.org/10.1063/1.3672689

Lee, J.N., Park, C., Whitesides, G.M., 2003. Solvent Compatibility of Poly(dimethylsiloxane)-Based Microfluidic Devices. Anal. Chem. 75, 6544–6554. https://doi.org/10.1021/ac0346712

Lee, S.W., Lee, S.S., 2008. Shrinkage ratio of PDMS and its alignment method for the wafer level process. Microsyst. Technol. 14, 205–208. https://doi.org/10.1007/s00542-007-0417-y

Lee, T.-K., Kang, T.G., Yang, J.-S., Jo, J., Kim, K.-Y., Choi, B.-O., Kim, D.-S., 2008. Drop-on-demand solder droplet jetting system for fabricating microstructure. IEEE Trans. Electron. Packag. Manuf. 31, 202–210. https://doi.org/10.1109/TEPM.2008.926285

Levenstein, M.A., Bawazer, L.A., Mc Nally, C.S., Marchant, W.J., Gong, X., Meldrum, F.C., Kapur, N., 2016. A reproducible approach to the assembly of microcapillaries for double emulsion production. Microfluid. Nanofluidics 20, 143. https://doi.org/10.1007/s10404-016-1806-2

Lhuissier, H., Tagawa, Y., Tran, T., Sun, C., 2013. Levitation of a drop over a moving surface. J. Fluid Mech. 733, R4. https://doi.org/10.1017/jfm.2013.470

Li, L., Saedan, M., Feng, W., Fuh, J.Y.H., Wong, Y.S., Loh, H.T., Thian, S.C.H., Thoroddsen, S.T., Lu, L., 2009. Development of a multi-nozzle drop-on-demand system for multi-material dispensing. J. Mater. Process. Technol. 209, 4444–4448. https://doi.org/10.1016/j.jmatprotec.2008.10.040

Lima, R., Ishikawa, T., Imai, Y., Yamaguchi, T., 2012. Blood Flow Behavior in Microchannels: Past, Current and Future Trends, in: Lima, R., Ishikawa, T., Imai, Y., Yamaguchi, T. (Eds.), Single and Two-Phase Flows on Chemical and Biomedical Engineering. Bentham Science Publishers, pp. 513–547. https://doi.org/10.2174/978160805295011201010513

Lima, R., Wada, S., Tanaka, S., Takeda, M., Ishikawa, T., Tsubota, K., Imai, Y., Yamaguchi, T., 2008. In vitro blood flow in a rectangular PDMS microchannel: experimental observations using a confocal micro-PIV system. Biomed. Microdevices 10, 153–167. https://doi.org/10.1007/s10544-007-9121-z

Liu, Y., Tan, P., Xu, L., 2015. Kelvin–Helmholtz instability in an ultrathin air film causes drop splashing on smooth surfaces. Proc. Natl. Acad. Sci. 112, 3280–3284. https://doi.org/10.1073/pnas.1417718112

Luo, J., Qi, L.-H., Jiang, X. -s., Zhou, J. -m., Huang, H., 2008. Research on lateral instability of the uniform-charged droplet stream during droplet-based freeform fabrication. Int. J. Mach. Tools Manuf. 48, 289–294. https://doi.org/10.1016/j.ijmachtools.2007.10.012

Maeda, N., 1996. Erythrocyte Rheology in Microcirculation. Jpn. J. Physiol. 46, 1–14. https://doi.org/10.2170/jjphysiol.46.1

Malboubi, M., Gu, Y., Jiang, K., 2011. Surface properties of glass micropipettes and their effect on biological studies. Nanoscale Res. Lett. 6, 401. https://doi.org/10.1186/1556-276X-6-401

Mata, A., Fleischman, A.J., Roy, S., 2005. Characterization of Polydimethylsiloxane (PDMS) Properties for Biomedical Micro/Nanosystems. Biomed. Microdevices 7, 281–293. https://doi.org/10.1007/s10544-005-6070-2

McDonald, A., Lamontagne, M., Moreau, C., Chandra, S., 2006. Impact of plasma-sprayed metal particles on hot and cold glass surfaces. Thin Solid Films 514, 212–222. https://doi.org/10.1016/j.tsf.2006.03.010

Merkel, T.J., Jones, S.W., Herlihy, K.P., Kersey, F.R., Shields, A.R., Napier, M.E., Luft, J.C., Wu, H., Zamboni, W.C., Wang, A.Z., Bear, J.E., DeSimone, J.M., 2011. Using mechanobiological mimicry of red blood cells to extend circulation times of hydrogel microparticles. Proc. Natl. Acad. Sci. U. S. A. 108, 586–591. https://doi.org/10.1073/pnas.1010013108

Montanero, J.M., Gañán-Calvo, A.M., Acero, A.J., Vega, E.J., 2010. Micrometer glass nozzles for flow focusing. J. Micromechanics Microengineering 20, 075035. https://doi.org/10.1088/0960-1317/20/7/075035

Moore, M.R., Howison, S.D., Ockendon, J.R., Oliver, J.M., 2012. Three-dimensional oblique water-entry problems at small deadrise angles. J. Fluid Mech. 711, 259–280. https://doi.org/10.1017/jfm.2012.391

Moore, M.R., Ockendon, H., Ockendon, J.R., Oliver, J.M., 2014. Capillary and viscous perturbations to Helmholtz flows. J. Fluid Mech. 742, R1. https://doi.org/10.1017/jfm.2014.39

Moraes, C., Sun, Y., Simmons, C. a, 2009. Solving the shrinkage-induced PDMS alignment registration issue in multilayer soft lithography. J. Micromechanics Microengineering 19, 065015. https://doi.org/10.1088/0960-1317/19/6/065015

Moreira, A.L.N., Moita, A.S., Panão, M.R., 2010. Advances and challenges in explaining fuel spray impingement: How much of single droplet impact research is useful? Prog. Energy Combust. Sci. 36, 554–580. https://doi.org/10.1016/j.pecs.2010.01.002

Morimoto, Y., Tan, W.-H., Takeuchi, S., 2009. Three-dimensional axisymmetric flow-focusing device using stereolithography. Biomed. Microdevices 11, 369–377. https://doi.org/10.1007/s10544-008-9243-y

Muñoz-Sánchez, B.N., Cabezas, M.G., 2018. Borosilicate nozzles manufactured by reproducible fire shaping. J. Mater. Process. Technol. 261, 173–183. https://doi.org/10.1016/j.jmatprotec.2018.06.011

Murr, L.E., Gaytan, S.M., Medina, F., Martinez, E., Martinez, J.L., Hernandez, D.H., Machado, B.I., Ramirez, D.A., Wicker, R.B., 2010. Characterization of Ti-6Al-4V open cellular foams fabricated by additive manufacturing using electron beam melting. Mater. Sci. Eng. A 527, 1861–1868. https://doi.org/10.1016/j.msea.2009.11.015

Neeson, M.J., Chan, D.Y.C., Tabor, R.F., 2014. Compound Pendant Drop Tensiometry for Interfacial Tension Measurement at Zero Bond Number. Langmuir 30, 15388–15391. https://doi.org/10.1021/la504406m

Nelson, G., Kirian, R.A., Weierstall, U., Zatsepin, N.A., Faragó, T., Baumbach, T., Wilde, F., Niesler, F.B.P., Zimmer, B., Ishigami, I., Hikita, M., Bajt, S., Yeh, S.-R., Rousseau, D.L., Chapman, H.N., Spence, J.C.H., Heymann, M., 2016. Three-dimensional-printed gas dynamic virtual nozzles for x-ray laser sample delivery. Opt. Express 24, 11515–11530. https://doi.org/10.1364/OE.24.011515

Nisisako, T., Torii, T., Higuchi, T., 2002. Droplet formation in a microchannel network. Lab Chip 2, 24–26. https://doi.org/10.1039/B108740C

Ohashi, T., Sato, M., 2012. Single and Two-Phase Flows on Chemical and Biomedical Engineering, Single and Two-phase Flows on Chemical and Biomedical Engineering. BENTHAM SCIENCE PUBLISHERS. https://doi.org/10.2174/97816080529501120101

Okorn-Schmidt, H.F., Holsteyns, F., Lippert, A., Mui, D., Kawaguchi, M., Lechner, C., Frommhold, P.E., Nowak, T., Reuter, F., Piqué, M.B., Cairós, C., Mettin, R., 2014. Particle Cleaning Technologies to Meet Advanced Semiconductor Device Process Requirements. ECS J. Solid State Sci. Technol. 3, N3069–N3080. https://doi.org/10.1149/2.011401jss

Orme, M., Smith, R.F., 2000. Enhanced aluminum properties by means of precise droplet deposition. J. Manuf. Sci. Eng. Trans. ASME 122, 484–493. https://doi.org/10.1115/1.1285914

Pak, N., Dergance, M.J., Emerick, M.T., Gagnon, E.B., Forest, C.R., 2011. An Instrument for Controlled, Automated Production of Micrometer Scale Fused Silica Pipettes. J. Mech. Des. 133, 061006. https://doi.org/10.1115/1.4004194

Park, H., Seo, K., Crozier, K.B., 2012. Adding colors to polydimethylsiloxane by embedding vertical silicon nanowires. Appl. Phys. Lett. 101, 193107. https://doi.org/10.1063/1.4766944

Partola, K.R., Andemariam, B., Lykotrafitis, G., 2017. Microfluidic experimental setup for adhesion and recovery measurements of red blood cells in sickle cell disease. J. Mech. Behav. Biomed. Mater. 71, 80–84. https://doi.org/10.1016/j.jmbbm.2017.02.031

Perales, J.M., Meseguer, J., 1992. Theoretical and experimental study of the vibration of axisymmetric viscous liquid bridges. Phys. Fluids A Fluid Dyn. 4, 1110–1130. https://doi.org/10.1063/1.858230

Peters, F., Arabali, D., 2013. Interfacial tension between oil and water measured with a modified contour method. Colloids Surfaces A Physicochem. Eng. Asp. 426, 1–5. https://doi.org/10.1016/j.colsurfa.2013.03.010

Pinho, D., Campo-Deaño, L., Lima, R., Pinho, F.T., 2017. In vitro particulate analogue fluids for experimental studies of rheological and hemorheological behavior of glucose-rich RBC suspensions. Biomicrofluidics 11, 54105. https://doi.org/10.1063/1.4998190

Pinho, D., Rodrigues, R.O., Faustino, V., Yaginuma, T., Exposto, J., Lima, R., 2016. Red blood cells radial dispersion in blood flowing through microchannels: The role of temperature. J. Biomech. 49, 2293–2298. https://doi.org/10.1016/j.jbiomech.2015.11.037

Pinho, D., Yaginuma, T., Lima, R., 2013. A microfluidic device for partial cell separation and deformability assessment. BioChip J. 7, 367–374. https://doi.org/10.1007/s13206-013-7408-0

Pinto, E., Faustino, V., Rodrigues, R., Pinho, D., Garcia, V., Miranda, J., Lima, R., 2015. A Rapid and Low-Cost Nonlithographic Method to Fabricate Biomedical Microdevices for Blood Flow Analysis. Micromachines 6, 121–135. https://doi.org/10.3390/mi6010121

Piotter, V., Klein, A., Plewa, K., Beyerlein, K.R., Chapman, H.N., Bajt, S., 2018. Development of a ceramic injection molding process for liquid jet nozzles to be applied for X-ray free-electron lasers. Microsyst. Technol. 24, 1247–1252. https://doi.org/10.1007/s00542-017-3493-7

Rayleigh, Lord, 1878. On The Instability Of Jets. Proc. London Math. Soc. s1-10, 4–13. https://doi.org/10.1112/plms/s1-10.1.4

Riboux, G., Gordillo, J.M., 2014. Experiments of Drops Impacting a Smooth Solid Surface: A Model of the Critical Impact Speed for Drop Splashing. Phys. Rev. Lett. 113, 024507. https://doi.org/10.1103/PhysRevLett.113.024507

Rodrigues, R.O., Bañobre-López, M., Gallo, J., Tavares, P.B., Silva, A.M.T., Lima, R., Gomes, H.T., 2016a. Haemocompatibility of iron oxide nanoparticles synthesized for theranostic applications: a high-sensitivity microfluidic tool. J. Nanoparticle Res. 18, 194. https://doi.org/10.1007/s11051-016-3498-7

Rodrigues, R.O., Lopes, R., Pinho, D., Pereira, A.I., Garcia, V., Gassmann, S., Sousa, P.C., Lima, R., 2016b. In vitro blood flow and cell-free layer in hyperbolic microchannels: Visualizations and measurements. BioChip J. 10, 9–15. https://doi.org/10.1007/s13206-016-0102-2

Rodrigues, R.O., Pinho, D., Faustino, V., Lima, R., 2015. A simple microfluidic device for the deformability assessment of blood cells in a continuous flow. Biomed. Microdevices 17, 108. https://doi.org/10.1007/s10544-015-0014-2

Ru, C., Luo, J., Xie, S., Sun, Y., 2014. A review of non-contact micro- and nano-printing technologies. J. Micromechanics Microengineering 24, 053001. https://doi.org/10.1088/0960-1317/24/5/053001

Saad, S.M.I., Neumann, A.W., 2016. Axisymmetric Drop Shape Analysis (ADSA): An Outline. Adv. Colloid Interface Sci. 238, 62–87. https://doi.org/10.1016/j.cis.2016.11.001

Saidur, R., Leong, K.Y., Mohammad, H.A., 2011. A review on applications and challenges of nanofluids. Renew. Sustain. Energy Rev. 15, 1646–1668. https://doi.org/10.1016/j.rser.2010.11.035

Sanz, A., Diez, J.L., 1989. Non-axisymmetric oscillations of liquid bridges. J. Fluid Mech. 205, 503. https://doi.org/10.1017/S0022112089002120

Sattler, R., Wagner, C., Eggers, J., 2008. Blistering Pattern and Formation of Nanofibers in Capillary Thinning of Polymer Solutions. Phys. Rev. Lett. 100, 164502. https://doi.org/10.1103/PhysRevLett.100.164502

Secomb, T.W., Pries, A.R., 2013. Blood viscosity in microvessels: experiment and theory. Comptes Rendus Phys. 14, 470–478. https://doi.org/10.1016/j.crhy.2013.04.002

Seo, J.-H., Sakai, K., Yui, N., 2013. Adsorption state of fibronectin on poly(dimethylsiloxane) surfaces with varied stiffness can dominate adhesion density of fibroblasts. Acta Biomater. 9, 5493–5501. https://doi.org/10.1016/j.actbio.2012.10.015

She, S., Li, Q., Shan, B., Tong, W., Gao, C., 2013. Fabrication of Red-Blood-Cell-Like Polyelectrolyte Microcapsules and Their Deformation and Recovery Behavior Through a Microcapillary. Adv. Mater. 25, 5814–5818. https://doi.org/10.1002/adma.201302875

Shin, M., Matsuda, K., Ishii, O., Terai, H., Kaazempur-Mofrad, M., Borenstein, J., Detmar, M., Vacanti, J.P., 2004. Endothelialized Networks with a Vascular Geometry in Microfabricated Poly(dimethyl siloxane). Biomed. Microdevices 6, 269–278. https://doi.org/10.1023/B:BMMD.0000048559.29932.27

Sousa, P.C., Pinho, F.T., Oliveira, M.S.N., Alves, M.A., 2011. Extensional flow of blood analog solutions in microfluidic devices. Biomicrofluidics 5, 014108. https://doi.org/10.1063/1.3567888

Stockslager, M.A., Capocasale, C.M., Holst, G.L., Simon, M.D., Li, Y., McGruder, D.J., Rousseau, E.B., Stoy, W.A., Sulchek, T., Forest, C.R., 2016. Optical method for automated measurement of glass micropipette tip geometry. Precis. Eng. 46, 88–95. https://doi.org/10.1016/j.precisioneng.2016.04.003

Sun, H., Björnmalm, M., Cui, J., Wong, E.H.H., Dai, Y., Dai, Q., Qiao, G.G., Caruso, F., 2015. Structure Governs the Deformability of Polymer Particles in a Microfluidic Blood Capillary Model. ACS Macro Lett. 4, 1205–1209. https://doi.org/10.1021/acsmacrolett.5b00591

Sun, S.L., Wu, G.X., 2013. Oblique water-entry of non-axisymmetric bodies at varying speed by a fully nonlinear method. Q. J. Mech. Appl. Math. 66, 366–393. https://doi.org/10.1093/qjmam/hbt011

Switzer, G.L., 1991. A versatile system for stable generation of uniform droplets. Rev. Sci. Instrum. 62, 2765–2771. https://doi.org/10.1063/1.1142211

Tamizhanban, R., Sreejith, K.R., Jayanth, G.R., 2014. An automated pipette puller for fabrication of glass micropipettes. Rev. Sci. Instrum. 85, 055105. https://doi.org/10.1063/1.4874316

Tanaka, T., Ishikawa, T., Numayama-Tsuruta, K., Imai, Y., Ueno, H., Matsuki, N., Yamaguchi, T., 2012. Separation of cancer cells from a red blood cell suspension using inertial force. Lab Chip 12, 4336. https://doi.org/10.1039/c2lc40354d

Tasoglu, S., Demirci, U., 2013. Bioprinting for stem cell research. Trends Biotechnol. 31, 10–19. https://doi.org/10.1016/j.tibtech.2012.10.005

Thoraval, M.-J., Takehara, K., Etoh, T.G., Popinet, S., Ray, P., Josserand, C., Zaleski, S., Thoroddsen, S.T., 2012. von Kármán Vortex Street within an Impacting Drop. Phys. Rev. Lett. 108, 264506. https://doi.org/10.1103/PhysRevLett.108.264506

Thoraval, M.-J., Takehara, K., Etoh, T.G., Thoroddsen, S.T., 2013. Drop impact entrapment of bubble rings. J. Fluid Mech. 724, 234–258. https://doi.org/10.1017/jfm.2013.147

Thoroddsen, S.T., 2002. The ejecta sheet generated by the impact of a drop. J. Fluid Mech. 451, 373–381. https://doi.org/10.1017/S0022112001007030

Thoroddsen, S.T., Etoh, T.G., Takehara, K., 2008. High-Speed Imaging of Drops and Bubbles. Annu. Rev. Fluid Mech. 40, 257–285. https://doi.org/10.1146/annurev.fluid.40.111406.102215

Thoroddsen, S.T., Mahadevan, L., 1997. Experimental study of coating flows in a partially-filled horizontally Rotating cylinder. Exp. Fluids 23, 1–13. https://doi.org/10.1007/s003480050080

Tjahjadi, M., Stone, H. a., Ottino, J.M., 1992. Satellite and subsatellite formation in capillary breakup. J. Fluid Mech. 243, 297–317. https://doi.org/10.1017/S0022112092002738

Tognoni, E., Baschieri, P., Ascoli, C., Pellegrini, M., Pellegrino, M., 2016. Characterization of tip size and geometry of the pipettes used in scanning ion conductance microscopy. Micron 83, 11–18. https://doi.org/10.1016/j.micron.2016.01.002

Tomaiuolo, G., 2014. Biomechanical properties of red blood cells in health and disease towards microfluidics. Biomicrofluidics 8, 051501. https://doi.org/10.1063/1.4895755

Tomotika, S., 1936. Breaking up of a Drop of Viscous Liquid Immersed in Another Viscous Fluid Which is Extending at a Uniform Rate. Proc. R. Soc. A Math. Phys. Eng. Sci. 153, 302–318. https://doi.org/10.1098/rspa.1936.0003

Tomotika, S., 1935. On the Instability of a Cylindrical Thread of a Viscous Liquid Surrounded by Another Viscous Fluid. Proc. R. Soc. A Math. Phys. Eng. Sci. 150, 322–337. https://doi.org/10.1098/rspa.1935.0104

Trebbin, M., Krüger, K., DePonte, D., Roth, S. V, Chapman, H.N., Förster, S., 2014. Microfluidic liquid jet system with compatibility for atmospheric and high-vacuum conditions. Lab Chip 14, 1733–1745. https://doi.org/10.1039/C3LC51363G

Tripathi, S., Varun Kumar, Y.V.B., Prabhakar, A., Joshi, S.S., Agrawal, A., 2015. Passive blood plasma separation at the microscale: A review of design principles and microdevices. J. Micromechanics Microengineering 25, 083001. https://doi.org/10.1088/0960-1317/25/8/083001

Tsamopoulos, J., Chen, T.-Y., Borkar, A., 1992. Viscous oscillations of capillary bridges. J. Fluid Mech. 235, 579. https://doi.org/10.1017/S002211209200123X

Utada, A.S., Lorenceau, E., Link, D.R., Kaplan, P.D., Stone, H.A., Weitz, D.A., 2005. Monodisperse Double Emulsions Generated from a Microcapillary Device. Science (80-.). 308, 537–541. https://doi.org/10.1126/science.1109164

Varesano, A., Carletto, R.A., Mazzuchetti, G., 2009. Experimental investigations on the multi-jet electrospinning process. J. Mater. Process. Technol. 209, 5178–5185. https://doi.org/10.1016/j.jmatprotec.2009.03.003

Vaught, J.L., Cloutier, F.L., Donald, D.K., Meyer, J.D., Tacklind, C.A., Taub, H.H., 1984. Thermal ink jet printer. United States Pat. 4490728.

Vega, E.J., Cabezas, M.G., Muñoz-Sánchez, B.N., Montanero, J.M., Gañán-Calvo, A.M., 2014. A novel technique to produce metallic microdrops for additive manufacturing. Int. J. Adv. Manuf. Technol. 70, 1395–1402. https://doi.org/10.1007/s00170-013-5357-3

Vega, E.J., Gañán-Calvo, A.M., Montanero, J.M., Cabezas, M.G., Herrada, M.A., 2013. A novel technique for producing metallic microjets and microdrops. Microfluid. Nanofluidics 14, 101–111. https://doi.org/10.1007/s10404-012-1027-2

Vega, E.J., Montanero, J.M., Ferrera, C., 2011. Exploring the precision of backlight optical imaging in microfluidics close to the diffraction limit. Measurement 44, 1300–1311. https://doi.org/10.1016/j.measurement.2011.03.020

Vehring, R., 2008. Pharmaceutical Particle Engineering via Spray Drying. Pharm. Res. 25, 999–1022. https://doi.org/10.1007/s11095-007-9475-1

Verma, S.K., Tiwari, A.K., 2015. Progress of nanofluid application in solar collectors: A review. Energy Convers. Manag. 100, 324–346. https://doi.org/10.1016/j.enconman.2015.04.071

Vilanova, N., Rodríguez-Abreu, C., Fernández-Nieves, A., Solans, C., 2013. Fabrication of Novel Silicone Capsules with Tunable Mechanical Properties by Microfluidic Techniques. ACS Appl. Mater. Interfaces 5, 5247–5252. https://doi.org/10.1021/am4010896

Vladisavljević, G.T., Kobayashi, I., Nakajima, M., 2012. Production of uniform droplets using membrane, microchannel and microfluidic emulsification devices. Microfluid. Nanofluidics 13, 151–178. https://doi.org/10.1007/s10404-012-0948-0

Wang, J.-T., Wang, J., Han, J.-J., 2011. Fabrication of Advanced Particles and Particle-Based Materials Assisted by Droplet-Based Microfluidics. Small 7, 1728–1754. https://doi.org/10.1002/smll.201001913

Wang, T., Liu, J., Yang, B., Chen, X., Wang, X., Yang, C., 2016. Optimization of micropipette fabrication by laser micromachining for application in an ultrafine atmospheric pressure plasma jet using response surface methodology. J. Micromechanics Microengineering 26, 065001. https://doi.org/10.1088/0960-1317/26/6/065001

Wang, Z., Volinsky, A.A., Gallant, N.D., 2014. Crosslinking effect on polydimethylsiloxane elastic modulus measured by custom-built compression instrument. J. Appl. Polym. Sci. 131, 41050. https://doi.org/10.1002/app.41050

Weierstall, U., James, D., Wang, C., White, T.A., Wang, D., Liu, W., Spence, J.C.H., Bruce Doak, R., Nelson, G., Fromme, P., Fromme, R., Grotjohann, I., Kupitz, C., Zatsepin, N.A., Liu, H., Basu, S., Wacker, D., Won Han, G., Katritch, V., Boutet, S., Messerschmidt, M., Williams, G.J., Koglin, J.E., Marvin Seibert, M., Klinker, M., Gati, C., Shoeman, R.L., Barty, A., Chapman, H.N., Kirian, R.A., Beyerlein, K.R., Stevens, R.C., Li, D., Shah, S.T.A., Howe, N., Caffrey, M., Cherezov, V., 2014. Lipidic cubic phase injector facilitates membrane protein serial femtosecond crystallography. Nat. Commun. 5, 3309. https://doi.org/10.1038/ncomms4309

Weierstall, U., Spence, J.C.H., Doak, R.B., 2012. Injector for scattering measurements on fully solvated biospecies. Rev. Sci. Instrum. 83, 035108. https://doi.org/10.1063/1.3693040

Wiedorn, M.O., Oberthür, D., Bean, R., Schubert, R., Werner, N., Abbey, B., Aepfelbacher, M., Adriano, L., Allahgholi, A., Al-Qudami, N., Andreasson, J., Aplin, S., Awel, S., Ayyer, K., Bajt, S., Barák, I., Bari, S., Bielecki, J., Botha, S., Boukhelef, D., Brehm, W., Brockhauser, S., Cheviakov, I., Coleman, M.A., Cruz-Mazo, F., Danilevski, C., Darmanin, C., Doak, R.B., Domaracky, M., Dörner, K., Du, Y., Fangohr, H., Fleckenstein, H., Frank, M., Fromme, P., Gañán-Calvo, A.M., Gevorkov, Y., Giewekemeyer, K., Ginn, H.M., Graafsma, H., Graceffa, R., Greiffenberg, D., Gumprecht, L., Göttlicher, P., Hajdu, J., Hauf, S., Heymann, M., Holmes, S., Horke, D.A., Hunter, M.S., Imlau, S., Kaukher, A., Kim, Y., Klyuev, A., Knoška, J., Kobe, B., Kuhn, M., Kupitz, C., Küpper, J., Lahey-Rudolph, J.M., Laurus, T., Le Cong, K., Letrun, R., Xavier, P.L., Maia, L., Maia, F.R.N.C., Mariani, V., Messerschmidt, M., Metz, M., Mezza, D., Michelat, T., Mills, G., Monteiro, D.C.F., Morgan, A., Mühlig, K., Munke, A., Münnich, A., Nette, J., Nugent, K.A., Nuguid, T., Orville, A.M., Pandey, S., Pena, G., Villanueva-Perez, P., Poehlsen, J., Previtali, G., Redecke, L., Riekehr, W.M., Rohde, H., Round, A., Safenreiter, T., Sarrou, I., Sato, T., Schmidt, M., Schmitt, B., Schönherr, R., Schulz, J., Sellberg, J.A., Seibert, M.M., Seuring, C., Shelby, M.L., Shoeman, R.L., Sikorski, M., Silenzi, A., Stan, C.A., Shi, X., Stern, S., Sztuk-Dambietz, J., Szuba, J., Tolstikova, A., Trebbin, M., Trunk, U., Vagovic, P., Ve, T., Weinhausen, B., White, T.A., Wrona, K., Xu, C., Yefanov, O., Zatsepin, N., Zhang, J., Perbandt, M., Mancuso, A.P., Betzel, C., Chapman, H., Barty, A., 2018. Megahertz serial crystallography. Nat. Commun. 9, 4025. https://doi.org/10.1038/s41467-018-06156-7

Wijshoff, H., 2010. The dynamics of the piezo inkjet printhead operation. Phys. Rep. 491, 77–177. https://doi.org/10.1016/j.physrep.2010.03.003

Williams, C.B., Cochran, J.K., Rosen, D.W., 2011. Additive manufacturing of metallic cellular materials via three-dimensional printing. Int. J. Adv. Manuf. Technol. 53, 231–239. https://doi.org/10.1007/s00170-010-2812-2

Worthington, A.M., 1908. A Study of Splashes. Longmans, Green & Co.

Xie, D., Chang, X., Shu, X., Xiao, J., Zhang, H., 2015. Fabrication of Microglass Nozzle for Microdroplet Jetting. Adv. Mech. Eng. 7, 590849. https://doi.org/10.1155/2014/590849

Xu, J., Attinger, D., 2008. Drop on demand in a microfluidic chip. J. Micromechanics Microengineering 18, 065020. https://doi.org/10.1088/0960-1317/18/6/065020

Xu, L., Barcos, L., Nagel, S.R., 2007. Splashing of liquids: Interplay of surface roughness with surrounding gas. Phys. Rev. E 76, 066311. https://doi.org/10.1103/PhysRevE.76.066311

Xu, L., Zhang, W.W., Nagel, S.R., 2005. Drop Splashing on a Dry Smooth Surface. Phys. Rev. Lett. 94, 184505. https://doi.org/10.1103/PhysRevLett.94.184505

Yaginuma, T., Oliveira, M.S.N., Lima, R., Ishikawa, T., Yamaguchi, T., 2013. Human red blood cell behavior under homogeneous extensional flow in a hyperbolic-shaped microchannel. Biomicrofluidics 7, 054110. https://doi.org/10.1063/1.4820414

Yarin, A.L., 2006. Drop Impact Dynamics: Splashing, Spreading, Receding, Bouncing…. Annu. Rev. Fluid Mech. 38, 159–192. https://doi.org/10.1146/annurev.fluid.38.050304.092144

Yaul, M., Bhatti, R., Lawrence, S., 2008. Evaluating the process of polishing borosilicate glass capillaries used for fabrication of in-vitro fertilization (iVF) micro-pipettes. Biomed. Microdevices 10, 123–128. https://doi.org/10.1007/s10544-007-9117-8

Yi, P., Khoshmanesh, K., Campbell, J.L., Coughlan, P., Ghorbani, K., Kalantar-zadeh, K., 2014. Investigation of different nanoparticles for magnetophoretically enabled nanofin heat sinks in microfluidics. Lab Chip 14, 1604–1613. https://doi.org/10.1039/C3LC51331A

Zhang, L., Cao, Z., Li, Y., Ella-Menye, J.-R., Bai, T., Jiang, S., 2012. Softer Zwitterionic Nanogels for Longer Circulation and Lower Splenic Accumulation. ACS Nano 6, 6681–6686. https://doi.org/10.1021/nn301159a

Zhang, L. V, Toole, J., Fezzaa, K., Deegan, R.D., 2012. Splashing from drop impact into a deep pool: multiplicity of jets and the failure of conventional scaling. J. Fluid Mech. 703, 402–413. https://doi.org/10.1017/jfm.2012.249

Zhang, X., Basaran, O.A., 1995. An experimental study of dynamics of drop formation. Phys. Fluids 7, 1184–1203. https://doi.org/10.1063/1.868577

Zhao, L.-B., Li, S.-Z., Hu, H., Guo, Z.-X., Guo, F., Zhang, N.-G., Ji, X.-H., Liu, W., Liu, K., Guo, S.-S., Zhao, X.-Z., 2011. A novel method for generation of amphiphilic PDMS particles by selective modification. Microfluid. Nanofluidics 10, 453–458. https://doi.org/10.1007/s10404-010-0673-5

PAPER I:
DROPLET IMPACT ONTO MOVING LIQUIDS

Authors:

J. Rafael Castrejón-Pita, Beatriz N. Muñoz-Sánchez, Ian M. Hutchings, and Alfonso A. Castrejón-Pita

Paper published in:

Journal of Fluid Mechanics, 809 (2016), 716–725

DOI: 10.1017/jfm.2016.672

PAPER II:

A NOVEL TECHNIQUE TO PRODUCE METALLIC MICRODROPS FOR ADDITIVE MANUFACTURING

Authors:

Emilio J. Vega, M. Guadalupe Cabezas, Beatriz N. Muñoz-Sánchez, José M. Montanero, and Alfonso M. Gañán-Calvo

Paper published in:

The International Journal of Advanced Manufacturing Technology, 70 (2014), 1395–1402

DOI: 10.1007/s00170-013-5357-3

PAPER III:

GENERATION OF MICRO-SIZED PDMS PARTICLES BY A FLOW FOCUSING TECHNIQUE FOR BIOMICROFLUIDICS APPLICATIONS

Authors:

Beatriz N. Muñoz-Sánchez, Susana F. Silva, Diana Pinho, Emilio J. Vega, and Rui Lima

Paper published in:

Biomicrofluidics, 10 (2016), 14122

DOI: 10.1063/1.4943007

PAPER IV:
SHRINKAGE AND COLOUR IN THE PRODUCTION OF MICRO-SIZED PDMS PARTICLES FOR MICROFLUIDIC APPLICATIONS

Authors:

Claudia F. Anes, Diana Pinho, Beatriz N. Muñoz-Sánchez, Emilio J. Vega, and Rui Lima

Paper published in:

Journal of Micromechanics and Microengineering, 28 (2018), 075002

DOI: 10.1088/1361-6439/aab7b9

PAPER V:

FLEXIBLE PDMS MICROPARTICLES TO MIMIC RBCS IN BLOOD PARTICULATE ANALOGUE FLUIDS

Authors:

Diana Pinho, Beatriz N. Muñoz-Sánchez, Claudia F. Anes, Emilio J. Vega, and Rui Lima

Paper published in:

Mechanics Research Communications, 100 (2019), 103399

DOI: 10.1016/j.mechrescom.2019.103399

PAPER VI: BOROSILICATE NOZZLES MANUFACTURED BY REPRODUCIBLE FIRE SHAPING

Authors:

Beatriz N. Muñoz-Sánchez and M. Guadalupe Cabezas

Paper published in:

Journal of Materials Processing Technology, 261 (2018), 173–183

DOI: 10.1016/j.jmatprotec.2018.06.011

PAPER VII:
A NEW FIRE SHAPING APPROACH TO PRODUCE HIGHLY AXISYMMETRIC AND REPRODUCIBLE NOZZLES

Authors:
Beatriz N. Muñoz-Sánchez, Alfonso M. Gañán-Calvo, and M. Guadalupe Cabezas

Paper published in:
Journal of Materials Processing Technology, 270 (2019), 241–253
DOI: 10.1016/j.jmatprotec.2019.02.027

PAPER VIII:
A METHOD FOR MEASURING THE INTERFACIAL TENSION FOR DENSITY-MATCHED LIQUIDS

Authors:

Beatriz N. Muñoz-Sánchez, M. Guadalupe Cabezas, Conrado Ferrera, Miguel A. Herrada, and José M. Montanero

Paper published in:

Journal of Colloid and Interface Science, 566 (2020), 90–97

DOI: 10.1016/j.jcis.2020.01.043